Finite Difference Solutions of Quantum Wire and Quantum Dot Sysytems

Dureid El-Moghraby

Submitted in accordance with the requirements

for the degree of Doctor of Philosophy

The University of Leeds

School of Electronic and Electrical Engineering

January 2005

Acknowledgements

In the Name of Allah the Most Beneficent, the Most Merciful

I would like to extend my warmest regards and sincerest gratitude to my supervisors, Paul Harrison and Rob Johnson, without whose guidance and encouragement this thesis would not have been possible. Thank you for your patience.

To Ms Moyra Culbert, I would like to express my most sincere thanks for all her hard work and patience, with my occasionally unreasonable demands.

They say no man is an island and I would have surely have drowned if not for the support and help of my friends and colleagues Naush and Mazin. You have made the seemingly unbearable times, an unforgettable experience. I am deeply grateful for your help in all things non-academic and even some of the academic ones. To all the Holt Park gang, thank you for making this an interesting experience.

My regards also go to Neil Pilgrim, for the countless helpful, stimulating and sometimes overwhelming conversations.

No words can express the depth of gratitude, love and respect I have for my English family, and in particular my Uncle Mike.... Thank you for having faith.

To my uncle Mohamed and aunt Cathy, who are like my parents, without whose help I could never have adjusted to life in England I express my warmest thanks.

To all my colleagues in ISS, thank you for providing a working environment that makes work a joy rather than a chore.

To everyone unmentioned (you know who you are!), you are indeed unforgotten, I owe you all a debt that I cannot repay.

Last but by no means least, my parents, the indomitable Asim El-Moghraby and the incomparable Alawiyya Jamal. Thank you for giving me the confidence, the tools and above all the inspiration to believe that anything is possible.

List of Publications

[1] D. El-Moghraby, R.G. Johnson, and P. Harrison, "Calculating modes of quantum wire and dot systems using a finite differencing technique," *Computer Physics Communications*, vol. 150, no. 3, pp. 235 – 246, 2003.

[2] D. El-Moghraby, R.G. Johnson, and P. Harrison, "The effect of inter-dot separation on the finite difference solution of vertically aligned coupled quantum dots," *Computer Physics Communications*, vol. 155, no. 3, pp. 236 – 243, 2003.

[3] D. El-Moghraby, R.G. Johnson, and P. Harrison, "Calculating modes of quantum wire and dot systems using a finite differencing technique," in *Proceedings of the CMMP 2002- Condensed Matter and Materials Physics* , vol. 26A , pp. 229-229, April 2002, Poster presentation.

Abstract

A new implementation of the finite difference method was developed, and discussed, for solving the time-independent, constant effective mass Schrödinger equation in three dimensions. The motivation behind this approach was to develop a computational technique which is fast to execute and requires a small memory footprint.

To demonstrate its validity, this numerical finite difference method was utilised to calculate the electronic eigenenergies of an infinitely deep quantum wire (QWW), where the results were within 0.25 meV of the analytical values. The method was used to calculate energies of a triangular QWW of finite depth that was found in the literature [62]. The calculated energies showed very good agreement with that of Gangopahdhyay [62], with the difference in eigenenergies ranging between 1 and 10 meV. This difference is likely to arise from the simplified constant effective mass Hamiltonian. The case of a pyramidal quantum dot (QD) was then investigated. It was found that the calculated results were within 2 meV of the values found in the literature [5]. However, the advantages of this method become apparent as it requires a fraction of the memory needed by the eigenvalue method and the computational times also compare favourably.

The effect of the inter-dot separation in a system of vertically aligned pyramidal QDs was then investigated. It was found that when the separation between the QDs was large enough, they behaved as if isolated. As the proximity increased, so did the interaction, which manifests itself as an increase in the peak value of the wave function of the higher energy dot and a reduction in the overall eigenenergies.

The method was extended to incorporate the Poisson equation, and used to calculate the eigenenergies of a QD for a varying number of electrons. As would be expected the eigenenergies of the system rose as more electrons were added to the system. The effect of introducing a varying number of electrons into a system of vertically aligned QDs,

for a number of inter-dot separations, showed that the eigenenergies for a single electron increased as the inter-dot separation was increased. However, for the case of multiple electrons, it was found that the eigenenergies initially decrease and then increase as the inter-dot separation is increased.

List of Principal Abbreviations

AFM	Atomic Force Microscopy
DOS	Density of States
EMA	Effective Mass Approximation
FWHM	Full Width at Half Maximum
LO	Longitudinal Optical Phonon
MBE	Molecular Beam Epitaxy
ML	Monolayer
MOVCVD	Metaloraganic Chemical Vapour Deposition
OPW	Orthogonalized Plane Waves
PL	Photoluminescence
PW	Plane Waves
QD	Quantum Dot
QW	Quantum Wire
QWW	Quantum Well Wire
SH	Semiconductor Heterostructure
STM	Scanning Tunnelling Microscopy
SAQD	Self Assembled Quantum Dot
TEM	Transmission Electron Microscopy
THz	Terahertz

Contents

List of Figures

Chapter 1

Introduction

With the advent of recent advances in epitaxial crystal growth technology, such as molecular-beam epitaxy (MBE) and metalorganic chemical vapour deposition (MOCVD) [1], which have enabled the fabrication of atomically sharp heterojunction interfaces, there has been a growing interest in spatially quantized systems [2]. This interest is largely fuelled by the miniaturisation trend overtaking the microelectronics industry. For instance, as the dimensions of devices become smaller it is becoming apparent that at some scale present device fabrication technology will reach limits at which it will become economically feasible to consider alternative approaches to computing and data storage. Yet the limits set by the physical laws governing present CMOS-based devices may occur at much smaller scales, and as such there is a considerable opportunity for the development of nanoprocessing and nanocharacterization technologies that will enable the present scheme of silicon electronics to reach its ultimate limits. Scanned probe techniques, such as the scanning tunnelling microscope (STM) and the atomic force microscope (AFM), are prime contenders as the silicon nanoprocessing and characterisation tools of the future. Even so, the physical limits of present CMOS based devices, such as tunnelling currents in gate oxides [3] or statistical effects in doping very small structures, will eventually be reached possibly requiring entirely new approaches to computing [4]. One such route is the use of heterojunction devices which operate at the nanoscale level, i.e. operation as quantum

confined devices or quantum tunnelling structures, through structural miniaturisation [4]. One-dimensional confinement is easily achieved through miniaturisation, by forming layered films using MBE. However, unique quantum properties, some based on the behaviour of a single electron, can only be achieved by higher degrees of confinement. Also, optoelectronic devices such as photo-detectors and lasers operating in the far-infrared or terahertz region require quantum structures with very small interlevel spacing, and high emission efficiency which may only be achieved at room temperature with higher dimensional confinement. Arrays of well defined *quantum dots* (QD) structures are particularly valuable in such applications. These structures must be different enough in composition from the surrounding matrix, so that significant band offsets occur, they must be small enough so that the charge carriers are spatially confined and they must be uniform in size so that the energy levels are well defined [5].

1.1 Quantum dots

Quantum dots (QDs) are low-dimensional nanometre sized semiconductor (in some cases metallic) structures that are artificially created for the quantum confinement of only a few electrons. They are called quantum dots, or zero dimensional systems, in reference to their quantum confinement in all three spatial dimensions [6], which is similar to the physical situation in atoms. These dots exhibit typical atomic properties such as discrete energy levels, shell structures and a density of states (DOS) which consists of a series of sharp peaks and, as such, quantum dots are frequently referred to as artificial atoms [5, 7, 8]. However in contrast to natural atoms, the number of electrons in a QD is tunable [7] and their energy levels can be manipulated to tailor the number of confined states and their intersublevel energy spacings [9].

The unique properties of QDs have led to their utilisation in the construction of photomixer devices used for terahertz generation [10], in photoconductive intersubband detectors [11], in lasers [12], and more recently pairs of QDs have been used as "quantum bits"

(qubits) [13, 14] for storing information with the ultimate goal of realising a quantum computer.

1.2 Fabrication techniques

From a chronological point of view, the first techniques to be employed in the realisation of the three dimensional confinement of charge carriers in semiconductor heterostructures were the lithographic patterning and etching of quantum well structures and they still remain the most straightforward way of creating QDs [15]. There are a number of different lithographic techniques such as:

- optical lithography and holography,
- X-ray lithography,
- electron and focused ion beam lithography,
- scanning tunnelling microscopy.

However the fundamental steps involved are basically the same. Namely, to grow a layered structure and impose further structure on it or a three dimensional pattern. Layers are usually patterned in two steps. First the desired area is marked out, by depositing a layer of light-sensitive material or photo-resist, using lithography, and the pattern is then transfered to the semiconductor by either etching, see figure 1.1, or by depositing a layer of a different material, usually metal, on its surface.

As regards the resolution of the these techniques, patterns with line widths larger than 0.5 μm can be obtained using the basic optical lithographic processes by employing light sensitive layers deposited on the material and then exposed to radiation of suitable wavelengths. For line widths smaller than about 0.5 μm, radiation of shorter wavelengths is required and thus an electron beam or X-rays must be used, and these can be focused to a spot of about 10 Å in diameter. For high resolution line widths, below 0.1 μm, a modified version of the scanning electron microscope has been used, which can process

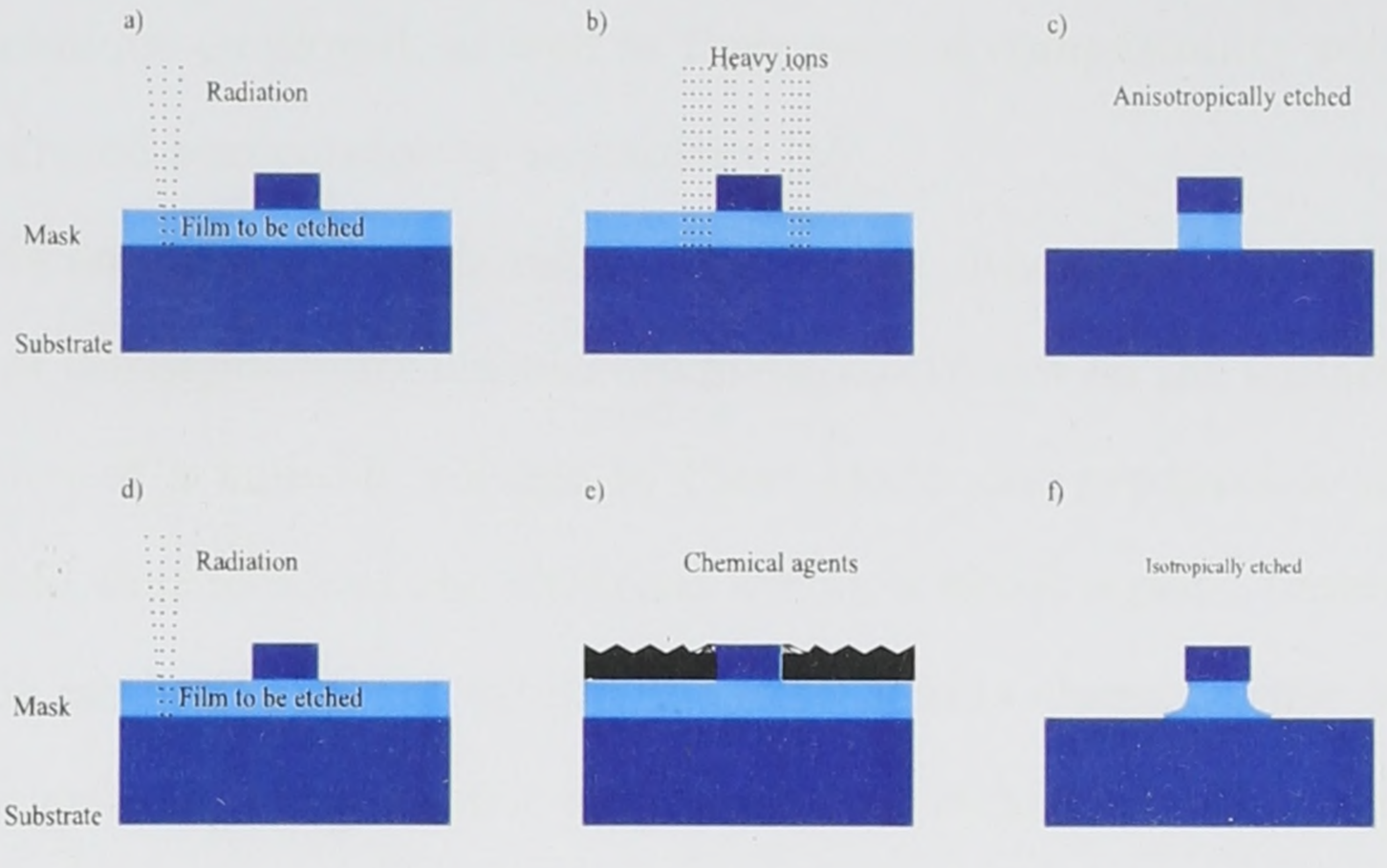

Figure 1.1: Schematic illustration of the basic fabrication principles of three dimensional structure by lithography and the subsequent wet (bottom) or dry (top) etching. (a,d): exposure of the masked resist to radiation; (b): dry etching by heavy ion bombardment; (c): dry etched structure. (e): wet etching by immersion in a solvent; (f): wet etched structure. (Reproduced from reference [5])

wafers of 5 cm in diameter with a maximum spot size of about $2 - 10$ nm [16]. It is worth noting that the advantages of this technique include the fine scale of patterns that can be produced by it and also its versatility. However a severe disadvantage is that it is a serial process and hence very slow. The remaining resist can then be used as a mask to protect the area underneath from the etching . This etching can either be wet, where chemicals in a solution are used, or dry, where ion bombardment is employed. Wet or chemical etching causes little damage to the material, and many selective processes have been developed to etch away the material at a rate dependent on the composition or even the crystallographic orientation of the material. However, structures produced by wet etching are isotropically etched, i.e. no sharp edges, see figure (1.1). In contrast, dry etching produces sharper structures with vertical sidewalls, see figure (1.1), at the cost of damage to the material under the etched surface. Thus, there is great interest in developing fabrication techniques that do not employ lithography or etching. Even so, lithographic techniques have several advantages that still make them appealing, such as the ability to realise dots of almost arbitrary lateral shape, size and arrangement, depending on the resolution of the particular

lithographic technique employed, as well as their general compatibility with modern very large scale integrated semiconductor technology [15].

Another related method worth mentioning is the lithographic patterning of gates, which consists of the deposition of miniature metal electrodes on the surface of a quantum well. Application of a suitable voltage to these electrodes produces a spatially modulated electric field that localises the electrons within a small region. Lateral confinement achieved by this method does not exhibit the edge defects characteristic of etched structures. Thus the creation of an electric gate around an etched dot allows, at least partial, elimination of edge defects and additional squeezing of the electrons [5].

1.2.1 Self-assembled quantum dots (SAQD)

The most recent technique utilised in the creation of quantum dots is the self-organised formation of dots without any artificial patterning. In essence, self-assembly relies on the fact that when semiconductor materials that differ slightly in lattice constants are deposited on each another, the resulting lattice strain can be exploited to obtain three dimensional crystallites or quantum dots.

When a material is grown on a substrate with a different lattice constant, for example InGaAs on GaAs, it can strain to conform to the substrate in the plane of the junction, assuming the substrate is of sufficient thickness so as not to be distorted significantly. This results in the reduction of the lattice constant (for InGaAs on GaAs) in the plane of the junction while being extended in the growth direction due to the elastic response of the material (the opposite occurs for Si on SiGe), see figure (1.2). This distortion in the active layer leads to the build up of elastic energy. This build up continues up to a certain thickness at which the strain is relaxed through the formation of three dimensional islands [17]. It has been proven recently that the three dimensional confinement of charge carriers is attainable within the strained islands of many semiconductor heterostructures (SHs) that are formed on the surface of a substrate of a different material during, what is now believed [15] to be a modified Stranski-Krastanow [18] growth.

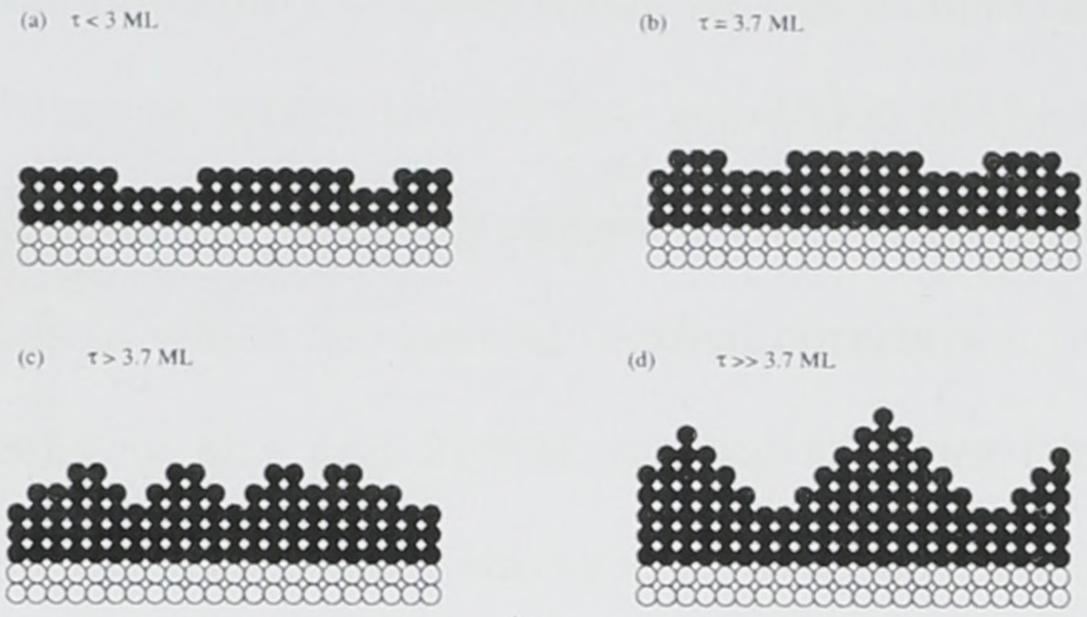

Figure 1.2: Schematic diagram of the growth of Ge (solid circles) on a Si (open circles) substrate. The initial 2D layer-by-layer growth takes place (a) up till the critical thickness for island formation $\tau = 3.7$ML (b), after which small islands nucleate on the flat 3.7ML of Ge (c), which turn to 3D islands (d) while leaving 3.0 ML of 2D Ge. (Taken from reference [19])

This growth mode is illustrated schematically, for the case of SiGe, in figure (1.2). The growth proceeds via the successive MBE layer deposition of material 1 on a substrate of material 2. Under particular growth conditions, such as temperature, growth rate, sample orientation and mode of deposition, the lattice mismatch between material and substrate causes the two dimensional growth to change to a three dimensional one once a critical thickness τ is reached. The critical thickness, τ, depends on the particular heterostructure and the three dimensional growth results in the spontaneous formation of coherent, i.e. dislocation free, islands of material 1 [20] that are pyramidal, truncated-pyramidal, or hemispherical (lens) in shape with a thin wetting layer left beneath the islands. The quantum dot islands are capped with a layer of the substrate material. In the case of InAs/GaAs quantum dots, which are the main focus of this project, there is a 7% mismatch between GaAs and InAs and the critical thickness has been reported to be between $1.5 - 1.8$ monolayers (ML) of InAs [21]. Theoretical analyses have shown that under the approriate growth conditions coherent islands are not only energetically more stable than both the strained epitaxial film and dislocated islands, but also favored kinetically over the nucleation of dislocations [22, 23].

The size and position uniformity of these quantum dot islands can be greatly improved through the use of multilayers, where the vertical repetition of the film acts as a selective filter for both size and spacing. This results in a three dimensional array of coherent three dimensional islands in which the partial vertical correlation of the islands continues to improve the uniformity in size and lateral spacing as more layers are added [5]. In fact it is now possible to fabricate, using suitable growth conditions, arrays and stacks of small quantum dots ($\sim$ 10nm) that are ordered in size and shape with high area densities ($> 10^{11}\text{cm}^{-2}$) and high optical quality, and suitable for creating devices such as low threshold lasers [15].

1.3 Optical properties of quantum dots

In this section a brief outline of the advantages of quantum dots over other low dimensional structures will be given, from the point of view of their optical properties.

First, consider quantum wells where the confinement of the charge carriers motion along one direction gives rise to a set of subbands, see figure (1.3), as opposed to the three dimensional energy bands of bulk semiconductors, photon emission can be obtained in electron or hole intersubband transitions. The energy separation of these subbands can be tuned to obtain photon energies covering most of the infrared spectrum by altering the layer thickness a [5]. However, at lower frequencies problems arise due to the increase of non-radiative processes. The energy separation between the subbands becomes of the order of the longitudinal optical (LO) phonon energies, where a low momentum phonon can be emitted in a vertical transition, which increases the electron-LO phonon scattering rate. The quantum efficiency is further reduced by the increase in the non-radiative process of electron-electron scattering as well as a decrease in the radiative rate [24]. Furthermore, the energy separation of the subbands does not need to be equal to the LO phonon energy for non-radiative relaxation to occur. This is due to the dispersion curve of the subbands which allow the emission of LO phonons whether the subband separation is greater or

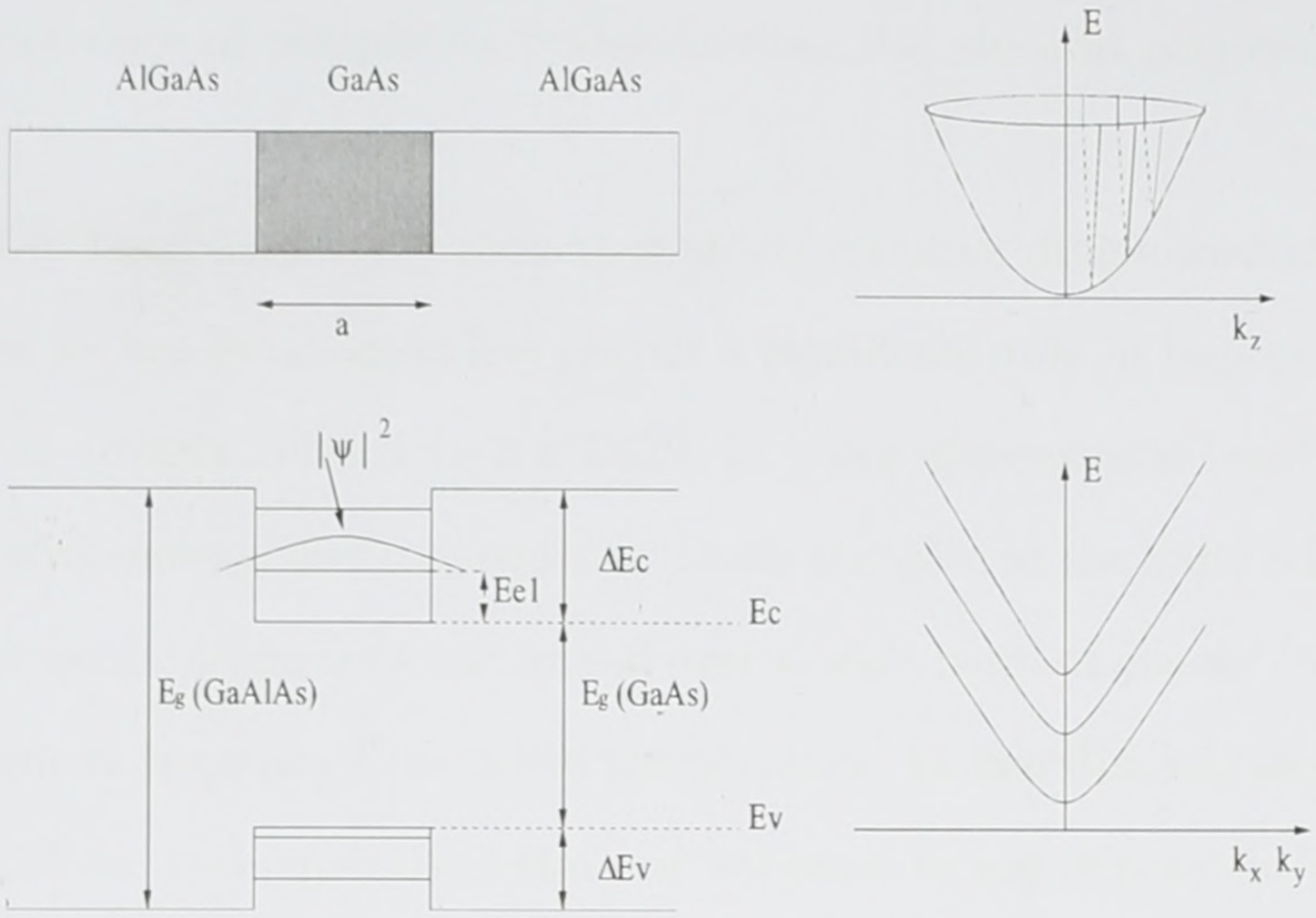

Figure 1.3: Schematic illustration of conduction band structure of GaAs quantum well of width a sandwiched between thick barriers of GaAlAs. The total energy of a conduction band electron is $E = E_{e,n} + \hbar^2/2m^*(k_x^2 + k_y^2)$ where $E_{e,n} = \hbar^2/2m^*(n\pi/a)$ and z is the direction perpendicular to the interface.

smaller than the LO phonon energy. Even so the quantum efficiency of such systems can be improved, and indeed emission in the THz region via intersubband transitions has been observed [25].

In contrast to two and three dimensional systems, where hot carriers are able to relax easily to the band edges through optical phonons followed by acoustical phonons [26], zero dimensional quantum dot systems have no energy dispersion but rather have well-defined, sharp levels in **k** space with a delta-like density of states [27]. It was initially thought that this discrete nature of the DOS would impede carrier relaxation once they are captured by the quantum dots. The argument being that the interlevel spacing is too large for efficient acoustic phonon emission, and that there is no reason that the energy separation should match the energy of LO phonon energy [26, 28], hence resulting in an enhancement of the quantum efficiency through the engineering of the interlevel spacing. However, experimental results have since shown that relaxation from excited dot states to the ground state is very rapid, similar to quantum wells [29, 30]. This merely emphasises

the crucial importance of completely understanding the physical properties of quantum dots.

In the field of laser diodes the reduction of the effective dimensionality of the active layer from three to two dimensions has played a significant role in improving device performance, and is directly related to the DOS. In three dimensional band structures the DOS increases with energy, and consequently limits the gain at the band edge lasing wavelength since the available carriers are spread over a wide band of energy thus limiting the population inversion because of the finite temperature. In two dimensional quantum well systems the DOS for each quantised state or subband is not dependent on energy, and the carriers more readily able to collect at the band edge thus increasing the gain at the lasing wavelength as compared to the three dimensional case [28].

It is predicted that a semiconductor laser diode with a large density of "perfect" QDs will have optimum properties, i.e. a low and temperature-insensitive threshold current and a large modulation bandwidth [31]. Perfect in this context implies that all the dots are identical and have a deep confining potential. The underlying reason for this predicted behaviour is again related to the DOS, since for a homogeneous ensemble of QDs, the DOS has a sharp peak at the band edge transition energy. This means that only two electrons per dot need to be excited over the energy gap to achieve population inversion, which is also true for high temperatures provided that the confining potential is sufficiently deep [28]. However, the realisation of such an array of QDs presents a considerable technical challenge. Nevertheless, QD lasers that emit continuous wave at room temperature have been realised and the properties of the diodes have significantly improved since the first reports of laser action [15]. In addition, low temperature thresholds have been reported which compare very favourably with the best quantum well laser diodes [15] and this is very clearly a direct consequence of the carrier confinement in the QD [32]. Also, much higher powers have been realised by QD lasers than with QW lasers [28].

Another possible application of QDs is in quantum cryptography where there is a pressing need for single photon sources. Quantum cryptography uses either the polari-

sation, or the phase, of single photons as the means of communication and can achieve almost completely secure transmission [33]. The basic principle is that the sender rotates his basis randomly thus making it impossible for an interceptor to detect and accurately recreate a photon [28]. In order for this technology to become possible a single photon emitter is required. Prototype systems employ a highly attenuated laser as the source but this is both inefficient and insecure because a large majority of pulses are empty and a sizable fraction contain two photons [28].

A photon source consisting of a single QD can in principle overcome these limitations. One approach is to excite a QD with a laser pulse intense enough that the probability of capturing at least one exciton is very close to one [34]. Since highly excited QDs decay by emitting a series of photons with different energies, this enables the selection of the final photon through the use of spectral filtering, and this photon can then be used for communication [28]. This concept has been explored experimentally, and for low temperatures, photons on demand have been generated from individual QDs [35–37].

Quantum dots have the capability of confining individual electrons or holes and it might be possible to exploit this characteristic in the production of a memory element with a bit being represented by a single electron in a single QD. The underlying principle for an optically based quantum dot-based memory storage device is to separate an electron and a hole in an optically excited electron-hole pair with a strong electric field. One route towards achieving this is through the use of vertically oriented QDs in a field-effect heterostructure, where the electric field can be varied simply through a voltage applied to the gate electrode. On illumination, the write part of the process, a large negative bias is applied to generate a high electric field in the device. Thus, resulting in the QDs in one layer trapping one or more electrons and dots in another layer trapping one or more holes. After illumination a positive bias is applied causing the electrons to tunnel to the dots containing the holes. The electrons and holes then recombine generating light, which is the read part of the process [28]. Indeed this approach has been implemented using

a layer of self-assembled QDs and an adjacent quantum well [38] and vertically oriented self-assembled QDs [39].

1.4 Size and shape of SAQD

There is a wealth of experimental data available on InAs/GaAs QDs since the Stranski-Krastanow growth method [18] has simplified the fabrication of samples with narrow size and uniform density distributions. Various sizes and shapes, depending on the growth conditions, have been reported for these QDs. Grundmann et al. [40] have grown dots which were observed to be square-based pyramids with typical base width of 120 Å and a height of 60 Å by high-resolution transmission electron microscopy (TEM). The pyramidal dots investigated by Moison et al. [41] were shown to have a base width of 240 Å and a height of 30 Å by atomic force microscopy(AFM). Leonard et al. [42] fabricated hemispherical or lens shaped dots with a typical base diameter of 200 Å and a height of 50 Å as indicated by AFM measurements. The InAs dots investigated by Fricke et al. [43] were estimated, from atomic force micrographs, to be lens shaped with approximate dimensions of 200 Å in diameter and 7 Å in height. Sauvage et al. [44] reported that the dots investigated in their work were square based pyramids before GaAs regrowth, and lens shaped after the regrowth with a smaller size than that indicated by AFM, due to GaAs regrowth quenching the evolution of the islands. Capping could also result in the slight elongation of the dots as a consequence of the extreme anisotropy of InAs islands grown on GaAs for submonolayer coverage [43]. Experimental data, in the form of far-infrared (FIR) spectra, on the associated breaking of the symmetry in the first and second excited electronic states have been reported [43].

Liu et al. [45] utilised cross-sectional scanning tunnelling microscopy (STM) to examine their nominally $In_{0.5}Ga_{0.5}As$ buried dots and reported them to be truncated pyramids with an In-rich core of an inverted-triangle/cone shaped profile. Kegel et al. [46] have also reported a continuously varying composition, from GaAs at the base of the dot to

InAs at the top, for their InAs free-standing rotationally symmetric islands. However, the strain distribution obtained from their sample was consistent with a laterally homogeneous composition but not with an inverted cone In-profile [46].

Recently, Wang et al. [47] used AFM to show that despite the random spatial distribution of InAs islands formed during the growth of the first layer of QDs on GaAs substrates, it is possible to exploit the tendency of QDs to vertically align themselves during the growth of subsequent stacked layers to fabricate relatively long *chains*, about 2μm long, of InAs dots with an average size of 3.4 Å in height and 350 Å in diameter.

The tools utilised to investigate QD can be classed into two groups. On one hand there are techniques such as AFM and STM which allow the direct observation of QDs. However, they require that the samples be uncapped while the samples used in experimental measurements are capped. The usual procedure is to grow two samples under the same conditions and to cap one of them for use in measurements, while leaving the other uncapped for structural investigation. From the previous discussion it is clear that the capping process may introduce both size and shape variations in the islands thus limiting the usefulness and accuracy of the structural investigations [2].

On the other hand structural information on capped QDs can be obtained through the use of analysis techniques such as TEM. The images in this case are formed by a convolution of the strain contrast with atomic number dependent contrast, which tends to overestimate dot dimensions and does not give a good estimate of the composition [2, 5].

It is worth emphasising the importance of both the size and shape of QDs which can, and do, modify the interlevel spacing in the conduction and valence bands. This is especially true of theoretical calculations, where the exact shape and dimensions of QDs are essential to obtaining accurate descriptions of their electronic structure. It is thus of crucial importance that one exercise caution when comparing theoretical predictions with experimental data choosing only those exhibiting characteristics which the model or calculation aims to reproduce. It follows that depending on the particular method for accounting for the different parameters, such as confining potential, shape, size etc. , different electronic

structures have been theoretically predicted. The situation is further complicated by the shape of the photoluminescence (PL) spectra, usually fitted to a Gaussian distribution, which in the best cases has a full width at half maximum (FWHM) of about 50 meV, due to size fluctuations of the QDs in the sample. In some cases [48] the spectrum could not be fitted to a Gaussian but was resolved rather into a forest of narrow lines extending over an 80 meV range. In a narrower range of this particular spectrum, about 20 meV, about 90 peaks were observed with each of them being attributed to the emission of a specific InAs QD. In most cases this energy range combined with the fluctuations in QD size is too broad to distinguish between different theoretical predictions, in other words the right value can be found to support all of the different models. Thus far only the main feature of the PL spectra has been discussed, and this strong signal is attributed to the emission from the dots' ground state. There is still some debate on the origin of the higher energy spectral features. For example, they have been attributed to the transitions between the electronic ground state and several hole states which are allowed by the lack of symmetry along the growth axis [49], while they have also been identified with transitions between states with the same quantum number [50].

These are only some of the issues that are still open. Quantum dots are potentially useful for a number of different technologies. However, at present they have no established application but there are a number of interesting areas and as such it is of crucial importance that their physical properties, such as the number and position of the energy levels and their dependence on the dot characteristics are completely understood, thus providing great opportunities for producing original research.

Chapter 2

Frameworks/Methods of Solution

Energy band theory has more than seventy years of history, ever since 1928 when Bloch applied quantum physics to calculate the electronic band structure of solids [51]. Almost all of the recent theoretical approaches to the study of semiconductors are based on fundamental energy band theory. In the late 1950s the progress of experimental techniques opened the way for the growth of nearly perfect crystals and the use of new methods for performing experimental measurements on crucial parameters such as effective electron and hole masses, energy band dispersion and made possible the study of electronic states in general. More recently the advancement in computer technology has enabled the performance of increasingly complex electronic band structure calculations [5].

This chapter presents a brief introduction and overview of the most successful approaches in the study of semiconductor systems, along with a mathematical overview of two of the more commonly used numerical methods for the solution of the Schrödinger equation which forms the basis for any theoretical investigation.

2.1 $\mathbf{k} \cdot \mathbf{p}$ Theory

The $\mathbf{k} \cdot \mathbf{p}$ method was originally a device for exploring the properties of energy bands and wave functions in the vicinity of some important point in $\mathbf{k}$ space [52], at an energy

extremum (usually the Γ point) [53], with the aid of perturbation theory. The method follows in a straightforward fashion from the Bloch form of the wave function. When electrons are excited from the valence band to the conduction band, the holes remain near the top of the valence band and the electrons near the bottom of the conduction band, see figure 2.1. In all direct-band semiconductors the maximum of the valence band is at the Γ point, or centre of the first Brillouin zone, and the minimum of the conduction band is also at the Γ point [54]. Thus, the holes at the top of the valence band are in Bloch states, as are the electrons at the bottom of the conduction band. Hence, for the description of low energy charge carriers only the band structure near the Γ point needs to be known [54].

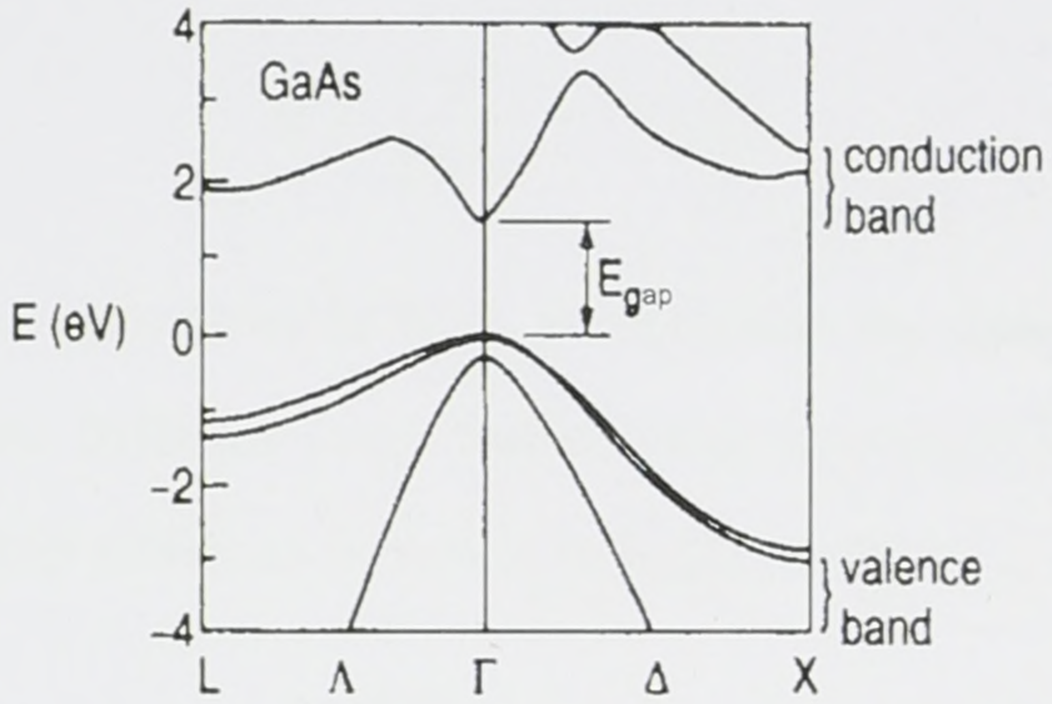

Figure 2.1: Top of the valence band and bottom of conduction band for GaAs (taken from Wenckebach, 1999 [54]).

The $\mathbf{k} \cdot \mathbf{p}$ method, used with symmetry considerations, shows that the band structure in the vicinity of a point in $\mathbf{k}$ space depends on a small number of parameters (band gaps and masses) which can be accurately determined by experiment [52]. More recently it has been used to investigate the electronic structure of unstrained quantum wires [55] and strained quantum wires [56].

Since the periodic part of Bloch functions, u_{nk}, forms a complete set of cell periodic functions for a given $\mathbf{k}$, it follows that if the momentum and energy matrix elements are known for a given $\mathbf{k}$, then the energy for the values of $\mathbf{k}$ are completely determined. This is called the $\mathbf{k} \cdot \mathbf{p}$ representation. The limitations of this empirical $\mathbf{k} \cdot \mathbf{p}$ method do not

arise from perturbation theory, but from how much of the $\mathbf{k} \cdot \mathbf{p}$ matrix can be empirically determined.

For a brief overview of the method, consider the single-electron Schrödinger equation for the Bloch functions

$$\phi_{n\mathbf{k}}(\mathbf{r}) = u_{n\mathbf{k}}(\mathbf{r})e^{i\mathbf{k}\cdot\mathbf{r}} \tag{2.1}$$

in a crystal with a periodic potential $V(\mathbf{r})$ is given by

$$H\phi_{n\mathbf{k}}(\mathbf{r}) = E_{n\mathbf{k}}\phi_{n\mathbf{k}}(\mathbf{r}) \tag{2.2}$$

where the Hamiltonian, H, is given by

$$H = \left[\frac{\mathbf{p}^2}{2m_0} + V(\mathbf{r})\right], \tag{2.3}$$

and $u_{n\mathbf{k}}(\mathbf{r})$ has the same periodicity as $V(\mathbf{r})$, n represents the different energy bands and $\mathbf{k}$ is restricted to the first Brillouin zone. Substituting equations (2.1) and (2.3) into the Schrödinger equation (2.2) yields an equation in $u_{n\mathbf{k}}(\mathbf{r})$ only,

$$\left[\frac{\mathbf{p}^2}{2m_0} + \frac{\hbar}{m_0}\mathbf{k}\cdot\mathbf{p} + \frac{\hbar^2k^2}{2m_0} + V(\mathbf{r})\right] u_{n\mathbf{k}}(\mathbf{r}) = E_{n\mathbf{k}}u_{n\mathbf{k}}(\mathbf{r}) \tag{2.4}$$

This can be rewritten as

$$(H + H')u_{n\mathbf{k}}(\mathbf{r}) = E_{n\mathbf{k}}u_{n\mathbf{k}}(\mathbf{r}) \tag{2.5}$$

where

$$H' = \frac{\hbar}{m_0}\mathbf{k}\cdot\mathbf{p} + \frac{\hbar^2k^2}{2m_0} \tag{2.6}$$

$\tilde{H} = H + H'$ is the new $\mathbf{k} \cdot \mathbf{p}$ Hamiltonian which has the same periodicity as that of the crystal lattice. Thus equation (2.5) need only be solved for a primitive cell, as opposed to equation (2.2) which has to be solved for the entire crystal. In addition, for states near the centre of the first Brillouin zone or Γ point, where $\mathbf{k} \to 0$, the second part of the

Hamiltonian, H', also tends to zero. Thus, perturbation theory can be used to obtain the eigenvalues and eigenfunctions of $\tilde{H}$ when H' is small.

For a single non-degenerate band, time independent perturbation theory gives the energy to second order in perturbation [5, 53],

$$E_{n\mathbf{k}} = E_{n\mathbf{0}} + \frac{\hbar^2 k^2}{2m_0} + \frac{\hbar}{m_0}\mathbf{k}\cdot\mathbf{p}_{nn} + \frac{\hbar^2}{m_0^2}\sum_{n'\neq n}\frac{|\mathbf{k}\cdot\mathbf{p}_{nn'}|^2}{E_{n\mathbf{0}} - E_{n'\mathbf{0}}} \tag{2.7}$$

and the wave function to the first order in perturbation,

$$u_{n\mathbf{k}}(\mathbf{r}) = u_{n\mathbf{0}}(\mathbf{r}) + \sum_{n'\neq n}\frac{\hbar}{m_0}\frac{\mathbf{k}\cdot\mathbf{p}_{nn'}}{E_{n\mathbf{0}} - E_{n'\mathbf{0}}}u_{n'\mathbf{0}}(\mathbf{r}), \tag{2.8}$$

where $\mathbf{p}_{nn'}$, the momentum matrix elements are defined as

$$\mathbf{p}_{nn'} = \int_{unitcell} u^*_{n\mathbf{0}}(\mathbf{r})\mathbf{p}u_{n'\mathbf{0}}(\mathbf{r})\,\mathrm{d}^3\mathbf{r} \tag{2.9}$$

and $u_{n\mathbf{k}}(\mathbf{r})$'s are normalised as

$$\int_{unitcell} u^*_{n\mathbf{0}}(\mathbf{r})u_{n'\mathbf{0}}(\mathbf{r})\mathrm{d}^3\mathbf{r} = \delta_{nn'} \tag{2.10}$$

If $\mathbf{k} = 0$ is at an extremum of $E_{n\mathbf{k}}$, then $E_{n\mathbf{k}}$ must depend quadratically on $\mathbf{k}$ near $\mathbf{k} = 0$ and $\mathbf{p}_{nn} = 0$. This is the reason why second-order perturbation theory is needed for the energy correction, and only first-order for the wave function. Since $\mathbf{k}$ is set to zero,

$$E_{n\mathbf{k}} - E_{n\mathbf{0}} = \sum_{\alpha,\beta} D^{\alpha\beta}k_\alpha k_\beta = \frac{\hbar^2}{2}\sum_{\alpha,\beta}\left(\frac{1}{m^*}\right)_{\alpha\beta}k_\alpha k_\beta \tag{2.11}$$

and

$$D^{\alpha\beta} = \frac{\hbar^2}{2m_0}\delta_{\alpha\beta} + \frac{\hbar^2}{2m_0}\sum_{n'\neq n}\frac{p^\alpha_{nn'}p^\beta_{n'n} + p^\beta_{nn'}p^\alpha_{n'n}}{E_{n\mathbf{0}} - E_{n'\mathbf{0}}} = \frac{\hbar^2}{2}\left(\frac{1}{m^*}\right)_{\alpha\beta} \tag{2.12}$$

where $\alpha, \beta = x, y$ and z . The matrix $D^{\alpha\beta}$ is the inverse effective mass in matrix form multiplied by $\hbar^2/2$.

The above formulation ignores the spin-orbit interaction, which is taken into account by Kane's model [57] for direct-band semiconductors. It introduces a term into the Hamiltonian H, to account for this spin-orbit interaction, of the form

$$H_{so} = \frac{\hbar^2}{4m_0^2c^2}\,\sigma \cdot (\nabla V \times \mathbf{p}), \tag{2.13}$$

where σ is the spin operator. Thus, an additional term appears in H' of the form

$$H'_{so} = \frac{\hbar^2}{4m_0^2c^2}\,\sigma \cdot (\nabla V \times \mathbf{k}), \tag{2.14}$$

which, however, is small compared to the other terms since the crystal momentum $\hbar\mathbf{k}$ is very small compared to the atomic momentum $\mathbf{p}$ in the far interior of the atom where most of the spin-orbit interaction occurs. Thus, this term is usually neglected.

Finally, the Luttinger-Kohn model [58] applies the $\mathbf{k} \cdot \mathbf{p}$ formalism to the case of degenerate bands.

2.2 The pseudopotential method

The pseudopotential method is in essence a mathematical transformation where the real potential $V(\mathbf{r})$ is replaced by a pseudopotential $V^{PS}(\mathbf{r})$ while the energy of the system remains unchanged. By choosing an appropriate model for the pseudopotential the effect of the strong attractive potential in the neighbourhood of the core region is substantially reduced, while the behaviour of the pseudopotential and the real potential is the same between the core regions. The corresponding pseudowave functions have no rapid oscillations in the whole crystal space and they behave as the real functions outside the atomic core radius. In this way only a few plane waves are required to approximate the pseudowave functions.

Using Dirac notation, the ground state and lower states of an electron in a crystal satisfy

$$\hat{H}|\psi_{\mathbf{k}}\rangle = E_{\mathbf{k}}|\psi_{\mathbf{k}}\rangle \tag{2.15}$$

$$\hat{H}|\psi_c\rangle = E_c|\psi_c\rangle \tag{2.16}$$

where $\psi_{\mathbf{k}}$ are the wave functions of the energy band, ψ_c are the core wave functions and in the interests of simplicity only one energy E_c has been taken for the core level. The wave functions $\psi_{\mathbf{k}}$ and ψ_c are orthonormal and form a complete set and are expressed mathematically as,

$$\sum_{\mathbf{k}} |\psi_{\mathbf{k}}\rangle\langle\psi_{\mathbf{k}}| + \sum_{c} |\psi_c\rangle\langle\psi_c| = \hat{I} \tag{2.17}$$

where $\hat{I}$ is the identity operator and $\sum_c$ includes all the core wave functions ψ_c of all lattice sites.

Now, if $\psi_{\mathbf{k}}$ is expanded in terms of plane waves (PW) it is natural to modify them so that they are orthogonal to the core states ψ_c. Introducing the projection operator

$$\hat{P}_c = \sum_{c} |\psi_c\rangle\langle\psi_c|, \tag{2.18}$$

the orthogonalized plane waves (OPW) can be expressed as the plane waves minus their projection on the core electronic states, i.e.

$$\begin{aligned} |\mathbf{OPW}, \mathbf{G}+\mathbf{k}\rangle &= (\hat{I} - \hat{P}_c)|\mathbf{PW}, \mathbf{G}+\mathbf{k}\rangle \\ &= |\mathbf{PW}, \mathbf{G}+\mathbf{k}\rangle - \sum_{\mathbf{c}} |\psi_{\mathbf{c}}\rangle\langle\psi_{\mathbf{c}}|\mathbf{PW}, \mathbf{G}+\mathbf{k}\rangle \end{aligned} \tag{2.19}$$

where $\mathbf{G}$ is a reciprocal lattice vector and

$$\langle \mathbf{r}|\mathbf{PW}, \mathbf{k}\rangle = \frac{1}{\sqrt{\mathbf{N}\Omega}} \mathbf{e}^{\mathbf{ik.r}} \tag{2.20}$$

where Ω is the volume of the unit cell of the crystal lattice, and N the total number of primitive cells.

The first term on the right hand side of equation (2.19) is the plane waves far from the core region and the second term reflects the wave functions near the core. Thus $\psi_{\mathbf{k}}$ can be expanded as

$$|\psi_{\mathbf{k}}\rangle = \sum_{\mathbf{G}} a_{\mathbf{G}+\mathbf{k}} |\mathbf{OPW}, \mathbf{G}+\mathbf{k}\rangle. \tag{2.21}$$

Substituting equation (2.21) into equation (2.15) and making use of equation (2.19) yields

$$[\hat{T} + V + (E_{\mathbf{k}} - E_c)\hat{P}_c] \sum_{\mathbf{G}} a_{\mathbf{G}+\mathbf{k}} |\mathbf{PW}, \mathbf{G}+\mathbf{k}\rangle = E_{\mathbf{k}} \sum_{\mathbf{G}} a_{\mathbf{G}+\mathbf{k}} |\mathbf{PW}, \mathbf{G}+\mathbf{k}\rangle, \tag{2.22}$$

where $\hat{H} = \hat{T} + V$ is the crystal Hamiltonian. Therefore the pseudopotential is written as

$$\hat{V}^{PS} = V + (E_{\mathbf{k}} - E_c)\hat{P}_c \tag{2.23}$$

and the pseudowave function as

$$|\psi_{\mathbf{k}}^{PS}\rangle = \sum_{\mathbf{G}} a_{\mathbf{G}+\mathbf{k}} |\mathbf{OPW}, \mathbf{G}+\mathbf{k}\rangle. \tag{2.24}$$

Substituting equations (2.24) and (2.23) into equation (2.22) gives

$$[\hat{T} + \hat{V}^{PS}]|\psi_{\mathbf{k}}^{PS}\rangle = E_{\mathbf{k}}|\psi_{\mathbf{k}}^{PS}\rangle. \tag{2.25}$$

Equation (2.25) is identical to equation (2.15) except that the potential V is now replaced with the pseudopotential $\hat{V}^{PS}$. Multiplying equation (2.22) on the left by $\langle \mathbf{PW}, \mathbf{G}+\mathbf{k}|$ yields

$$\sum_{\mathbf{G}'} \left(\left[\frac{\hbar^2(\mathbf{G}+\mathbf{k})^2}{2m} - E_{\mathbf{k}} \right] \delta_{\mathbf{G}\mathbf{G}'} + \langle \mathbf{PW}, \mathbf{G}|\hat{V}^{PS}|\mathbf{PW}, \mathbf{G}'\rangle \right) a_{\mathbf{G}'+\mathbf{k}} = 0, \tag{2.26}$$

and the energy of the system is given by

$$\left|\left[\frac{\hbar^2(\mathbf{G}+\mathbf{k})^2}{2m} - E_{\mathbf{k}}\right]\delta_{\mathbf{GG'}} + \langle \mathbf{PW}, \mathbf{G}|\hat{V}^{PS}|\mathbf{PW}, \mathbf{G'}\rangle\right| = 0 \tag{2.27}$$

Thus the problem of finding the eigenfunctions and eigenvalues for a real system described by equation (2.15) can be replaced by that of finding the eigenfunctions and eigenvalues of a pseudosystem described by equation (2.25). In fact, the two systems have the same eigenvalue $E_{\mathbf{k}}$, which is restricted to only the energy bands without inclusion of the E_c [59]. The coefficients $a_{\mathbf{G}+\mathbf{k}}$ in the expansion of the pseudowave function in $|\mathbf{PW}\rangle$ are the same as the $a_{\mathbf{G}+\mathbf{k}}$ in the expansion of the real wave functions in $|\mathbf{OPW}\rangle$. The advantage of using this method is that only a few terms are required for the calculation of the band structure of a solid to achieve rapid convergence [59]. Furthermore if the crystal potential is expressed as a sum of all atomic potentials $U(\mathbf{r})$

$$V(\mathbf{r}) = \sum_j U(\mathbf{r} - \mathbf{r_j}), \tag{2.28}$$

the pseudopotential of the crystal can then be assumed to be the sum of all the atomic local pseudopotentials $U^{PS}(\mathbf{r} - \mathbf{r_j})$

$$\hat{V}^{PS} = \sum_j U^{PS}(\mathbf{r} - \mathbf{r_j}) \tag{2.29}$$

The pseudopotential method is considered as one of the most reliable techniques for calculating the electronic structure of semiconductors. Through the introduction of a few empirical parameters the calculated results of the overall band structure, electronic density of states, valence electron charge densities, etc. are usually in good agreement with experimental data.

2.3 Effective mass approximation

The effective mass approximation (EMA) is a standard and widely used procedure in which the band structure of the crystalline semiconductor is largely ignored, retaining only the energy and effective mass at the extremity of each band [60]. Referring to figure 2.1, at the extremity of each band it is always possible to approximate the band as a parabola; a fact on which this approximation relies heavily.

In order to arrive at the EMA, suppose a perturbation, in the form of an impurity or more generally a QW or QD, is added to a perfect crystal. Then the Schrödinger equation will take the form

$$(\hat{H}_0 + \hat{V}_{pert})\psi = E\psi \tag{2.30}$$

where $\hat{H}_0$ is the Hamiltonian for the perfect crystal and $\hat{V}_{pert}$ is the perturbation resulting from the impurity. For ease of notation consider a one-dimensional system. If the solution of the Schrödinger equation for the perfect crystal is given by

$$\hat{H}_0\phi_{nk}(x) = \varepsilon_n\phi_{nk}(x) \tag{2.31}$$

then the wave function $\psi(x)$ of the perturbed system can be expanded in terms of the complete set $\phi_{nk}(x)$. Thus,

$$\psi(x) = \sum_n \int_{-\frac{\pi}{a}}^{\frac{\pi}{a}} \tilde{\chi}_n(k)\phi_{nk}(x)\frac{\mathrm{d}k}{2\pi} \tag{2.32}$$

where $\tilde{\chi}_n(k)$ are the expansion coefficients. This expansion has both a summation over all bands n and an integration of k over the Brillouin zone in order to include all states. The first approximation is to assume that only the wave functions from one band play a significant role and hence the summation over n can be dropped. The second approximation is to assume that only states from a small region of k-space contribute significantly

to the integral. The Bloch functions can be written as

$$\phi_{nk}(x) = u_{nk}(x)e^{ikx} \tag{2.33}$$

which, assuming that most of the variation with k comes from the plane wave and that u_{nk} can be treated as being independent of k over a small region of k-space, can be rewritten as

$$\phi_{nk}(x) \approx u_{n0}(x)e^{ikx} = \phi_{n0}(x)e^{ikx} \tag{2.34}$$

for small values of k. Substituting equation (2.34) into equation (2.32) results in the wave function assuming the form of an inverse Fourier transform. This wave function can be approximated as the product of the Bloch function of the local extremum of the crystal energy band ϕ_{n0} and an *envelope function* $\chi(x)$ and this is the first major outcome of the EMA [60]. Mathematically this is expressed as

$$\psi(x) \approx \phi_{n0}(x)\chi(x) \tag{2.35}$$

To obtain an expression for the envelope function, equation (2.32) is substituted into the Schrödinger equation of equation (2.30). In three dimensions, after some simplifications that follow from the aforementioned approximations and making use of the parabolic approximation for the bottom of the conduction band, namely

$$\varepsilon_n(x) \approx E_c + \frac{\hbar^2 k^2}{2m_0 m_e}, \tag{2.36}$$

and making the substitution $k \to -i\nabla$ and m_e is the effective mass [60], the Schrödinger equation reduces to

$$\left[-\frac{\hbar^2}{2m_0 m_e}\nabla^2 + V_{pert}(\mathbf{r})\right]\chi(\mathbf{r}) = (E - E_c)\chi(\mathbf{r}). \tag{2.37}$$

This expression of the Schrödinger equation strongly resembles that for free electrons, except for the effective mass m_e, with the energy being measured from the bottom of the conduction band. The validity of this form of the Hamiltonian is limited by the parabolic approximation to the energy band and as such when considering cases at large energies from the band edge the approximation becomes dubious. The restriction to a single band is an approximation which is not suitable for some applications [60]. For example

- materials such as Si, that have several equivalent valleys in the conduction band, all of which must be retained for electronic states
- the valence band that contains light and heavy holes which are degenerate at the top and separated from a third or split-off band by only the weak spin-orbit coupling. The summation over all these bands must be retained in the wave function
- interband effects such as the optical absorption in a quantum well are described by taking into account both conduction and valence bands leading to the need to scrutinise the approximation made in equation (2.34) [60]

Note that in the case of several bands being retained the effective Hamiltonian becomes a matrix of differential equations acting on a vector consisting of the components of the wave function in each band.

In spite of these restrictions, investigation has shown that the EMA in its simplest form is robust and generally successful in describing the optical features of low dimensional systems, such as the absorption in QD. These can be treated by separately solving the single band Schrödinger equations for the conduction and valence bands and then combining the results to obtain the transition energies.

2.3.1 Effective mass theory in heterostructures

When applying the EMA to heterostructures the crucial point is the manner in which the envelope functions are matched at the interfaces between the two materials. If the materials were the same it would simply be a matter of matching both the value and the

derivative of the wave function at the interface. However, this condition is not correct for a heterojunction where the two effective masses are different and these conditions do not conserve the current. Consider a junction at $z = 0$ between material A and B, a correct set of matching conditions is

$$\chi(0_A) = \chi(0_B), \qquad \frac{1}{m_A}\frac{d\chi}{dz}(z)\bigg|_{z=0_A} = \frac{1}{m_B}\frac{d\chi}{dz}(z)\bigg|_{z=0_B} \tag{2.38}$$

where 0_A means the side of the interface in material A and so on. Since the derivative is in essence the momentum operator, equation (2.38) requires that the velocity be the same on both sides in order for the current to be conserved. Accordingly the Schrödinger equation takes the form

$$-\frac{\hbar^2}{2m_0}\nabla\left(\frac{1}{m^*}\nabla\right)\chi(\mathbf{r}) + V(\mathbf{r})\chi(\mathbf{r}) = E\chi(\mathbf{r}) \tag{2.39}$$

which is Hermitian and ensures that, among other things, the wave functions are orthogonal and that current is conserved [60].

2.4 Orthogonal periodic functions

This method for the solution of the Schrödinger equation, under the effective mass approximation, in the cases of quantum wires (QWW) and QD was first developed by Gershoni et al. [61], but has since been modified and widely used by a number of researchers [2,62,63]. It involves expanding the wave function in terms of a complete orthonormal set of functions. This method will now be discussed in more detail.

In the interests of simplicity consider the 2D case i.e. a quantum wire. A set of functions is said to be orthonormal if they satisfy the following condition,

$$\int_{\infty} \Phi_i^* \Phi_j \, \mathrm{d}x \, \mathrm{dy} = \delta_{ij} \tag{2.40}$$

where δ_{ij} is the Kronecker delta and is equal to 1 if $i = j$ and 0 otherwise. The orthonormality of a set of functions implies that any other function, in the same domain, may be expressed as a linear combination of this *basis set* [64]. Thus if a suitable basis set is chosen, any wave function in the system may be expanded in terms of this set.

Consider the single-particle 2D effective mass Schrödinger equation,

$$\left[\frac{-\hbar^2}{2}\nabla\left(\frac{1}{m^*(x,y)}\nabla\right) + V(x,y)\right]\psi(x,y) = E\psi(x,y) \tag{2.41}$$

$\psi(x,y)$ can then be expanded as a linear combination of a basis set $\Phi_l(x,y)$,

$$\psi(x,y) = \sum_l a_l \Phi_l(x,y) \tag{2.42}$$

where a_l are coefficients yet to be determined. In the system that Gershoni [61] investigated, $\Phi_l(x,y)$ were the product of sine and cosine functions which go to zero at the boundaries $x = \pm L_x$ and $y = \pm L_y$ which can be chosen without any loss of generality. These functions are the solutions to a rectangular wire with infinite height. Hence, the function $\Phi_l(x,y)$ could be expressed as,

$$\Phi_l(x,y) = u_m(x)u_n(y) \tag{2.43}$$

where

$$u_m(r) = \begin{cases} \sqrt{2/L_r}\,\sin(m\pi r/L_r), & m = 2,4,6,\ldots, \\ \sqrt{2/L_r}\,\cos(m\pi r/L_r), & m = 1,3,5,\ldots, \end{cases} \tag{2.44}$$

with a simple one-to-one mapping between the subscripts (m,n) and l is applied.

Now, substituting equations (2.44) and (2.43) into equation (2.41), left multiplying by Φ_l and integrating using the orthonormality condition of equation (2.40) allows the conversion of the partial differential equation into a matrix equation of the form,

$$(M_{ll'} - E\delta_{ll'})a_l = 0 \tag{2.45}$$

where the matrix $M_{ll'}$ is given by,

$$M_{ll'} = \frac{-\hbar^2}{2}\left[\int \Phi_l \left(\nabla \frac{1}{m^*}\right) \nabla \Phi_{l'}\, \mathrm{d}x\, \mathrm{d}y + \int \Phi_l \left(\frac{1}{m^*}\right) \nabla^2 \Phi_{l'}\, \mathrm{d}x\, \mathrm{d}y\right] + \int \Phi_l V \Phi_{l'}\, \mathrm{d}x\, \mathrm{d}y \quad (2.46)$$

Depending on the forms of the potential $V(x, y)$ and the effective mass $m^*(x, y)$, the above integrals can be calculated to generate all the matrix elements. The eigenvalues can then be calculated by direct diagonalisation of the aforementioned Hamiltonian matrix. In the case demonstrated by Gershoni [61] all the above integrals could be performed analytically by using standard software tools, and 15 waves were used in each direction for the expansion.

Even though the method is extendible to 3D [2], the computation time and demand on memory are increased significantly by doing so. A basis set of N elements in 1D becomes N^2 in 2D and N^3 in 3D. Thus, in 3D it is necessary to set and diagonalise a matrix of N^6 elements which, besides being time consuming, also requires a large amount of computer memory. The number of waves that have to be used in each direction can be reduced by selecting basis sets which are more suitable for the system under investigation. For example, Gangopadhyay [62] used the solutions for an infinitely deep quantum wire in the shape of right-angled isosceles triangle, as the basis set when solving for finite barrier triangular and arrowhead shaped quantum wires. It was found that only a 9×9 matrix was needed to obtain a convergent solution for the triangular wire and a 42×42 matrix for the arrowhead shaped wire [62].

2.5 Fourier expansion

In this method the wave function is also expressed in terms of a basis set. The basis set in this case is the plane wave Fourier series. However, the Hamiltonian used in this case [65] is different from the one described in the previous section.

Starting with the general 3D Schrödinger equation given by equation (2.48), the problem was reduced to 2D since the system under investigation was a quantum wire, see figure 2.2. The effective potential now depends on the "longitudinal" wave number k_z. The motion along the z direction is free particle like, thus the energy depends on the wave number k_z and the remainder of the energy dependence on the wave number is parameterised by k_n, a dummy variable. Thus, k_n can be defined as

$$E = \frac{\hbar^2}{2m_2}(k_z^2 - k_n^2) \tag{2.47}$$

To derive the 2D equation, first consider the 3D Schrödinger equation of the form

$$-\frac{\hbar^2}{2}\nabla\left(\frac{1}{m(x,y)}\nabla\right)\phi(x,y,z) + V(x,y)\phi(x,y,z) = E\phi(x,y,z) \tag{2.48}$$

where $m(x,y)$ is the variable effective mass which is only dependent on x and y, $V(x,y)$ is the 2D confining potential, and $\phi(x,y,z)$ is the 3D wave function. Since the potential along the x and y directions may be expressed separately from that in the z direction, then the wave function may be expressed as,

$$\phi(x,y,z) = e^{ik_z z}\psi(x,y) \tag{2.49}$$

where the exponential term represents the wave function in the z direction, and $\psi(x,y)$ is the as yet unknown 2D wave function. It can be shown that equation (2.48) reduces to,

$$-\left(\nabla\frac{m_2}{m(x,y)}\right)\nabla(e^{ik_z z}\psi(x,y)) - \frac{m_2}{m(x,y)}\nabla^2(e^{ik_z z}\psi(x,y)) + \left(\frac{2m_2}{\hbar^2}\right)V(x,y)e^{ik_z z}\psi(x,y) = (k_z^2 - k_n^2)e^{ik_z z}\psi(x,y) \quad (2.50)$$

Working out the derivatives, dividing both sides by the exponential term and collecting terms in k_z^2 yields,

$$-\left[\frac{m_2}{m(x,y)}\right]\left[\frac{\partial^2\psi}{\partial x^2}+\frac{\partial^2\psi}{\partial y^2}\right] - \frac{\partial}{\partial x}\left[\frac{m_2}{m(x,y)}\right]\frac{\partial\psi}{\partial x} - \frac{\partial}{\partial y}\left[\frac{m_2}{m(x,y)}\right]\frac{\partial\psi}{\partial y} + U_{eff}(x,y)\psi = -k_n^2\psi \quad (2.51)$$

where m_1 is the electron effective mass in the wire and m_2 is the effective mass in the barrier semiconductor, used here for scaling [66], $m(x,y)$ is the position-dependent electron effective mass, and U_{eff} is the effective potential given by,

$$U_{eff} = \begin{cases} \frac{2m_2}{\hbar^2}V(x,y) & \text{in bulk,} \\ \frac{2m_2}{\hbar^2}V(x,y) + k_z^2\left[\frac{m_2}{m_1}-1\right] & \text{in wire.} \end{cases} \quad (2.52)$$

The wave function is then expanded in terms of a plane-wave basis set, chosen to satisfy the boundary conditions

$$\psi(\pm w_x, y) = 0, \ \text{ for } 0 < |y| < w_y; \qquad \psi(x, \pm w_y) = 0, \ \text{ for } 0 < |x| < w_x \quad (2.53)$$

where the barrier layer ends at $\pm w_x$ and $\pm w_y$ [66]. While plane-wave expansions are applicable to wires of any cross-section, advantage was taken of the symmetry of the rectangular wire under investigation [65]. The wave functions must thus be of either even or odd parity in the x and y directions, and therefore only the following four types of

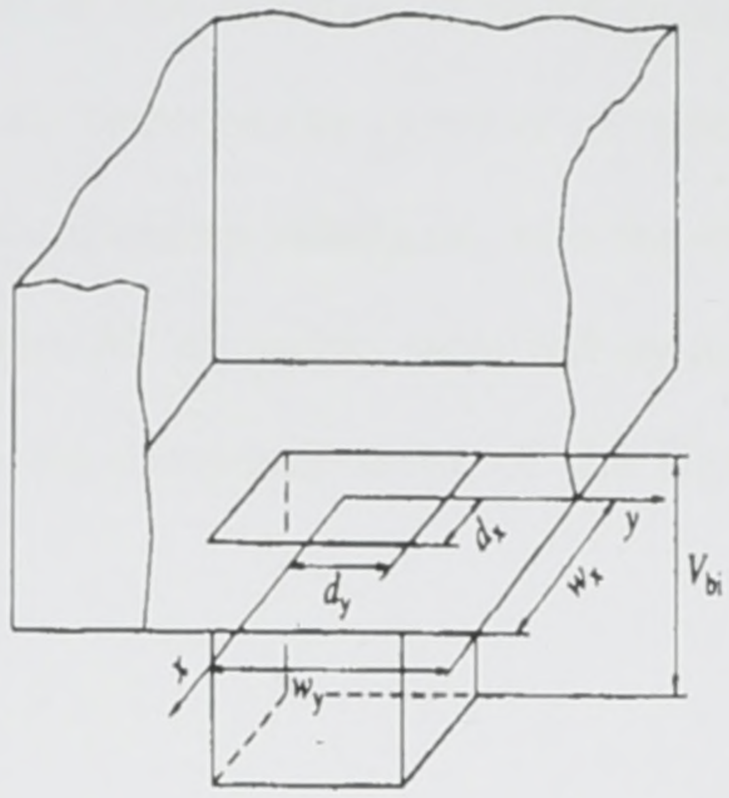

Figure 2.2: A schematic view of quantum wire under investigation (taken from Tadič et al. [66]), with dimensions $2w_x \times w_y$ and core dimensions $2d_x \times 2d_y$ and built-in potential V_{bi}.

sine-cosine plane-wave expansions were allowed (taking the centre of the quantum wire as the origin):

$$\psi = \frac{1}{\sqrt{w_x w_y}} \sum_{j=1}^{n} \sum_{k=1}^{n} a_{jk}^{cc} \cos\left[i_x \frac{\pi}{w_x} x\right] \cos\left[i_y \frac{\pi}{w_y} y\right] \tag{2.54}$$

$$\psi = \frac{1}{\sqrt{w_x w_y}} \sum_{j=1}^{n-1} \sum_{k=1}^{n-1} a_{jk}^{ss} \sin\left[j \frac{\pi}{w_x} x\right] \sin\left[k \frac{\pi}{w_y} y\right] \tag{2.55}$$

$$\psi = \frac{1}{\sqrt{w_x w_y}} \sum_{j=1}^{n} \sum_{k=1}^{n-1} a_{jk}^{cs} \cos\left[i_x \frac{\pi}{w_x} x\right] \sin\left[k \frac{\pi}{w_y} y\right] \tag{2.56}$$

$$\psi = \frac{1}{\sqrt{w_x w_y}} \sum_{j=1}^{n-1} \sum_{k=1}^{n} a_{jk}^{sc} \sin\left[j \frac{\pi}{w_x} x\right] \cos\left[i_y \frac{\pi}{w_y} y\right] \tag{2.57}$$

where the superscripts of the Fourier coefficients denote the expansion type, and i_x and i_y are,

$$i_x = \frac{2j-1}{2}, \quad i_y = \frac{2k-1}{2}. \tag{2.58}$$

Using these expansions it was found that calculations need only be done in a single quarter of the quantum wire, with the situation in the remainder of the structure being known by symmetry. The advantage of using this kind of expansion over a single unsep-

arated basis set is the reduction of the number of mesh points (i.e. Fourier coefficients). Also, using this symmetrical basis reduces the number of components in each direction by half. Thus, each of the four Hamiltonian matrices, one for each symmetry type, contain $\left(\frac{N}{2}\right)^6$ elements as compared to the N^6 elements required by an unseparated basis set. The eigenvalues are found by the direct diagonalisation of the Hamiltonian matrices.

2.6 Conclusion

This chapter presented a brief introduction to the most successful theoretical approaches in the study of semiconductor systems. These included the $\mathbf{k} \cdot \mathbf{p}$ theory, which was originally a device for exploring the properties of energy bands and wave functions at some important point in $\mathbf{k}$ space [52]. Next was the pseudopotential method, which at heart is a mathematical transformation by which only a few plane waves are required to approximate the pseudowave functions, which is of particular importance in the neighbourhood of the core region. The effective mass approximation (EMA) was then discussed, and is a standard procedure used to approximate the band structure of crystalline semiconductors by only retaining the effective masses and the energy at the extremity of each band. Particular attention was paid to the EMA in heterostructures. A mathematical overview of the two more commonly used numerical methods for the solution of the Schrödinger for QD systems was then presented. Namely, these were the expansion of the wave function in terms of orthogonal period functions [5], and the expansion of the wave function in terms of plane wave Fourier series [65, 66]. The main disadvantages of these methods is that they scale as N^6 and $(\frac{N}{2})^6$ when extended to three dimensions respectively, and hence have large memory requirements.

Chapter 3

Quantum Wires

3.1 Introduction

Finite difference methods have been used to solve partial differential equations for a considerable length of time. They are basically, numerical methods which utilise the expansion of derivatives in terms of finite differences. In this chapter a new implementation of the finite difference method is developed, and discussed, for solving the time-independent, constant effective mass Schrödinger equation. The motivation behind this approach is to develop a computational technique which is fast to execute and light on memory. This technique has the advantages of being easy to implement, scales as N^3 when extended to three dimensions as opposed to N^6 for orthogonal periodic functions (N in the case of this method being the number of mesh points in each direction), all the matrices generated are sparse so its computation time compares favourably with other methods. Also this method is readily expandable to larger spatial areas and completely general three-dimensional potentials.

3.2 Finite difference method in two dimensions

3.2.1 Finite difference expansion of Schrödinger 's equation

The system under initial investigation, had the simplest possible geometry. It consisted of an infinitely deep rectangular cross-sectional wire. While this geometry is not really practical, it nevertheless provides a good starting point, since this method should be versatile enough to solve for any cross-section and any potential. In addition, analytical solutions are available for comparison [27]. The quantum wire used is shown schematically in figure 3.1.

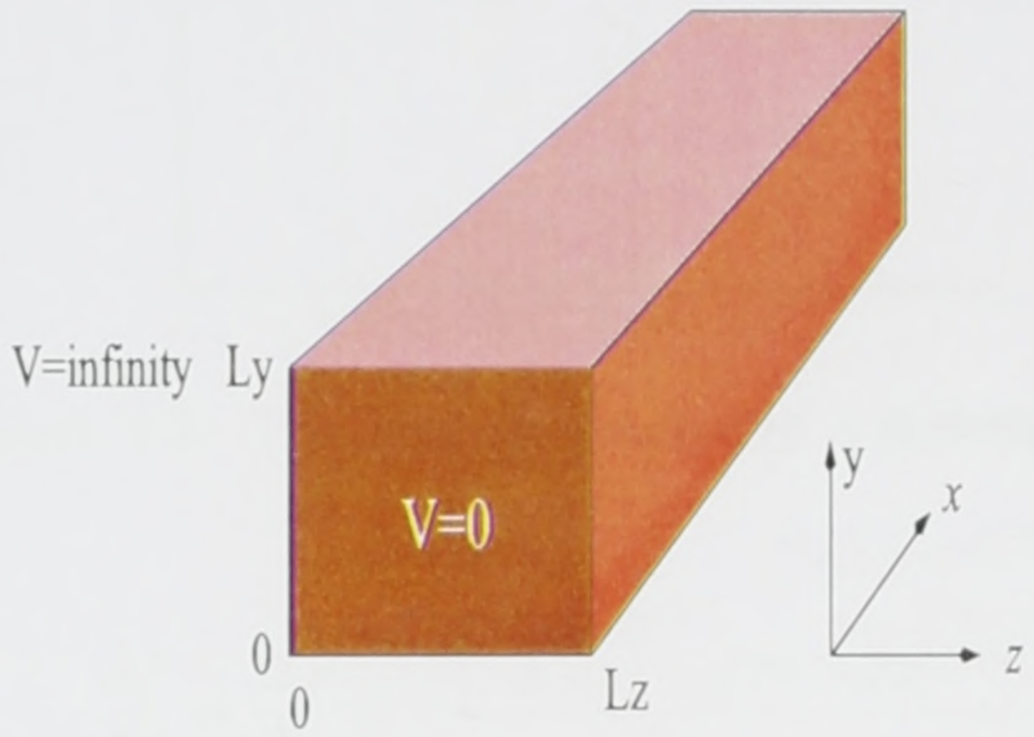

Figure 3.1: Infinitely deep rectangular cross-section quantum wire.

In this initial work, attention is focused on the general three-dimensional constant effective mass Schrödinger equation given by,

$$\frac{-\hbar^2}{2m^*}\nabla^2\psi(x,y,z) + V(x,y,z)\psi(x,y,z) = E_{x,y,z}\psi(x,y,z) \tag{3.1}$$

where m^* is the effective electron mass, and $V(x,y,z)$ the potential energy. Since, in the case under investigation, the potential is only a function of y and z then the variation along the length x of the wire can be decoupled [27], thus leading to a two-dimensional Schrödinger equation for the confinement within the cross-section of the wire, given by

$$\frac{-\hbar^2}{2m^*}\left[\frac{\partial^2\psi(y,z)}{\partial y^2} + \frac{\partial^2\psi(y,z)}{\partial z^2}\right] = \Big(E_{y,z} - V(y,z)\Big)\psi(y,z) \tag{3.2}$$

Now, consider expanding the first derivative of a general function $f(z)$ in terms of finite differences. Referring to figure 3.2, the first derivative is defined as:

$$\frac{\mathrm{d}f}{\mathrm{d}z} = \lim_{\Delta z \to 0} \frac{\Delta f}{\Delta z} \tag{3.3}$$

Using the approximate form of equation (3.3) yields,

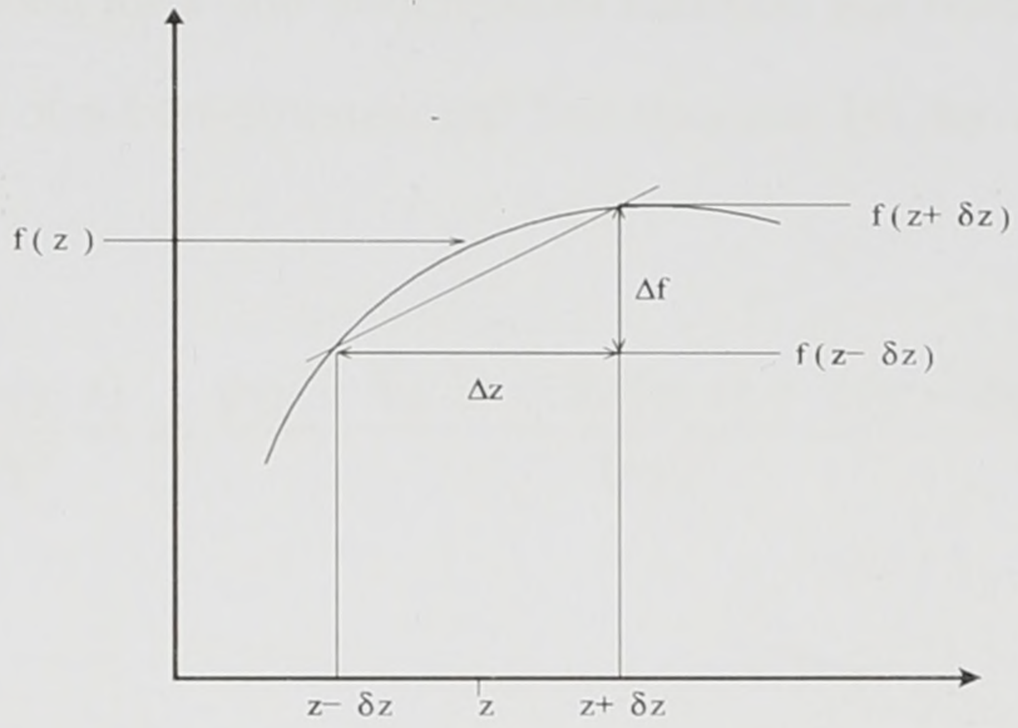

Figure 3.2: The first derivative of a function.

$$\frac{\mathrm{d}f}{\mathrm{d}z} \approx \frac{\Delta f}{\Delta z} = \frac{f(z+\delta z) - f(z-\delta z)}{2\delta z} \tag{3.4}$$

If f' is the first derivative, then the second derivative is given by,

$$\frac{\mathrm{d}f'}{\mathrm{d}z} \approx \frac{f'(z+\delta z) - f'(z-\delta z)}{2\delta z} \tag{3.5}$$

or more correctly,

$$\frac{\mathrm{d}^2 f}{\mathrm{d}z^2} \approx \frac{\frac{\mathrm{d}f}{\mathrm{d}z}|_{z+\delta z} - \frac{\mathrm{d}f}{\mathrm{d}z}|_{z-\delta z}}{2\delta z} \tag{3.6}$$

After some algebraic manipulation and using the finite difference expansion of equation (3.4) it can be shown that,

$$\frac{\mathrm{d}^2 f}{\mathrm{d}z^2} \approx \frac{f(z+2\delta z) - 2f(z) + f(z-2\delta z)}{(2\delta z)^2} \tag{3.7}$$

Since δz is a small arbitrary numerical value which is not yet defined, and it only appears in equation (3.7) with the factor 2, then in the interests of simplicity it is possible to substitute δz for $2\delta z$, reducing equation (3.7) to,

$$\frac{\mathrm{d}^2 f}{\mathrm{d}z^2} \approx \frac{f(z+\delta z) - 2f(z) + f(z-\delta z)}{(\delta z)^2} \tag{3.8}$$

Now that the expansion for a one-dimensional function has been derived, the expansion of the partial derivative of a two-dimensional function can be derived in a similar fashion, and is given by,

$$\frac{\partial^2 \psi(y,z)}{\partial y^2} \approx \frac{\psi(y+\delta y, z) - 2\psi(y,z) + \psi(y-\delta y, z)}{(\delta y)^2} \tag{3.9}$$

and by analogy,

$$\frac{\partial^2 \psi(y,z)}{\partial z^2} \approx \frac{\psi(y, z+\delta z) - 2\psi(y,z) + \psi(y, z-\delta z)}{(\delta z)^2} \tag{3.10}$$

Substituting equations (3.9) and (3.10) into the original Schrödinger equation (3.2), and making sure that the step lengths δy and δz are sufficiently small so that the approximation is valid,

$$\frac{-\hbar^2}{2m^*}\left[\frac{\psi(y+\delta y, z) - 2\psi(y,z) + \psi(y-\delta y, z)}{(\delta y)^2} + \frac{\psi(y, z+\delta z) - 2\psi(y,z) + \psi(y, z-\delta z)}{(\delta z)^2}\right] \approx \Big(E_{y,z} - V(y,z)\Big)\psi(y,z) \tag{3.11}$$

Multiplying equation (3.11) by $(\delta y)^2(\delta z)^2$ and rearranging yields the general form of the finite difference expansion of the Schrödinger equation and is given by,

$$(\delta y)^2\left[\psi(y,z+\delta z)+\psi(y,z-\delta z)\right]+(\delta z)^2\left[\psi(y+\delta y,z)+\psi(y-\delta y,z)\right] - \left[\frac{-2m^*}{\hbar^2}\Big(E_{y,z}-V(y,z)\Big)(\delta y)^2(\delta z)^2 + 2\big((\delta y)^2+(\delta z)^2\big)\right]\psi(y,z)=0 \quad (3.12)$$

Since δy and δz are arbitrary small numerical values, the problem represented by equation (3.12) can be further simplified by setting $\delta y = \delta z$. Making this substitution and rearranging,

$$\psi(y,z+\delta z)+\psi(y,z-\delta z)+\psi(y+\delta y,z) + \psi(y-\delta y,z)-\left[\frac{-2m^*}{\hbar^2}\Big(E_{y,z}-V(y,z)\Big)(\delta y)^2+4\right]\psi(y,z)=0 \quad (3.13)$$

In order to solve equation (3.13) numerically for $\psi(y,z)$, it is necessary to discretise the cross-section of the wire into blocks of length δz and height δy. The wave function is now mapped to the elements of this two-dimensional array. These array elements can now be labelled in the usual way, i.e. their corresponding row and column index (i,j). The value of δz is chosen so that the total width of the wire, L_z, is represented by the total number of columns, n_1+2. Similarly, δy is chosen so that the total height of the wire, L_y, is represented by the total number of rows, n_2+2. This arrangement is shown schematically in figure 3.3. For ease of notation, the value of the wave function at each array point is now labelled by its corresponding row and column index, i.e. (i,j). Thus, rewriting equation (3.13) in terms of these indices yields,

$$\psi_{i,j+1}+\psi_{i,j-1}+\psi_{i-1,j}+\psi_{i+1,j}-k\psi_{i,j}=0 \quad (3.14)$$

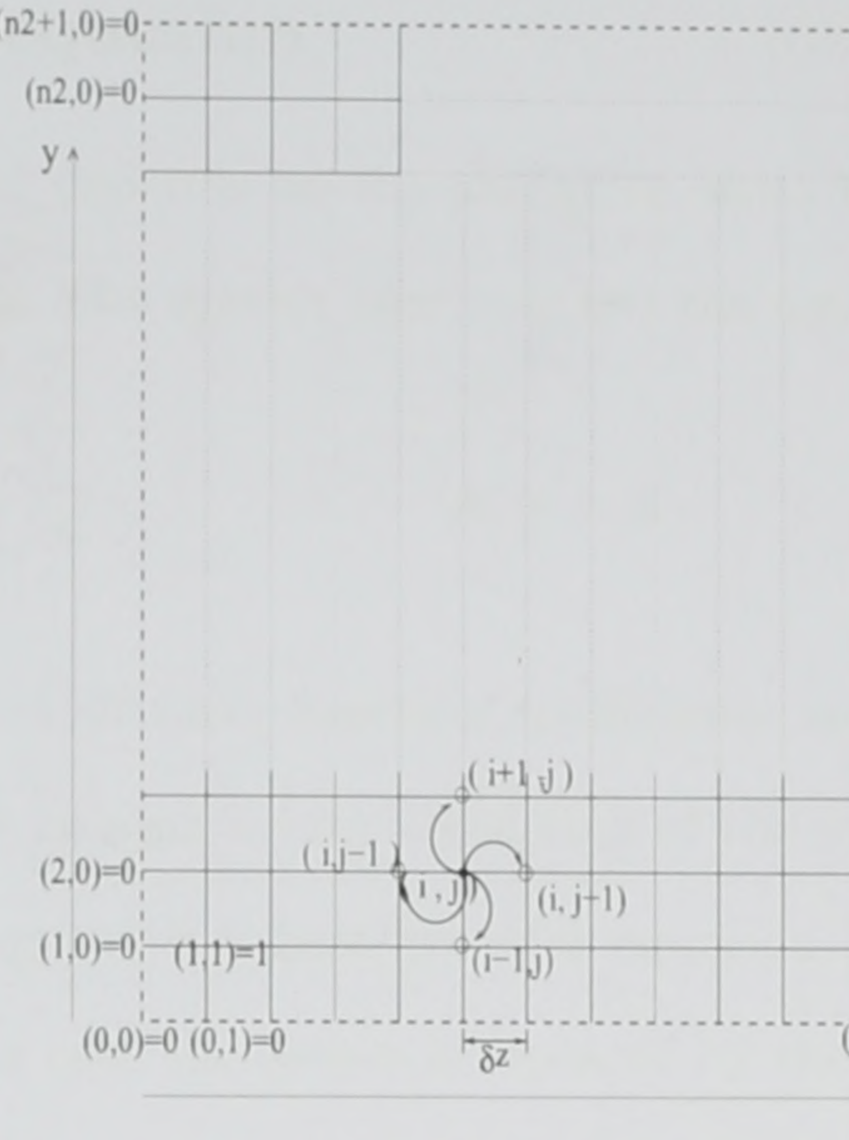

Figure 3.3: Schematic illustration of array representing cross section of wire and dependence of wave function points.

where,

$$k = \frac{-2m^*}{\hbar^2}\Big(E_{y,z} - V(y,z)\Big)(\delta y)^2 + 4 \tag{3.15}$$

Equation (3.14) shows that the value of the wave function at each point depends on the four surrounding grid points. Hence, the wave function can be calculated for any energy, by solving the sets of simultaneous equations generated by equation (3.14), provided that an appropriate initial condition is chosen. This initial condition has to be a non-zero value, otherwise the solution to this system of linear equations would be uniformly zero. Since scaling the wave function by a constant factor will not affect the energy eigenvalues, it is then reasonable to choose the following initial condition.

$$\psi_{1,1} = 1 \tag{3.16}$$

3.2.2 Matrix equation

The method developed depends on the ability to write the simultaneous equations, as a single matrix equation. The matrix equation has the form of

$$\mathbf{A}\cdot\Psi = \mathbf{S} \tag{3.17}$$

Where, $\mathbf{A}$ is the matrix of wave function coefficients and Ψ is a column vector of wave function points. $\mathbf{S}$ is a column vector consisting of the source terms. They are called the source terms in analogy with a heat transfer equation [67] which is solved in a similar manner. In the present case the source is replaced by the initial value. Now, to derive the form of these matrices, consider a small mesh of five by five elements, shown schematically in figure 3.4. The standard boundary conditions, given below by equations (3.18) and (3.19), are satisfied by all solutions.

$$\psi(y,z) \to 0 \ \text{ as } \ z \to \pm\infty \tag{3.18}$$

$$\psi(y,z) \to 0 \ \text{ as } \ y \to \pm\infty \tag{3.19}$$

This is accomplished by forcing all the outermost array elements to zero, shown by the dashed lines in figure 3.4. Thus, it is only necessary to calculate the internal points.

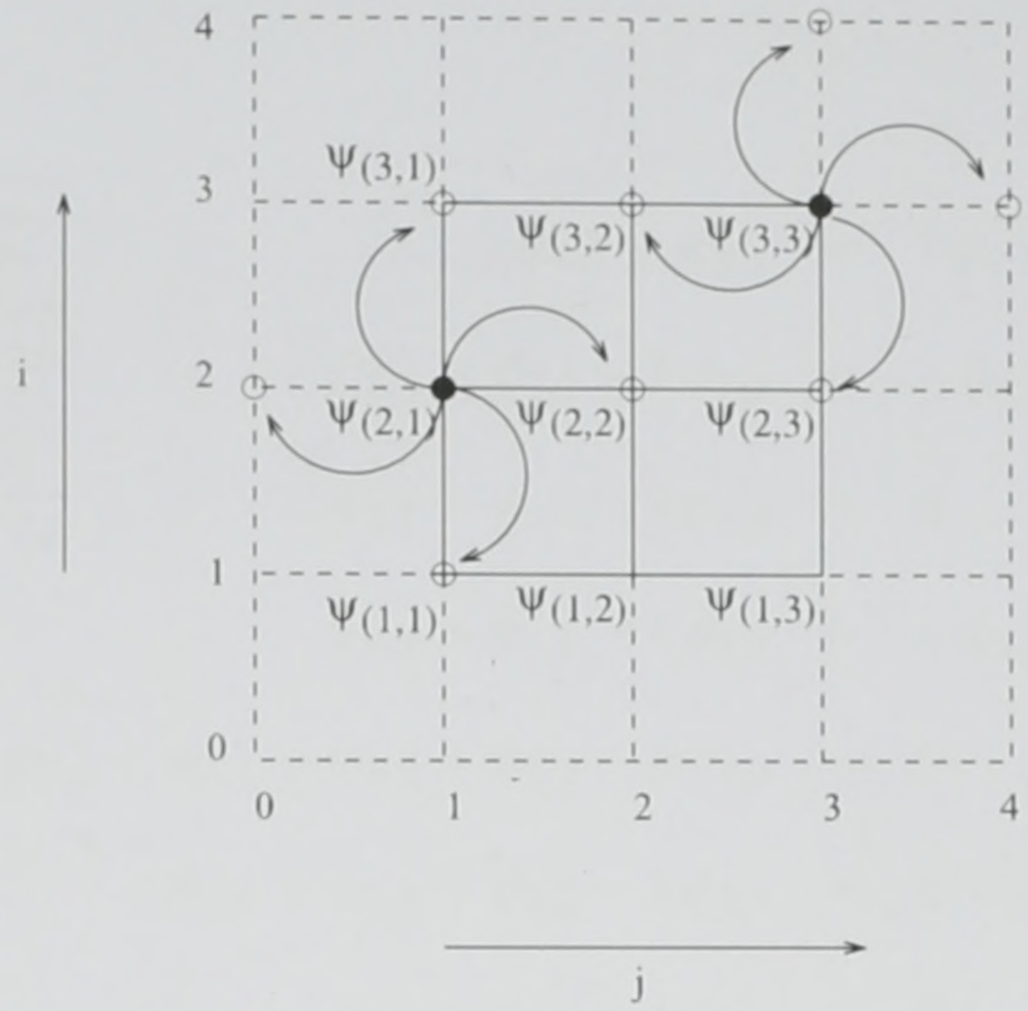

Figure 3.4: Schematic of five by five array with arrows showing dependence of points.

Now, writing out the entire set of equations explicitly yields,

$$i = 1, j = 1 \quad \psi_{1,2} + \psi_{1,0} + \psi_{2,1} + \psi_{0,1} - k\psi_{1,1} = 0 \tag{3.20}$$

$$i = 1, j = 2 \quad \psi_{1,3} + \psi_{1,1} + \psi_{2,2} + \psi_{0,2} - k\psi_{1,2} = 0 \tag{3.21}$$

$$i = 1, j = 3 \quad \psi_{1,4} + \psi_{1,2} + \psi_{2,3} + \psi_{0,3} - k\psi_{1,3} = 0 \tag{3.22}$$

$$i = 2, j = 1 \quad \psi_{2,2} + \psi_{2,0} + \psi_{3,1} + \psi_{1,1} - k\psi_{2,1} = 0 \tag{3.23}$$

$$i = 2, j = 2 \quad \psi_{2,3} + \psi_{2,1} + \psi_{3,2} + \psi_{1,2} - k\psi_{2,2} = 0 \tag{3.24}$$

$$i = 2, j = 3 \quad \psi_{2,4} + \psi_{2,2} + \psi_{3,3} + \psi_{1,3} - k\psi_{2,3} = 0 \tag{3.25}$$

$$i = 3, j = 1 \quad \psi_{3,2} + \psi_{3,0} + \psi_{4,1} + \psi_{2,1} - k\psi_{3,1} = 0 \tag{3.26}$$

$$i = 3, j = 2 \quad \psi_{3,3} + \psi_{3,1} + \psi_{4,2} + \psi_{2,2} - k\psi_{3,2} = 0 \tag{3.27}$$

$$i = 3, j = 3 \quad \psi_{3,4} + \psi_{3,2} + \psi_{4,3} + \psi_{2,3} - k\psi_{3,3} = 0 \tag{3.28}$$

From the boundary conditions of equations (3.17) and (3.18), all the points on the boundary of the array must equal zero, i.e. $\psi_{i,0}, \psi_{0,j}, \psi_{i,4}, \psi_{4,j} = 0$. Thus, equations (3.20) to

(3.28) will reduce to,

$$\psi_{1,2} + \psi_{2,1} = k\psi_{1,1} \tag{3.29}$$

$$\psi_{1,3} + \psi_{2,2} - k\psi_{1,2} = -\psi_{1,1} \tag{3.30}$$

$$\psi_{1,2} + \psi_{2,3} - k\psi_{1,3} = 0 \tag{3.31}$$

$$\psi_{2,2} + \psi_{3,1} - k\psi_{2,1} = -\psi_{1,1} \tag{3.32}$$

$$\psi_{2,3} + \psi_{2,1} + \psi_{3,2} + \psi_{1,2} - k\psi_{2,2} = 0 \tag{3.33}$$

$$\psi_{2,2} + \psi_{3,3} + \psi_{1,3} - k\psi_{2,3} = 0 \tag{3.34}$$

$$\psi_{3,2} + \psi_{2,1} - k\psi_{3,1} = 0 \tag{3.35}$$

$$\psi_{3,3} + \psi_{3,1} + \psi_{2,2} - k\psi_{3,2} = 0 \tag{3.36}$$

$$\psi_{3,2} + \psi_{2,3} - k\psi_{3,3} = 0 \tag{3.37}$$

It must be noted that even though there are nine internal array or wave function points, there are only eight unknowns since $\psi_{1,1}$ is defined by the initial condition of equation (3.16). Also, the variables $\psi_{i,j}$ are linearly dependent and as such equation (3.29) is providing redundant information, and since there are eight unknowns and nine equations then equation (3.29) will be excluded from the array. Now, the column vector Ψ, will have eight components, i.e. $n = [n_1 \times n_2] - 1$ components, which is actually the total number of unknown wave function points. Thus, the vector has the form,

$$\Psi = \begin{pmatrix} \psi_{1,2} \\ \psi_{1,3} \\ \psi_{2,1} \\ \vdots \\ \psi_{3,3} \end{pmatrix} \tag{3.38}$$

It can also be shown that the matrix of coefficients will be given by:

$$\mathbf{A} = \begin{pmatrix} -k & 1 & 0 & 1 & 0 & 0 & 0 & 0 \\ 1 & -k & 0 & 0 & 1 & 0 & 0 & 0 \\ 0 & 0 & -k & 1 & 0 & 1 & 0 & 0 \\ 1 & 0 & 1 & -k & 1 & 0 & 1 & 0 \\ 0 & 1 & 0 & 1 & -k & 0 & 0 & 1 \\ 0 & 0 & 1 & 0 & 0 & -k & 1 & 0 \\ 0 & 0 & 0 & 1 & 0 & 1 & -k & 1 \\ 0 & 0 & 0 & 0 & 1 & 0 & 1 & -k \end{pmatrix} \tag{3.39}$$

This matrix can be rewritten as:

$$\mathbf{A} = \begin{pmatrix} \beta_1 & I_1 & \mathbf{0} \\ I_2 & \beta & I \\ \mathbf{0} & I & \beta \end{pmatrix} \tag{3.40}$$

where,

$$\beta_1 = \begin{pmatrix} -k & 1 \\ 1 & -k \end{pmatrix} \quad I_1 = \begin{pmatrix} 0 & 1 & 0 \\ 0 & 0 & 1 \end{pmatrix} \quad \mathbf{0} = \begin{pmatrix} 0 & 0 & 0 \\ 0 & 0 & 0 \end{pmatrix} \quad I_2 = \begin{pmatrix} 0 & 0 \\ 1 & 0 \\ 0 & 1 \end{pmatrix} \tag{3.41}$$

$$\beta = \begin{pmatrix} -k & 1 & 0 \\ 1 & -k & 1 \\ 0 & 1 & -k \end{pmatrix} \quad I = \begin{pmatrix} 1 & 0 & 0 \\ 0 & 1 & 0 \\ 0 & 0 & 1 \end{pmatrix} \quad \mathbf{0} = \begin{pmatrix} 0 & 0 \\ 0 & 0 \\ 0 & 0 \end{pmatrix} \tag{3.42}$$

The column vector of source terms is given by,

$$\mathbf{S} = \begin{pmatrix} -\psi_1 \\ 0 \\ -\psi_1 \\ 0 \\ \vdots \\ 0 \end{pmatrix} \tag{3.43}$$

Now, all that needs to be done is solve this system of equations to obtain the value of Ψ, for which there are a variety of algorithms available. The value of $\psi_{1,1}$ can now be simply included as the first element of the vector Ψ.

This method can be generalised to any array size. Thus, if the quantum wire is divided into $n_1 + 2$ columns and $n_2 + 2$ rows, and a suitable scale, δy, is chosen to account for any size wire, the method still holds. The column vector Ψ will consist of $n = [n_1 \times n_2] - 1$ elements, which is the total number of unknown wave function points and is given by equation (3.44). It consists of a total of n_2 blocks each of length n_1 elements, with the exception of the first block which consists of $n_1 - 1$ elements since $\psi_{1,1}$ is already determined.

$$\Psi = \begin{pmatrix} \psi_{1,2} \\ \psi_{1,3} \\ \vdots \\ \psi_{1,n_1} \\ \psi_{2,1} \\ \vdots \\ \psi_{n_2,n_1} \end{pmatrix} \tag{3.44}$$

The matrix $\mathbf{A}$ will be a $(n \times n)$ sparse matrix, i.e. most of the elements are zeroes. The best way to represent this matrix, is by using sub-matrices as before. Here, there are

n_2 blocks or sub-matrices, which can be written as follows,

$$\mathbf{A} = \overbrace{\begin{pmatrix} \beta_1 & I_1 & \mathbf{0} & \cdots & \cdots & \mathbf{0} \\ I_2 & \beta & I & \mathbf{0} & \cdots & \mathbf{0} \\ \mathbf{0} & I & \beta & I & \ddots & \vdots \\ \vdots & \ddots & \ddots & \ddots & \ddots & \mathbf{0} \\ \mathbf{0} & \cdots & \mathbf{0} & I & \beta & I \\ \mathbf{0} & \cdots & \cdots & \mathbf{0} & I & \beta \end{pmatrix}}^{n_2 \text{blocks}} \tag{3.45}$$

where, the sub-matrix β_1 is a $([n_1 - 1] \times [n_1 - 1])$ tridiagonal matrix of the form,

$$\beta_1 = \begin{pmatrix} -k & 1 & 0 & \cdots & 0 \\ 1 & -k & 1 & \ddots & \vdots \\ 0 & \ddots & \ddots & \ddots & 0 \\ \vdots & \ddots & 1 & -k & 1 \\ 0 & \cdots & 0 & 1 & -k \end{pmatrix} \tag{3.46}$$

The remaining β sub-matrices all have the form of equation (3.46), but are all $(n_1 \times n_1)$ matrices. The sub-matrix I_1 is a $([n_1 - 1] \times n_1)$ matrix of the form,

$$I_1 = \begin{pmatrix} 0 & 1 & 0 & \cdots & 0 \\ 0 & 0 & 1 & \ddots & \vdots \\ \vdots & \ddots & \ddots & \ddots & 0 \\ 0 & \cdots & 0 & 0 & 1 \end{pmatrix} \tag{3.47}$$

The sub-matrix I_2 is a $(n_1 \times [n_1 - 1])$ matrix of the form,

$$I_2 = \begin{pmatrix} 0 & \cdots & \cdots & 0 \\ 1 & 0 & \cdots & \vdots \\ 0 & \ddots & \ddots & \vdots \\ \vdots & \ddots & \ddots & 0 \\ 0 & \cdots & 0 & 1 \end{pmatrix} \tag{3.48}$$

All the sub-matrices I are $(n_1 \times n_1)$ identity matrices. The remainder of the matrix $\mathbf{A}$ is comprised of zeroes.

Finally, the matrix $\mathbf{S}$ is a column vector of n elements and is of the form:

$$\mathbf{S} = \begin{pmatrix} -\psi_{1,1} \\ 0 \\ \vdots \\ 0 \\ -\psi_{1,1} \\ 0 \\ \vdots \\ 0 \end{pmatrix} \begin{matrix} \left.\begin{matrix} \\ \\ \\ \end{matrix}\right\} n_1 - 2 \\ \text{zeroes} \\ \\ \\ \\ \\ \end{matrix} \tag{3.49}$$

Having established the general forms of the matrices involved, there are several software packages available which can be used to solve this system of equations. In this case the package MATLAB® was used, because of its ability to deal with sparse matrices with little memory overhead. A computer program was written to set up the matrices and to find the solution to the set of linear equations, remembering to add $\psi_{1,1}$ as the first element of the vector Ψ.

3.2.3 Correct physical solutions

The only issue that remains to be addressed, is the identification of the correct physical solutions, since in spite of the fact that a mathematical solution can be calculated for all energies, correct physical solutions only occur at certain eigenenergies. In the one-dimensional shooting method [27] the correct physical solutions are identified by finding the solutions, that occur for energies E, which satisfy the standard boundary conditions of equations (3.18) and (3.19). In the case of this matrix method it is not possible to use the boundary conditions to identify the eigenenergies, since all solutions are forced to satisfy the boundary conditions.

A new aspect introduced in this work is to base the search for the correct physical solutions on the energies where the wave function has well defined maxima away from the edges of the $y-z$ plane. The exact location of these maxima depends on the character of the eigenstate, e.g. for the ground state the maxima should be at the centre of the plane (for a symmetric potential). The initial condition, stated in equation (3.16), of setting one of the corner values to unity, ensured that away from a physical solution, the maxima across the plane was always at this point. Only when the scanned energy was close to a solution did a global maxima occur away from this point. The correct energies were identified by plotting the position of the maxima in the $y-z$ plane versus the energy. The resulting plot not only gives a good estimate for the value of the eigenenergy but also gives a good indication of the character of the eigenstate, i.e. ground state, first excited state etc. figure 3.5 shows a plot of position of the maxima along the $y-$axis of the QWW versus energy for an infinitely deep 600×600 Å QWW. The well defined delta-like spikes indicate the energy level of the different states.

Figures 3.6 and 3.7 show the wave functions at the energies of the first two spikes. Table 3.1 shows the eigenenergies, obtained using this method, of the first four states compared to the eigenenergies, of the same eigenstates, which were calculated analytically [27]. The mesh used for these calculations was a 100×100 mesh, i.e. a mesh separation of 6 Å. As can be seen, the calculated eigenenergies lie within 0.25 meV of the analytical values.

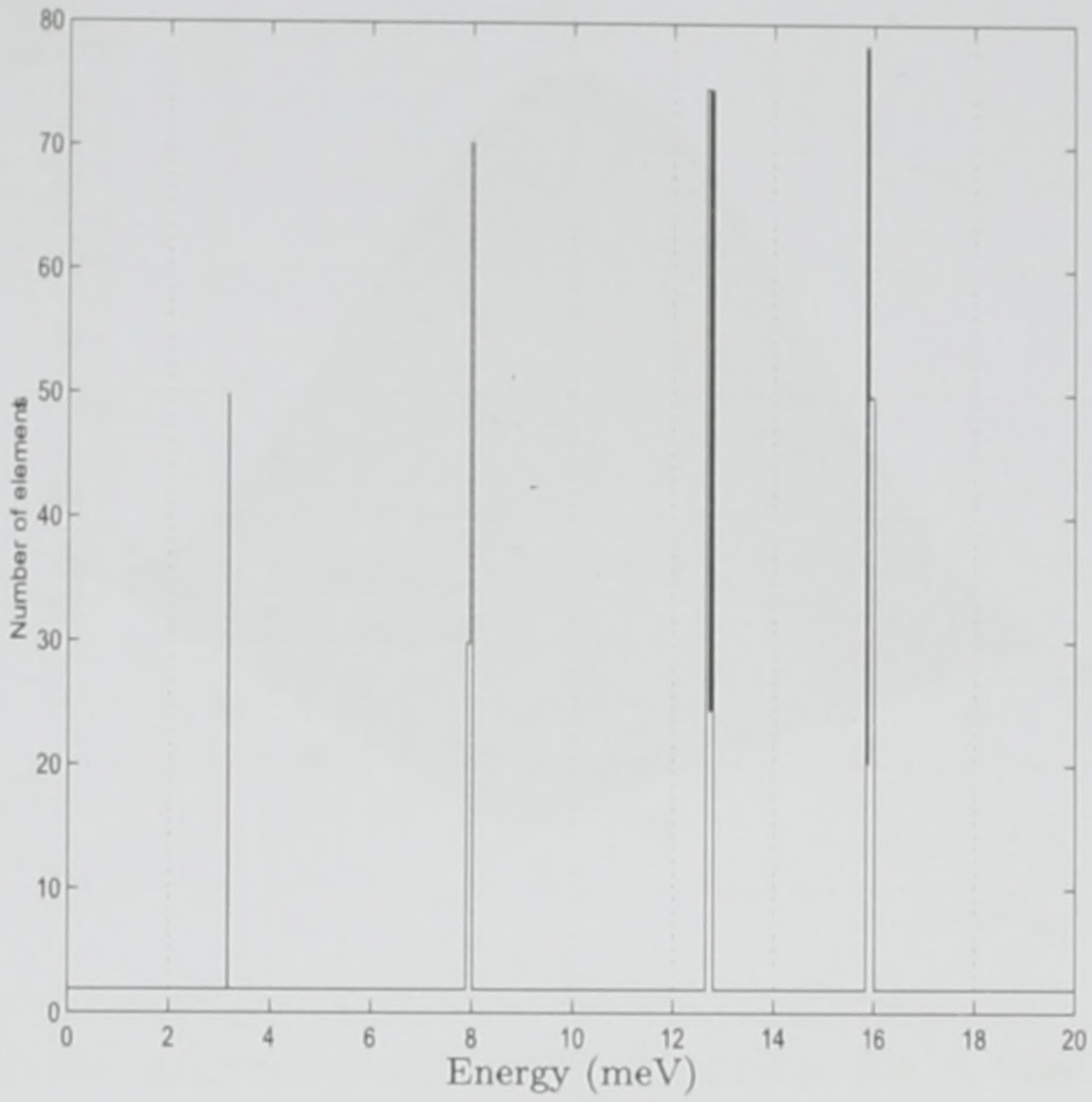

Figure 3.5: Position of maxima along the $y-$axis vs. Energy for a 600×600 Å wire with zero potential.

Table 3.1: Comparison of results between analytical and numerical values for a 600×600 Å infinite QWW

State	Numerical values (meV)	Analytical values (meV)
Ground	3.18	3.12
First	7.95	7.95
Second	12.65	12.47
Third	15.83	15.59

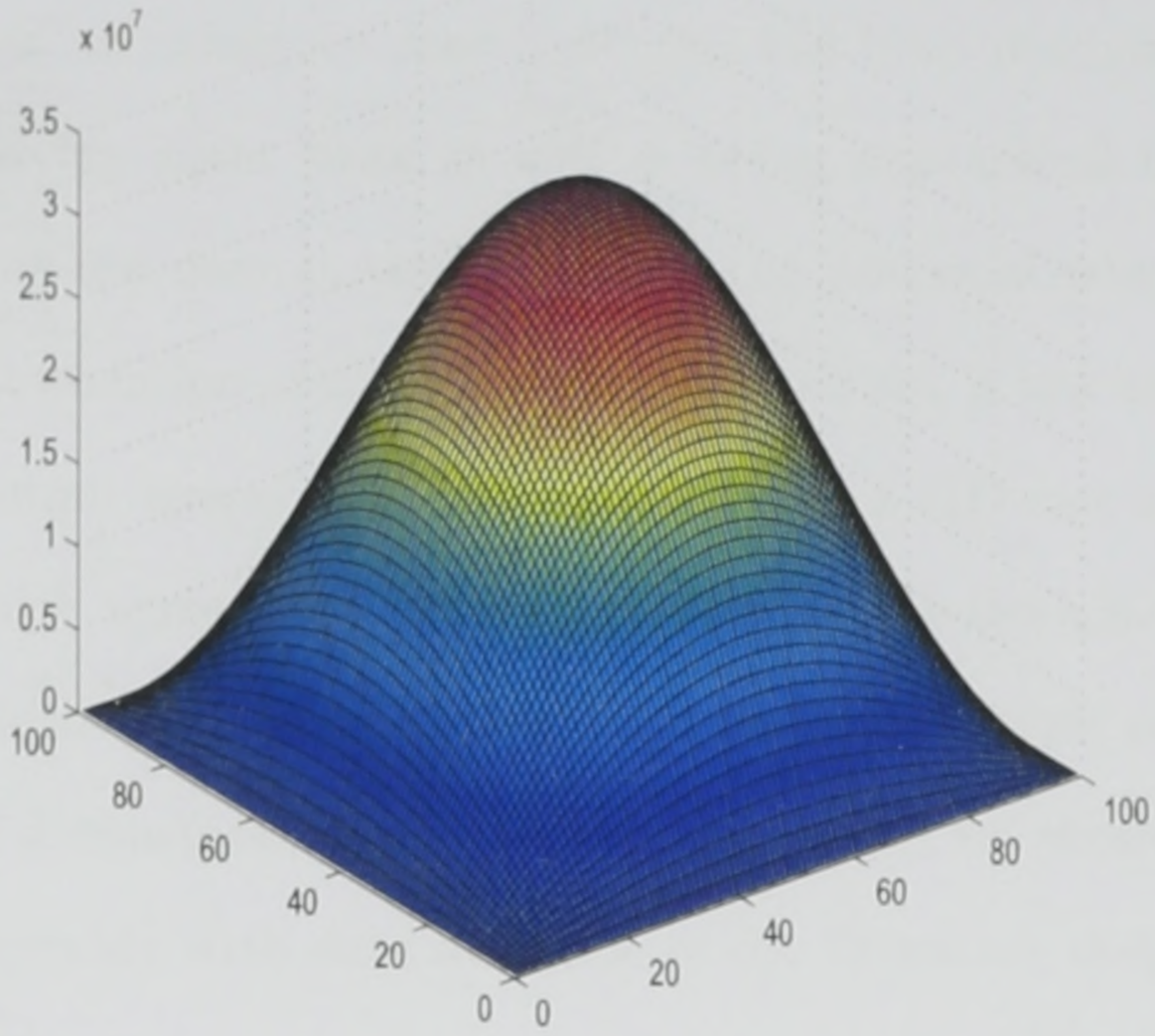

Figure 3.6: Normalised ground state wave function for a 600×600 Å wire with zero potential, horizontal coordinates represent position on the cross section of the QWW. Energy = 3.18 meV.

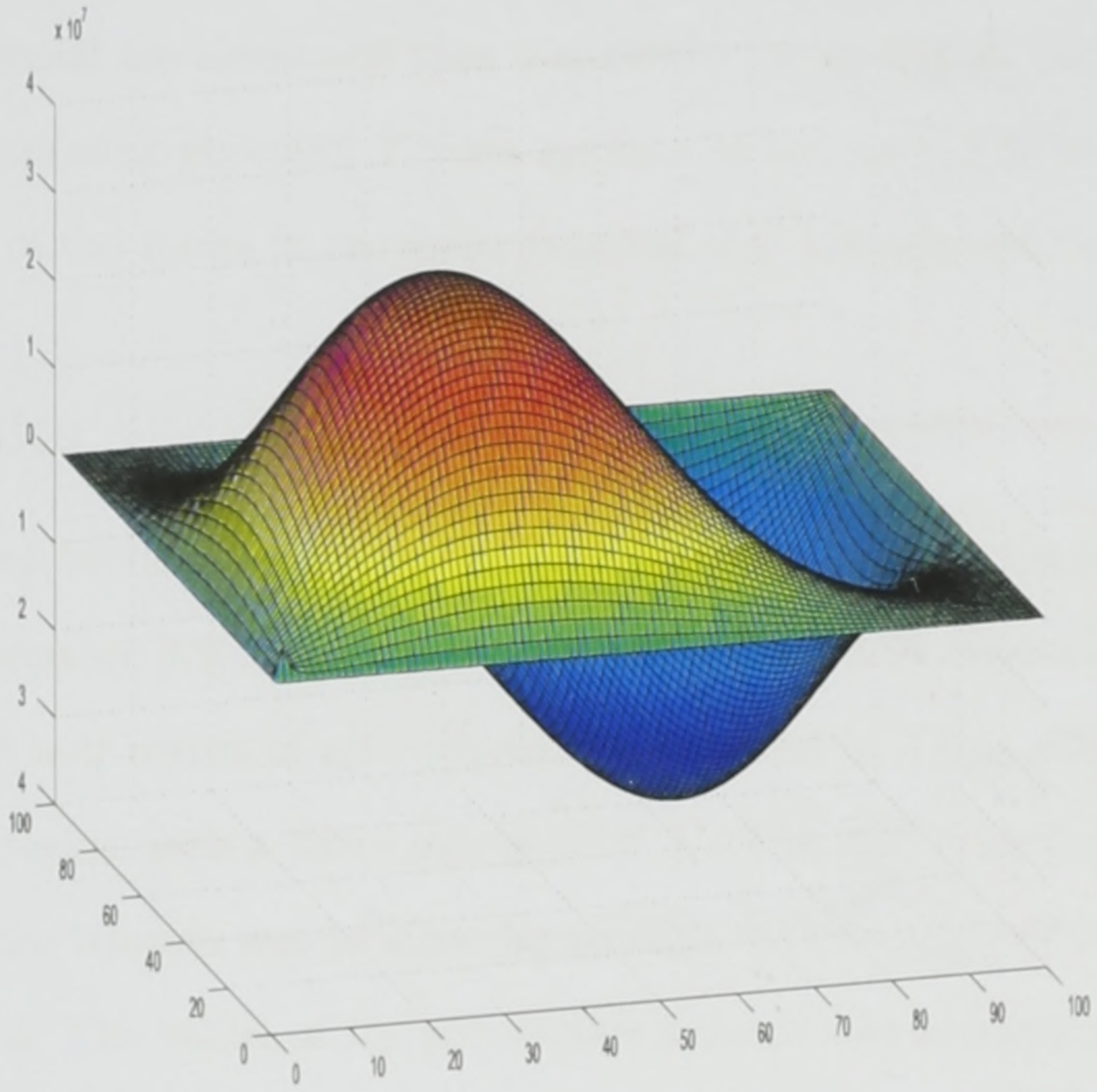

Figure 3.7: Normalised wave function of the first excited state for a 600×600 Å wire with zero potential, horizontal coordinates represent position on the cross section of the QWW. Energy = 7.95 meV.

3.3 Triangular quantum wire

So far only the case of an infinitely deep potential has been discussed, which as stated before was only a starting point since as well as being impractical it is also unrealistic. While most researchers use complicated forms for the potential which account for band mixing and the spatial variation of the potential due to strain, it has been demonstrated [2] that the use of a constant average potential throughout a QD can be valid, resulting in electronic energies which agree very well with theoretical studies which take into account the above mentioned features. Following this path, all the potentials used in the remainder of this research have a constant average value and as will be shown the results of the calculation agree favourably with data available in the literature despite the simple form of the potentials.

These finite potentials are included into the method as separate functions called from within the main program. They operate in the following way: the shape and spatial position of the potential is defined on a dummy matrix, the indices defining the shape and extent of the potential are noted and then mapped to the matrix **A**. Referring to sections 3.2.2, since the confining potential V only appears in the term k it is only necessary to update the value of the terms in the main diagonal that are affected.

3.3.1 Results

The first system to be examined was a finite barrier triangular quantum wire which was taken from the literature [62] for ease of comparison. The QWW used comprised of a GaAs triangular shaped well region of zero potential embedded in a $Ga_{0.6}Al_{0.4}As$ square cross sectional barrier region with a finite potential of V. The dimensions of the barrier were 600×600 Å and the triangle was an isosceles triangle with an angle of $70.6°$ subtended by the two equal sides. The values of the parameters were chosen to correspond with those in the literature [62]. The values used were: $m^* = 0.0665m_0$, and $V = 276$ meV, see figure 3.8.

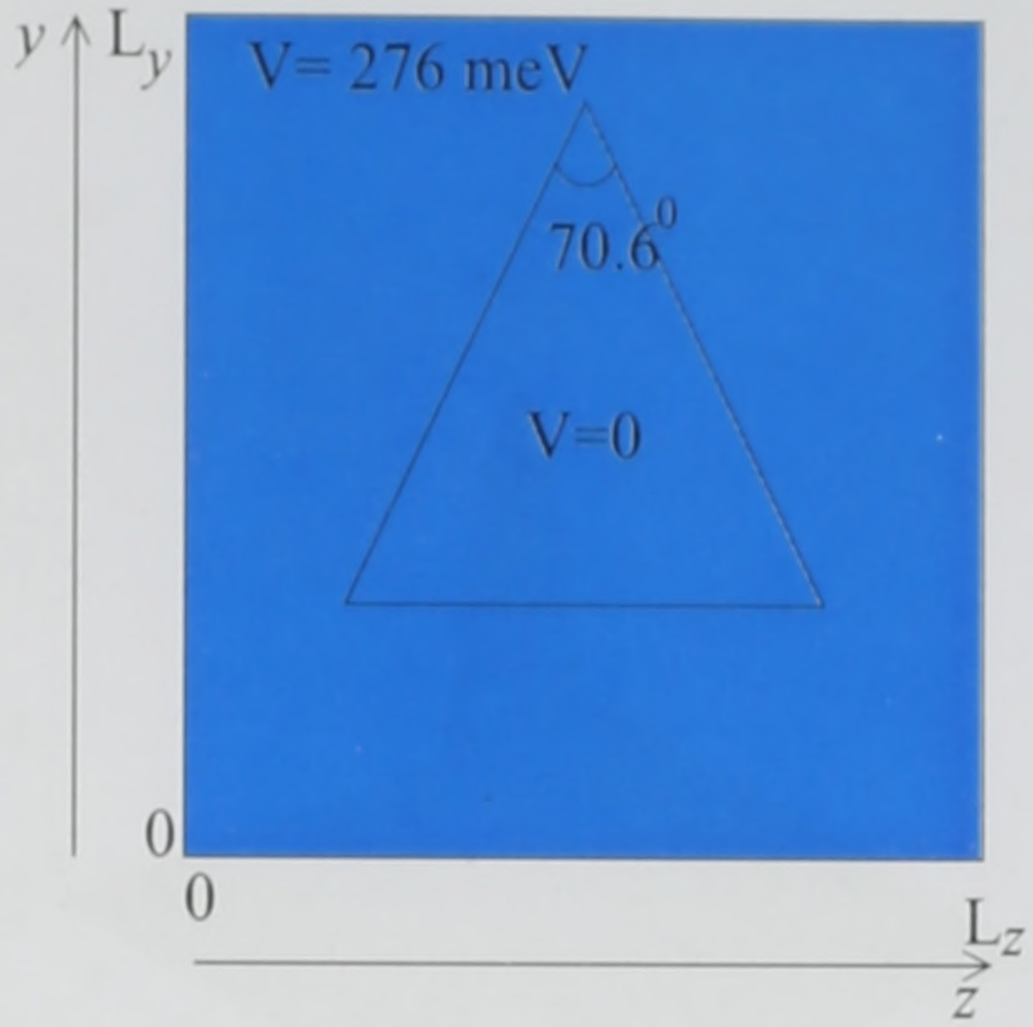

Figure 3.8: Figure showing rectangular cross sectional wire with finite barrier height with triangular region having no potential.

Different values for the base width and height of the triangle were used in the calculation of the energy states. The mesh spacing used was 6 Å giving an array size of 100×100 elements. Figure 3.9 shows the wave function for a base width of 200 Å and a height of 141.2 Å. It can clearly be seen that the peak of the wave function is localised over a small central region of the cross section (corresponding to the triangular region), when compared to the wave function for the infinitely deep wire of figure 3.6. Since the wave functions are directly related to the probability of the electron existing in any given region of space, this behaviour may be interpreted in the following manner: in the case of the infinitely deep wire an electron has a maximum probability of being located at the centre of the QWW and this probability diminishes gradually when moving towards the edge of the QWW where it drops to a negligible value. In contrast, the wave function for the case of the triangular QWW shows that an electron has a maximum probability of being located at the centre of the triangular region, and this probability diminishes rapidly when moving towards the edge of the triangular region and drops to a negligible value just outside this region.

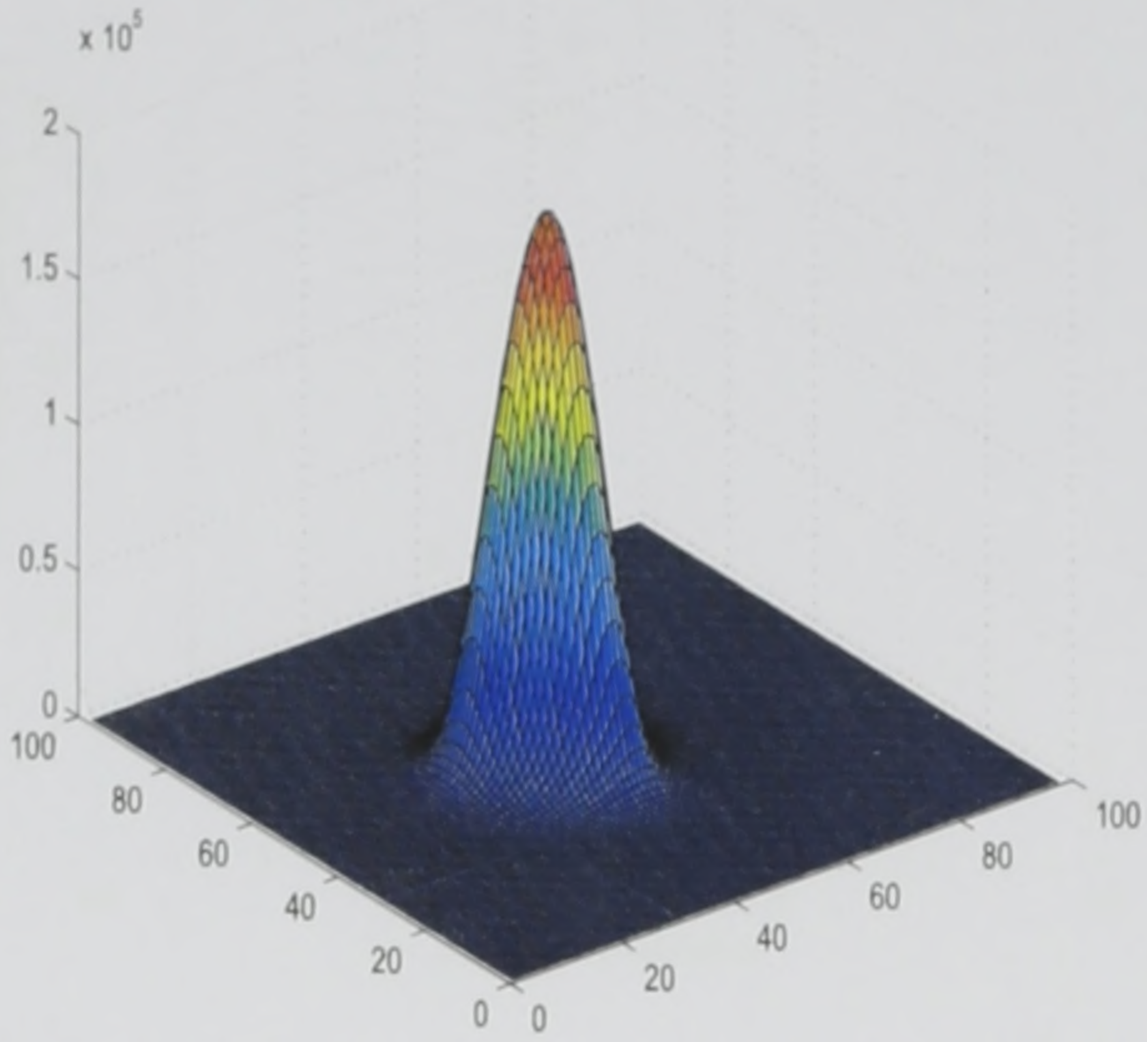

Figure 3.9: Normalised wave function of the ground state for a triangular cross sectional wire, horizontal coordinates represent position on the cross section of the QWW. Energy= 60.76 meV.

Figure 3.10 shows the results obtained using this method along with the data found in the literature.

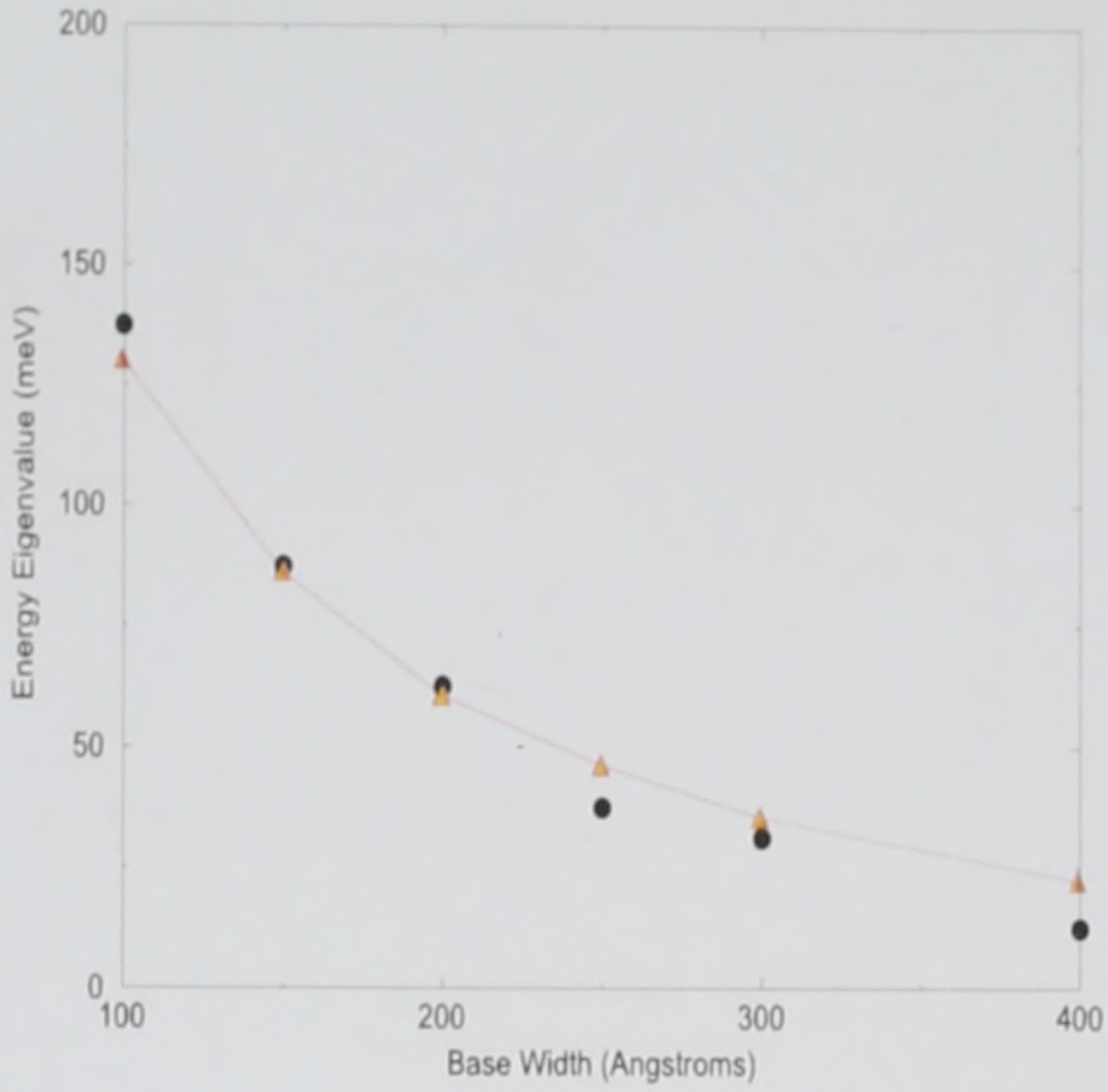

Figure 3.10: Energy eigenenergies of triangular wire with finite barrier potential. Dots data from Gangopahdhyay [62], line with triangle data obtained using the finite difference method presented here.

The results obtained from this method show very good agreement with that of Gangopahdhyay [62], with the difference in eigenenergies ranging between 1 and 10 meV[1]. The accuracy of these eigenenergies can be improved by increasing the resolution of the mesh, but this in turn means increasing the computation time. Since for most cases calculating the eigenenergy to within a few meV is sufficient, it was deemed unnecessary to use a smaller grid step.

Figure 3.11 shows the ground state energy versus mesh size in each direction for a triangular wire of base width of 200 Å. It can be seen that the energy starts to converge at a mesh size of 90. Note that even though the energy increases slightly from that point when going to larger mesh sizes, it does not change by a significant amount that would justify the use of a larger mesh size because of the increase in computation time.

[1]This is likely to arise from the simplified constant effective mass Hamiltonian employed here for this initial demonstration

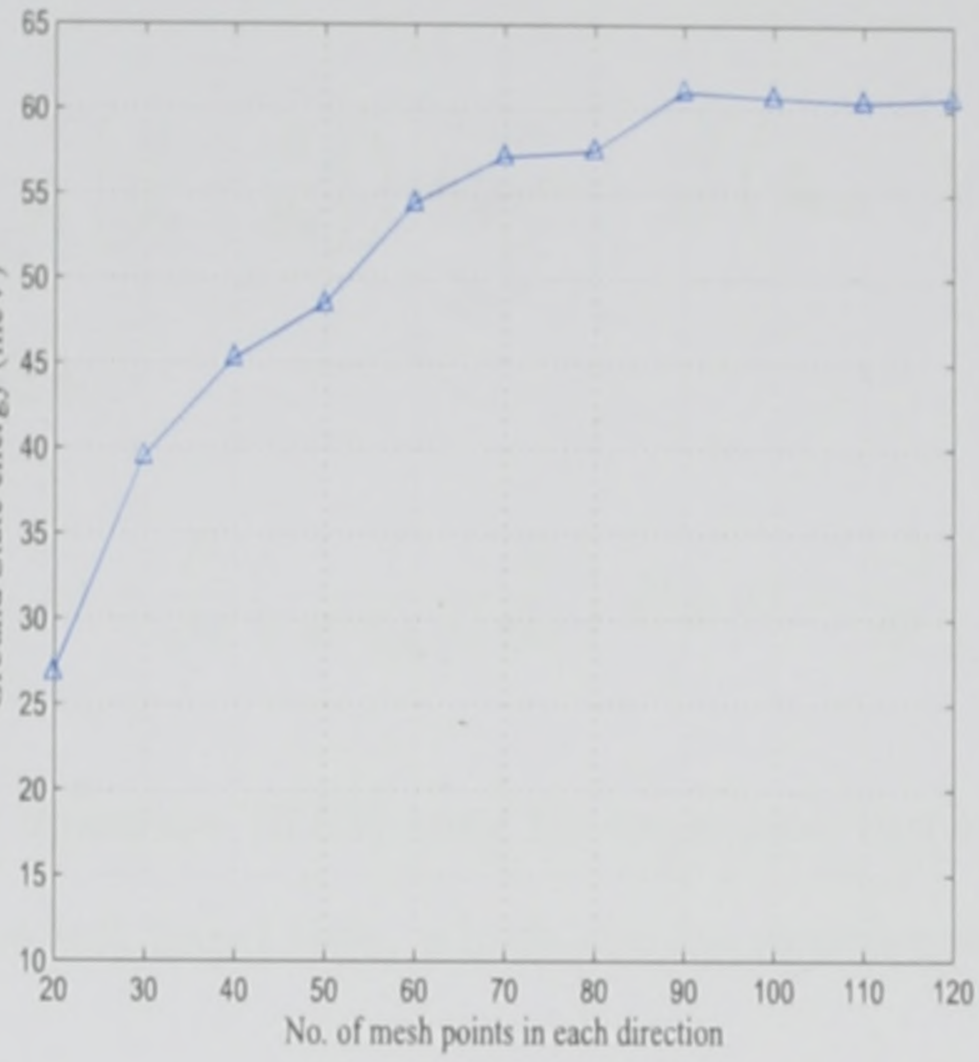

Figure 3.11: Ground state energy vs. Mesh size for triangular QWW with a base width of 200 Å.

3.4 Extension to variable effective mass

So far, only the case of constant effective mass has been considered. However, the Schrödinger equation for systems of real interest must take account of variable effective masses between different semiconductor layers. This section provides a mathematical overview of how the method can be modified to account for variable effective masses.

With the aim of extending the finite difference method to account for this more realistic situation, consider the two dimensional variable effective mass Schrödinger equation given by,

$$\frac{-\hbar^2}{2}\nabla\left(\frac{1}{m^*(y,z)}\nabla\right)\psi(y,z)+V(y,z)\psi(y,z)=E_{y,z}\psi(y,z) \tag{3.50}$$

Equation (3.50) can be rewritten as,

$$\nabla\left(\frac{1}{m^*(y,z)}\nabla\right)\psi(y,z)=\frac{-2}{\hbar^2}\Big(E_{y,z}-V(y,z)\Big)\psi(y,z) \tag{3.51}$$

Equation (3.51) can be further expanded to give,

$$\left[\frac{\partial}{\partial y}+\frac{\partial}{\partial z}\right]\left(\frac{1}{m^*(y,z)}\left[\frac{\partial}{\partial y}+\frac{\partial}{\partial z}\right]\right)\psi(y,z)=\frac{-2}{\hbar^2}\Big(E_{y,z}-V(y,z)\Big)\psi(y,z) \tag{3.52}$$

and this can be expanded to,

$$\frac{\partial}{\partial y}\left(\frac{1}{m^*(y,z)}\frac{\partial}{\partial y}\right)\psi(y,z)+\frac{\partial}{\partial z}\left(\frac{1}{m^*(y,z)}\frac{\partial}{\partial z}\right)\psi(y,z)=\frac{-2}{\hbar^2}\Big(E_{y,z}-V(y,z)\Big)\psi(y,z) \tag{3.53}$$

The expression given by equation (3.53) may be expanded further. For example consider only the first term on the left hand side, which can be expressed as,

$$-\frac{1}{[m^*(y,z)]^2}\left(\frac{\partial}{\partial y}m^*\right)\frac{\partial}{\partial y}\psi(y,z)+\frac{1}{m^*}\frac{\partial^2}{\partial y^2}$$

However, it was shown that numerical inaccuracies occur when the one dimensional form of this expression was expanded in terms of finite differences [27], thus the expression given in (3.53) is expanded in terms of finite differences directly, to give

$$\frac{\frac{1}{m^*(y+\delta y,z)}\left.\frac{\partial\psi(y,z)}{\partial y}\right|_{y+\delta y,z}-\frac{1}{m^*(y-\delta y,z)}\left.\frac{\partial\psi(y,z)}{\partial y}\right|_{y-\delta y,z}}{2\delta y}+$$

$$\frac{\frac{1}{m^*(y,z+\delta z)}\left.\frac{\partial\psi(y,z)}{\partial z}\right|_{y,z+\delta z}-\frac{1}{m^*(y,z-\delta z)}\left.\frac{\partial\psi(y,z)}{\partial z}\right|_{y,z-\delta z}}{2\delta z}$$

$$=\frac{-2}{\hbar^2}\Big(E_{y,z}-V(y,z)\Big)\psi(y,z) \tag{3.54}$$

Setting $\delta z = \delta y$ in the interests of simplicity, while ensuring that the step lengths are small enough so that the approximation is valid, yields

$$\frac{1}{m^*(y+\delta y,z)}\left.\frac{\partial\psi(y,z)}{\partial y}\right|_{y+\delta y,z} - \frac{1}{m^*(y-\delta y,z)}\left.\frac{\partial\psi(y,z)}{\partial y}\right|_{y-\delta y,z} + \frac{1}{m^*(y,z+\delta z)}\left.\frac{\partial\psi(y,z)}{\partial z}\right|_{y,z+\delta z} - \frac{1}{m^*(y,z-\delta z)}\left.\frac{\partial\psi(y,z)}{\partial z}\right|_{y,z-\delta z} = \frac{-2(2\delta y)}{\hbar^2}\Big(E_{y,z} - V(y,z)\Big)\psi(y,z) \quad (3.55)$$

From (3.4) the centred finite difference expansion for the first partial derivative of a function $f(y,z)$ is given by,

$$\left.\frac{\partial f}{\partial y}\right|_{y,z} = \frac{f(y+\delta y,z) - f(y-\delta y,z)}{2\delta y} \quad (3.56)$$

Utilising equation (3.56), making the transformation $2\delta y \to \delta y$ and rearranging, equation (3.55) becomes,

$$\frac{\psi(y+\delta y,z)}{m^*(y+\delta y/2,z)} + \frac{\psi(y-\delta y,z)}{m^*(y-\delta y/2,z)} + \frac{\psi(y,z+\delta z)}{m^*(y,z+\delta z/2)} - \frac{\psi(y,z-\delta z)}{m^*(y,z-\delta z/2)} - \left[\frac{-2(\delta y)^2}{\hbar^2}\Big(E_{y,z} - V(y,z)\Big) + \frac{1}{m^*(y+\delta y/2,z)} + \frac{1}{m^*(y-\delta y/2,z)} + \frac{1}{m^*(y,z+\delta z/2)} + \frac{1}{m^*(y,z-\delta z/2)}\right]\psi(y,z) = 0 \quad (3.57)$$

This form of the expansion is more robust since the effective mass m^* at the intermediate points, for example at $(y+\delta y/2,z)$, can be calculated by taking the mean of the two neighbouring points, at (y,z) and $(y+\delta y,z)$. In this manner the inaccuracies that result from large discontinuities in the effective mass between layers may be avoided, in analogy with the one dimensional case [27].

In array notation, equation (3.57) can be expressed as,

$$\frac{\psi_{i+1,j}}{m^*_{i+\frac{1}{2},j}} + \frac{\psi_{i-1,j}}{m^*_{i-\frac{1}{2},j}} + \frac{\psi_{i,j+1}}{m^*_{i,j+\frac{1}{2}}} + \frac{\psi_{i,j-1}}{m^*_{i,j-\frac{1}{2}}} - k_{i,j}\psi_{i,j} = 0 \quad (3.58)$$

where,

$$k_{i,j} = \left[\frac{-2(\delta y)^2}{\hbar^2} \Big(E_{i,j} - V(i,j) \Big) + \frac{1}{m^*_{i+\frac{1}{2},j}} + \frac{1}{m^*_{i-\frac{1}{2},j}} + \frac{1}{m^*_{i,j+\frac{1}{2}}} + \frac{1}{m^*_{i,j-\frac{1}{2}}} \right] \psi_{i,j} \quad (3.59)$$

and the indices i, j label the y, z directions.

This equation can be formulated into a matrix equation identical in form to equation (3.17) and is given by

$$\mathbf{A_m} \cdot \Psi = \mathbf{S_m} \quad (3.60)$$

where, $\mathbf{A_m}$ is the matrix of wave function coefficients, Ψ is the column vector of wave function points and $\mathbf{S_m}$ is the column vector of source terms. The vector Ψ is identical to that described by equation (3.44), where n_1 and n_2 are the mesh dimensions representing the computational domain, see section 3.2.2. The exact form of the remaining matrices depends on the specific system being investigated, i.e. it depends on the shape of the potential and geometry of the particular system. However, it can be shown that $\mathbf{A_m}$ is a $(n \times n)$ matrix, where $n = [n_1 \times n_2] - 1$, and has the general form

$$\mathbf{A_m} = \overbrace{\begin{pmatrix} \alpha_1 & L_1 & \mathbf{0} & \cdots & \cdots & \mathbf{0} \\ L_2 & \alpha & L & \mathbf{0} & \cdots & \mathbf{0} \\ \mathbf{0} & L & \alpha & L & \ddots & \vdots \\ \vdots & \ddots & \ddots & \ddots & \ddots & \mathbf{0} \\ \mathbf{0} & \cdots & \mathbf{0} & L & \alpha & L \\ \mathbf{0} & \cdots & \cdots & \mathbf{0} & L & \alpha \end{pmatrix}}^{n_2 \text{blocks}} \quad (3.61)$$

where the sub-matrix α_1 is a $([n_1 - 1] \times [n_1 - 1])$ tridiagonal matrix of the form,

$$\alpha_1 = \begin{pmatrix} -k_{i,j} & {}^{1}/_{m_{i,j}} & 0 & \cdots & 0 \\ {}^{1}/_{m_{i,j}} & -k_{i,j} & {}^{1}/_{m_{i,j}} & \ddots & \vdots \\ 0 & \ddots & \ddots & \ddots & 0 \\ \vdots & \ddots & {}^{1}/_{m_{i,j}} & -k_{i,j} & {}^{1}/_{m_{i,j}} \\ 0 & \cdots & 0 & {}^{1}/_{m_{i,j}} & -k_{i,j} \end{pmatrix} \tag{3.62}$$

The remaining α sub-matrices all have the form of (3.62), but are all $(n_1 \times n_1)$ matrices.

The sub-matrix L_1 is a $([n_1 - 1] \times n_1)$ matrix of the form,

$$L_1 = \begin{pmatrix} 0 & 1 & 0 & \cdots & 0 \\ 0 & 0 & {}^{1}/_{m_{i,j}} & \ddots & \vdots \\ \vdots & \ddots & \ddots & \ddots & 0 \\ 0 & \cdots & 0 & 0 & {}^{1}/_{m_{i,j}} \end{pmatrix} \tag{3.63}$$

The sub-matrix L_2 is a $(n_1 \times [n_1 - 1])$ matrix of the form,

$$L_2 = \begin{pmatrix} 0 & \cdots & \cdots & 0 \\ {}^{1}/_{m_{i,j}} & 0 & \cdots & \vdots \\ 0 & \ddots & \ddots & \vdots \\ \vdots & \ddots & \ddots & 0 \\ 0 & \cdots & 0 & {}^{1}/_{m_{i,j}} \end{pmatrix} \tag{3.64}$$

All the sub-matrices L are $(n_1 \times n_1)$ square matrices of the form,

$$L = \begin{pmatrix} {}^{1}/_{m_{i,j}} & 0 & \cdots & 0 \\ 0 & \ddots & \ddots & \vdots \\ \vdots & \ddots & \ddots & \vdots \\ 0 & \cdots & 0 & {}^{1}/_{m_{i,j}} \end{pmatrix} \tag{3.65}$$

The remainder of the matrix $\mathbf{A_m}$ is comprised of zeroes. Finally, the matrix $\mathbf{S_m}$ is a column vector of n elements and is of the form,

$$\mathbf{S_m} = \begin{pmatrix} -\psi_{1,1}/m_{1,1.5} \\ 0 \\ \vdots \\ 0 \\ -\psi_{1,1}/m_{1.5,1} \\ 0 \\ \vdots \\ 0 \end{pmatrix} \begin{matrix} \left.\begin{matrix} \\ \\ \\ \\ \end{matrix}\right\} n_1 - 2 \text{ zeroes} \\ \\ \\ \\ \\ \\ \\ \\ \end{matrix} \tag{3.66}$$

In order to construct the matrix $\mathbf{A_m}$ for a specific system, the following procedure is carried out; first the matrix is created by setting all the terms $1/m_{i,j}$ to the value of the barrier effective mass m_b^*. The sub-routine that constructs the potential is modified, so as to return the indices of the QWW region. A mapping scheme is used to identify the elements in $\mathbf{A_m}$ that correspond to this region, and all the elements corresponding to the internal points are modified to the wire effective mass, $1/m_w^*$, and the corresponding $k_{i,j}$ element is also adjusted accordingly. The matrix elements corresponding to the border points are modified to the average between the two masses, $m_{av} = \frac{m_b^* + m_w^*}{2}$, as are the corresponding $k_{i,j}$ elements. As for the source vector $\mathbf{S_m}$, the terms $-\frac{\psi_{1,1}}{m_{1,1.5}}$ and $-\frac{\psi_{1,1}}{m_{1.5,1}}$ always correspond to the effective mass of the barrier region, since the initial value is at the corner of the computational domain and hence far away from the wire region.

3.5 Conclusion

In this chapter a numerical finite difference method was developed and used to calculate the electronic eigenenergies of an infinitely deep quantum wire, by solving the Schrödinger

equation, to demonstrate its validity. In the case of the infinitely deep quantum wire the numerical values calculated agree with the analytical values to within 0.25 meV.

A brief description of how finite confining potentials can be included into the method was then given. The method was then used to calculate the electronic eigenenergies of a triangular quantum wire of finite depth that was found in the literature [62]. The calculated energies show very good agreement with that of Gangopahdhyay [62], with the difference in eigenenergies ranging between 1 and 10 meV. This difference is likely to arise from the simplified constant effective mass Hamiltonian. The method has the advantage of being relatively fast, where a typical iteration for a 100×100 mesh takes approximately 7 seconds, and is usable with any wire geometry and any potential profile.

An overview of the mathematics for the extension of the method to account for the case of variable masses was also presented.

Chapter 4

Quantum Dots

It has been shown that for the two dimensional case, or QWW, that the finite difference method is an efficient and accurate method. Now, having deduced the form of the equations and matrices needed for the two dimensional solution, it will now be extended to three dimensions.

4.1 Finite difference expansion of Schrödinger 's equation

As with the two dimensional case, the starting point is the three dimensional Schrödinger equation given by equation (3.1). The partial derivatives of the three dimensional function can be expanded in a similar manner to that of the two dimensional case and are given by,

$$\frac{\partial^2\psi(x,y,z)}{\partial x^2} \approx \frac{\psi(x+\delta x,y,z) - 2\psi(x,y,z) + \psi(x-\delta x,y,z)}{(\delta x)^2} \tag{4.1}$$

$$\frac{\partial^2\psi(x,y,z)}{\partial y^2} \approx \frac{\psi(x,y+\delta y,z) - 2\psi(x,y,z) + \psi(x,y-\delta y,z)}{(\delta y)^2} \tag{4.2}$$

$$\frac{\partial^2\psi(x,y,z)}{\partial z^2} \approx \frac{\psi(x,y,z+\delta z) - 2\psi(x,y,z) + \psi(x,y,z-\delta z)}{(\delta z)^2} \tag{4.3}$$

Substituting into the Schrödinger equation and rearranging, while ensuring the the step values $\delta x, \delta y$ and δz are small enough so that the approximation is valid, yields

$$\begin{aligned}\frac{-\hbar^2}{2m^*}\Bigg[&\frac{\psi(x+\delta x,y,z) - 2\psi(x,y,z) + \psi(x-\delta x,y,z)}{(\delta x)^2} \\ &+ \frac{\psi(x,y+\delta y,z) - 2\psi(x,y,z) + \psi(x,y-\delta y,z)}{(\delta y)^2} \\ &+ \frac{\psi(x,y,z+\delta z) - 2\psi(x,y,z) + \psi(x,y,z-\delta z)}{(\delta z)^2}\Bigg] \\ &\approx \Big(E_{x,y,z} - V(x,y,z)\Big)\psi(x,y,z)\end{aligned} \tag{4.4}$$

After some algebraic manipulation, it can be shown that equation (4.4) yields the general form of the finite difference expansion of the Schrödinger equation and is given by,

$$\begin{aligned}&(\delta y)^2(\delta z)^2\left[\psi(x+\delta x,y,z) + \psi(x-\delta x,y,z)\right] \\ &+ (\delta x)^2(\delta z)^2\left[\psi(x,y+\delta y,z) + \psi(x,y-\delta y,z)\right] \\ &+ (\delta x)^2(\delta y)^2\left[\psi(x,y,z+\delta z) + \psi(x,y,z-\delta z)\right] \\ &- \Bigg[\frac{-2m^*}{\hbar^2}\Big(E_{x,y,z} - V(x,y,z)\Big)(\delta x)^2(\delta y)^2(\delta z)^2 \\ &\quad + 2\left[(\delta y)^2(\delta z)^2 + (\delta x)^2(\delta z)^2 + (\delta x)^2(\delta y)^2\right]\Bigg]\psi(x,y,z) = 0\end{aligned} \tag{4.5}$$

Equation (4.5) can be further simplified by setting $\delta x = \delta z = \delta y$, yielding

$$\begin{aligned}&\psi(x+\delta x,y,z) + \psi(x-\delta x,y,z) + \psi(x,y+\delta y,z) + \psi(x,y-\delta y,z) \\ &+ \psi(x,y,z+\delta z) + \psi(x,y,z-\delta z) - k\psi(x,y,z) = 0\end{aligned} \tag{4.6}$$

where

$$k = \frac{-2m^*}{\hbar^2}\Big(E_{x,y,z} - V(x,y,z)\Big)(\delta y)^2 + 6 \tag{4.7}$$

It is worth noting that equation (4.7) is almost identical to equation (3.15) of the two dimensional case, except for the constant term which now has a value of 6 as compared to the value of 4 for the two dimensional case. This is due to the fact that in the present case each wave function point now has 6 nearest neighbours (see figure 4.1) as compared to 4 nearest neighbours for the two dimensional case. Now in order to arrive at the matrix equation consider the simple case of a quantum box of dimensions L_x, L_y and L_z. The box can discretized in such a way that, by choosing appropriate scales, the dimensions of the box can be represented by a total of $n_1 + 2$ elements for the y dimension, $n_2 + 2$ for the z dimension and $n_3 + 2$ for the x dimension. This arrangement is shown schematically in figure 4.1. Thus equation (4.6) can be further simplified to give

$$\psi_{i,j,l+1} + \psi_{i,j,l-1} + \psi_{i,j-1,l} + \psi_{i,j+1,l} + \psi_{i+1,j,l} + \psi_{i-1,j,l} - k\psi_{i,j,l} = 0 \tag{4.8}$$

where i, j, l are the array indices of the wave function points. As before an initial value must be selected and is given by

$$\psi_{1,1,1} = 1 \tag{4.9}$$

4.1.1 Matrix equation

As before, the problem can be formulated as a matrix equation in the form of equation (3.17). The set of simultaneous equations generated by equation (4.8) can be converted to a two dimensional array, $\mathbf{A}$, of wave function coefficients, a column vector, $\mathbf{\Psi}$, of wave function points and a column vector, $\mathbf{S}$, of source terms which arise from the perturbation value $\psi_{1,1,1}$.

Again, the standard boundary conditions

$$\psi(x,y,z) \to 0 \text{ as } x, y \text{ or } z \to \pm\infty \tag{4.10}$$

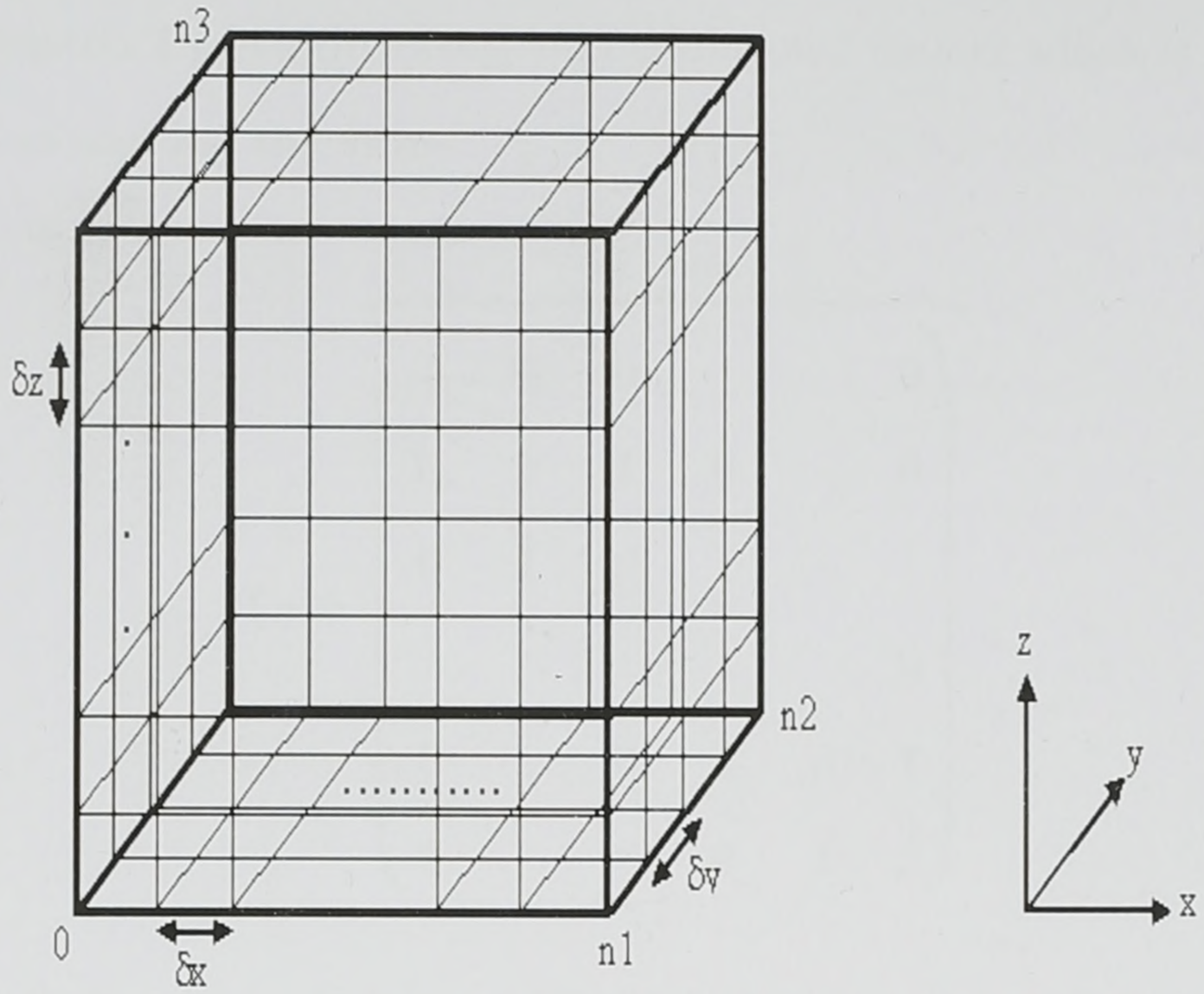

Figure 4.1: Schematic showing discretized box.

are imposed on all solutions and this is accomplished by forcing all the outermost array elements to zero.

The form of the matrices can be derived in a similar manner to that of the two dimensional case, i.e by considering a small mesh. It can be shown that the matrix **A** is an $n \times n$ sparse matrix, where $n = [n_1 \times n_2 \times n_3] - 1$ and has the same general form as that of the two dimensional case. Again, the best way to represent this matrix is by using sub-matrices. In the present case the matrix contains n_1 sub-matrices such that the total matrix has the form

$$\mathbf{A} = \overbrace{\begin{pmatrix} \mathbf{\Gamma_1} & \mathbf{D_1} & \mathbf{0} & \cdots & \cdots & \mathbf{0} \\ \mathbf{D_2} & \mathbf{\Gamma} & \mathbf{D} & \mathbf{0} & \cdots & \mathbf{0} \\ \mathbf{0} & \mathbf{D} & \mathbf{\Gamma} & \mathbf{D} & \ddots & \vdots \\ \vdots & \ddots & \ddots & \ddots & \ddots & \mathbf{0} \\ \mathbf{0} & \cdots & \mathbf{0} & \mathbf{D} & \mathbf{\Gamma} & \mathbf{D} \\ \mathbf{0} & \cdots & \cdots & \mathbf{0} & \mathbf{D} & \mathbf{\Gamma} \end{pmatrix}}^{n_1 \text{ blocks}} \tag{4.11}$$

where, the sub-matrix $\mathbf{\Gamma_1}$ is a $([n_2 \times n_3] - 1)$ tridiagonal matrix which is itself comprised of n_2 sub-matrices and has the form

$$\mathbf{\Gamma_1} = \overbrace{\begin{pmatrix} \beta_1 & \mathbf{I_1} & \mathbf{0} & \cdots & \cdots & \mathbf{0} \\ \mathbf{I_2} & \beta & \mathbf{I} & \mathbf{0} & \cdots & \mathbf{0} \\ \mathbf{0} & \mathbf{I} & \beta & \mathbf{I} & \ddots & \vdots \\ \vdots & \ddots & \ddots & \ddots & \ddots & \mathbf{0} \\ \mathbf{0} & \cdots & \mathbf{0} & \mathbf{I} & \beta & \mathbf{I} \\ \mathbf{0} & \cdots & \cdots & \mathbf{0} & \mathbf{I} & \beta \end{pmatrix}}^{n_2 \text{ blocks}} \tag{4.12}$$

The sub-matrix $\beta_\mathbf{1}$ is a $[n_3 - 1] \times [n_3 - 1]$ matrix and has the same form as that of the two dimensional case that is given by equation (3.46). All the remaining β sub-matrices have the same form as that of $\beta_\mathbf{1}$, but are all $n_3 \times n_3$ matrices.

The sub-matrix $\mathbf{D_1}$ is a $([n_2 \times n_3] \times [n_2 \times n_3] - 1])$ diagonal matrix which in itself is comprised of n_2 sub-matrices and has the form

$$\mathbf{D}_1 = \overbrace{\begin{pmatrix} \mathbf{I}_1 & \mathbf{0} & \cdots & \cdots & \mathbf{0} \\ \mathbf{0} & \mathbf{I} & \mathbf{0} & \cdots & \mathbf{0} \\ \mathbf{0} & \ddots & \ddots & \ddots & \vdots \\ \vdots & \ddots & \mathbf{0} & \mathbf{I} & \mathbf{0} \\ \mathbf{0} & \cdots & \cdots & \mathbf{0} & \mathbf{I} \end{pmatrix}}^{n_2 \text{ blocks}} \tag{4.13}$$

The sub-matrix $\mathbf{D_2}$ is a $([n_2 \times n_3] - 1] \times [n_2 \times n_3])$ diagonal matrix which in itself is comprised of n_2 sub-matrices and has the form

$$\mathbf{D_2} = \overbrace{\begin{pmatrix} \mathbf{I_2} & \mathbf{0} & \cdots & \cdots & \mathbf{0} \\ \mathbf{0} & \mathbf{I} & \mathbf{0} & \cdots & \mathbf{0} \\ \mathbf{0} & \ddots & \ddots & \ddots & \vdots \\ \vdots & \ddots & \mathbf{0} & \mathbf{I} & \mathbf{0} \\ \mathbf{0} & \cdots & \cdots & \mathbf{0} & \mathbf{I} \end{pmatrix}}^{n_2 \text{ blocks}} \tag{4.14}$$

The sub-matrix $\mathbf{I_1}$ is a $(n_3 \times [n_3 - 1])$ matrix which has the same form as that of the two dimensional case and is given by equation (3.47). The sub-matrix $\mathbf{I_2}$ is a $([n_3 - 1] \times n_3)$ and again has the same form as for the two dimensional case and is given by equation (3.48). All the remaining $\mathbf{I}$ sub-matrices are $n_3 \times n_3$ identity matrices. The remainder of the matrix $\mathbf{A}$ is comprised of zeroes.

The column vector $\mathbf{\Psi}$ will consist of $n = [n_1 \times n_2 \times n_3] - 1$ elements, which is the total number of unknown elements and is given by equation (4.15). It consists of a total of n_1 blocks each of length $n_2 \times n_3$ elements, with the exception of the first block which consists of $[n_2 \times n_3] - 1$ elements since $\psi_{1,1,1}$ is already determined.

$$\mathbf{\Psi} = \begin{pmatrix} \psi_{1,1,2} \\ \psi_{1,1,3} \\ \vdots \\ \psi_{1,1,n_3} \\ \psi_{1,2,1} \\ \vdots \\ \psi_{1,n_2,n_3} \\ \psi_{2,1,1} \\ \vdots \\ \psi_{n_1,n_2,n_3} \end{pmatrix} \tag{4.15}$$

Finally, the matrix **S** is a column vector of length n and is of the form

$$\mathbf{S} = \begin{pmatrix} -\psi_{1,1,1} \\ 0 \\ \vdots \\ 0 \\ -\psi_{1,1,1} \\ 0 \\ \vdots \\ 0 \\ -\psi_{1,1,1} \\ 0 \\ \vdots \\ 0 \end{pmatrix} \begin{matrix} \left.\begin{matrix} \\ \\ \\ \end{matrix}\right\} n_3 - 1 \text{ zeroes} \\ \left.\begin{matrix} \\ \\ \\ \end{matrix}\right\} n_2 \times n_3 \text{ zeroes} \\ \left.\begin{matrix} \\ \\ \\ \end{matrix}\right\} \end{matrix} \tag{4.16}$$

4.1.2 Correct physical solutions

As with the two dimensional case, the boundary conditions can not be used to identify the correct physical solutions since all solutions forcibly satisfy the boundary conditions. The approach of identifying the correct solutions by locating the energies at which the wave function has well defined global maxima away from the initial condition at the corner can again be utilised.

However, it was noted that after achieving a maximum peak value at the correct eigenenergy, that the entire wave function will abruptly change signs, so that the well defined maxima become well defined minima and vice versa, at an energy slightly higher than the eigenenergy. It is worth mentioning that the value of the initial condition at the corner remains unchanged. These inverted maxima and minima gradually decrease in magnitude as the energy is increased until once again the initial condition dominates the wave function. While the eigenenergies are narrow in the energy domain, this behaviour of inverting signs is easily detectable over a relatively wide range in the energy domain.

In order to exploit this behaviour, the wave function is scanned to determine the sign of the maximum and minimum values. The product of these two is then plotted versus the energy, and the point at which the product changes signs from positive to negative is a good estimate of the position of the ground state eigenenergy. The advantage of this approach is that a good estimate for the eigenenergy can be obtained quickly since the energy can be incremented in large steps as opposed to the small increments that need to be used with the previous method. This estimate can then be used to identify the correct energy more efficiently. The disadvantage being that it can only be used to identify the ground state eigenenergy.

4.2 Infinitely deep quantum box

The initial test system to be investigated was the simple case of an infinitely deep quantum box, see figure 4.2. This provides a good starting point since analytical solutions are readily available [27] and are given by

$$E_{x,y,z} = \frac{\hbar^2\pi^2}{2m^*}\left(\frac{n_x^2}{L_x^2} + \frac{n_y^2}{L_y^2} + \frac{n_z^2}{L_z^2}\right) \tag{4.17}$$

Where n_x, n_y, and n_y are the three quantum numbers required to label each state and L_x, L_y, and L_z are the dimensions of the box. The box under investigation had the dimensions $L_x = L_y = L_z = 100$ Å and the parameters used were $V = 0$ and $m^* = 0.0665m_0$ which gives the value of the ground state as $E_{x,y,z} = 169.6$ meV. The ground state energy was then calculated using the finite difference method for a number of different mesh sizes. Figure 4.3 shows a plot of the calculated ground state energy against the number of mesh points in each direction, along with the analytical value. As the mesh size is increased the calculated value tends towards the analytical value, and since calculating the energy within a few meV of the correct value is usually sufficient it seems unnecessary to use larger mesh sizes than the ones displayed.

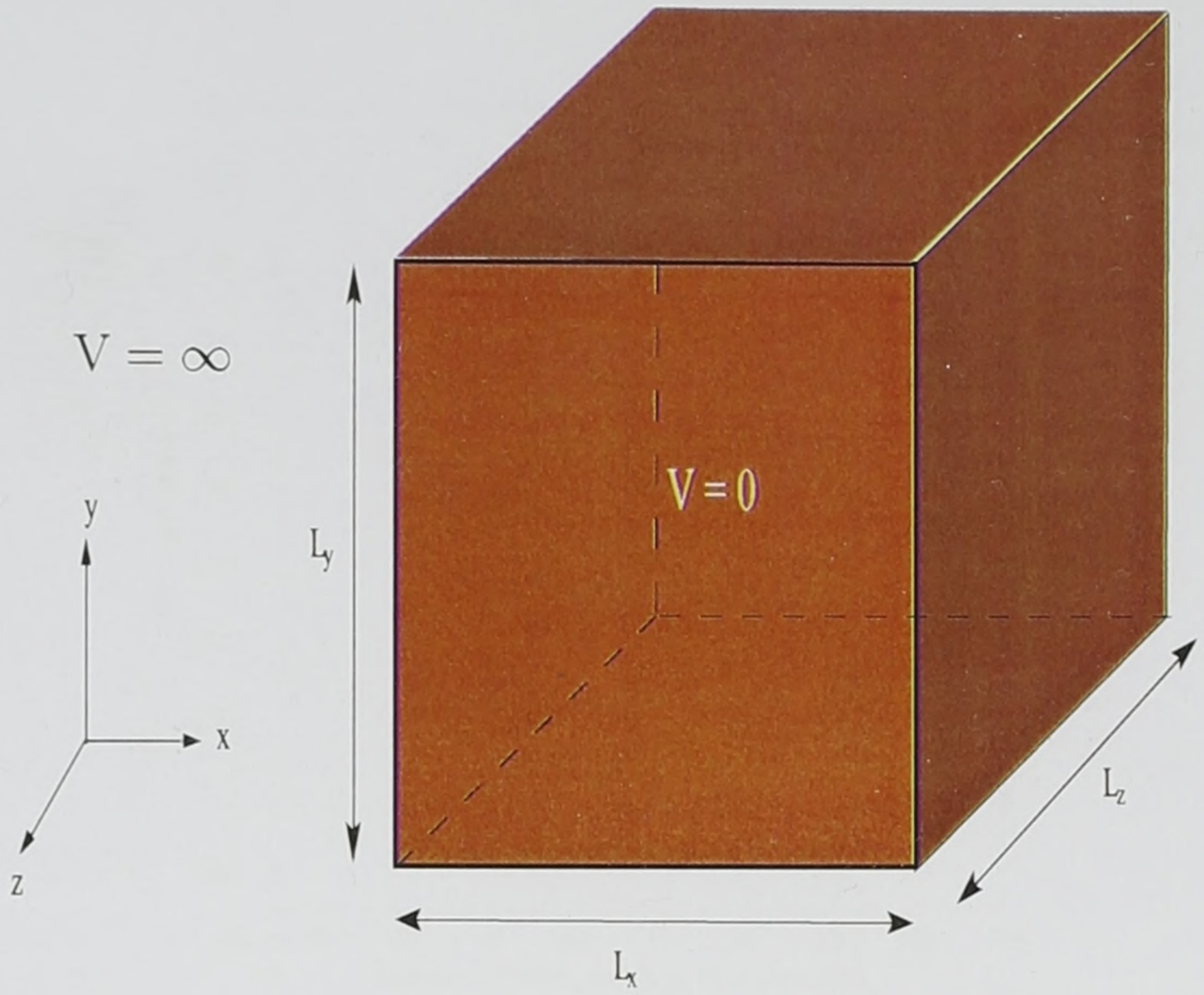

Figure 4.2: Infinitely deep quantum box, $V = 0$ inside and $V = \infty$ outside the box.

The wave functions obtained from these calculations are three dimensional and as such it was deemed necessary to plot *slices* of the wave function, i.e. plotting the $x - y$ plane at a constant value of z. Figure 4.4 shows a plot of such a slice of the normalised ground state wave function, where the mesh size used for the calculation was $100 \times 100 \times 100$ elements. Figure 4.5 shows a plot of a slice of the wave function at an energy slightly above the ground state eigenenergy. As can be seen the wave function is inverted and this is the property that is used to identify the correct ground state energy, see section(4.1.2).

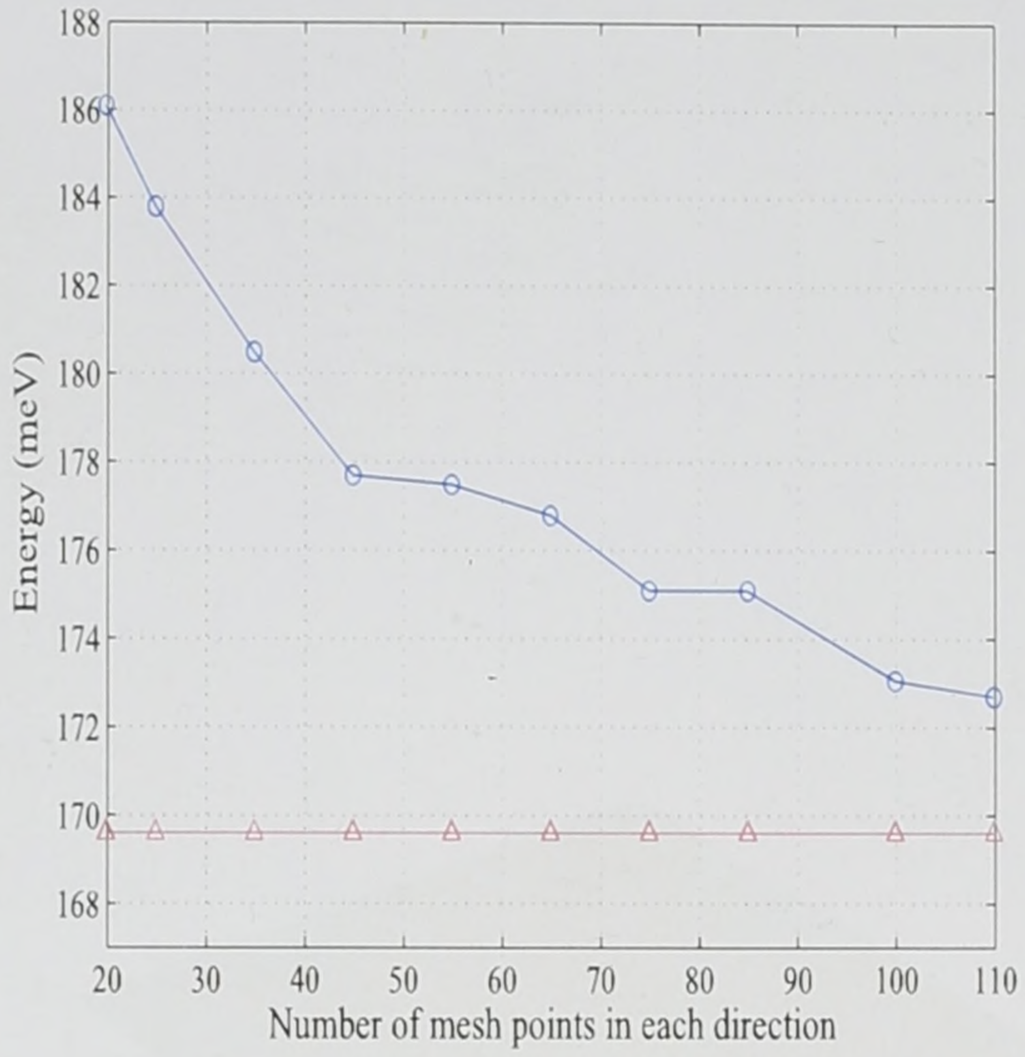

Figure 4.3: Energy vs. mesh size for a $100 \times 100 \times 100$ Å infinitely deep quantum box. Line with triangles shows analytical values and the line with circles shows the values calculated using the finite difference method.

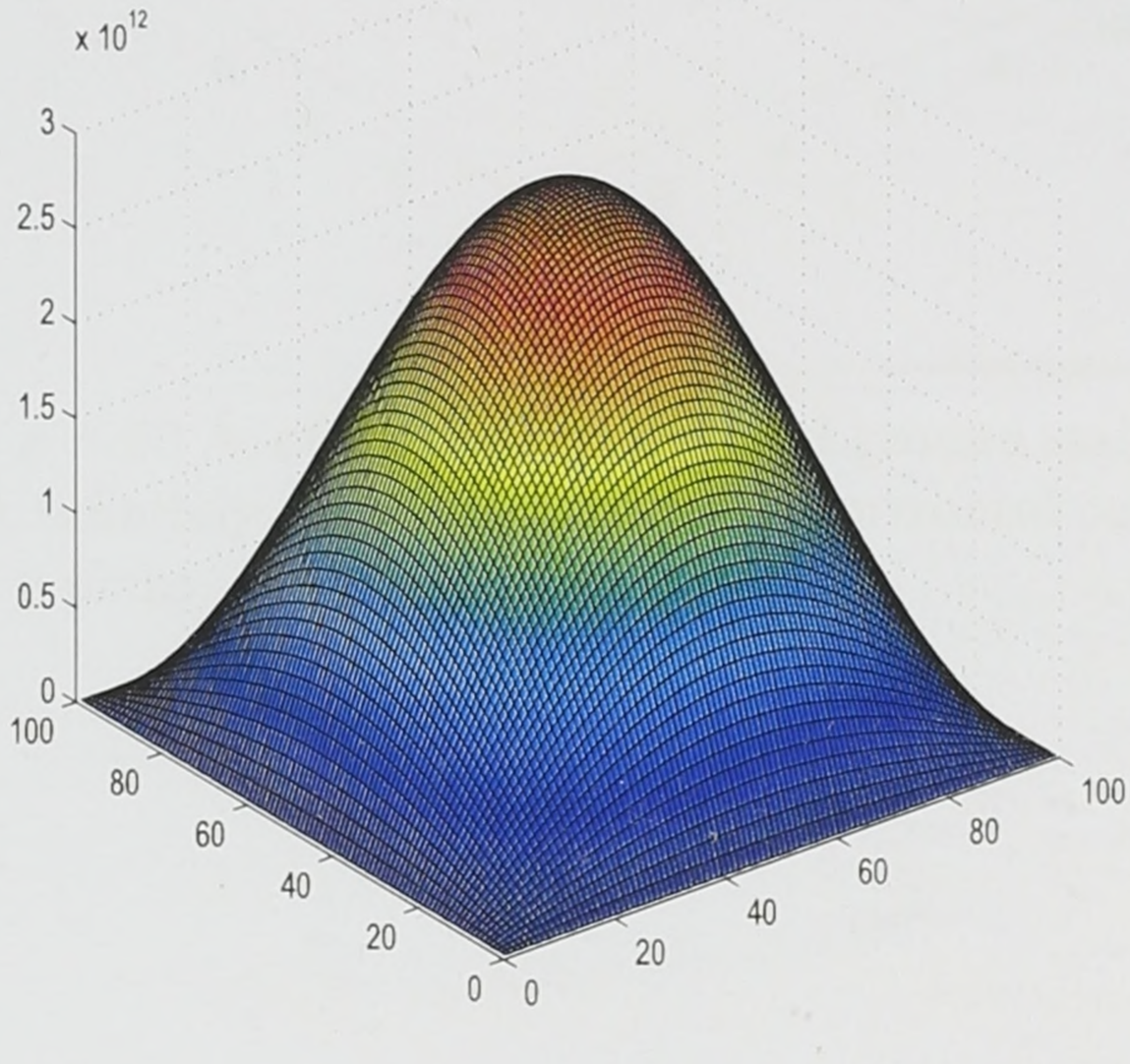

Figure 4.4: Slice, at $z = 50$ Å, of normalised ground state wave function for a $100 \times 100 \times 100$ Å infinitely deep quantum box. Horizontal coordinates represent position on the $x - y$ plane. Energy= 173.06 meV.

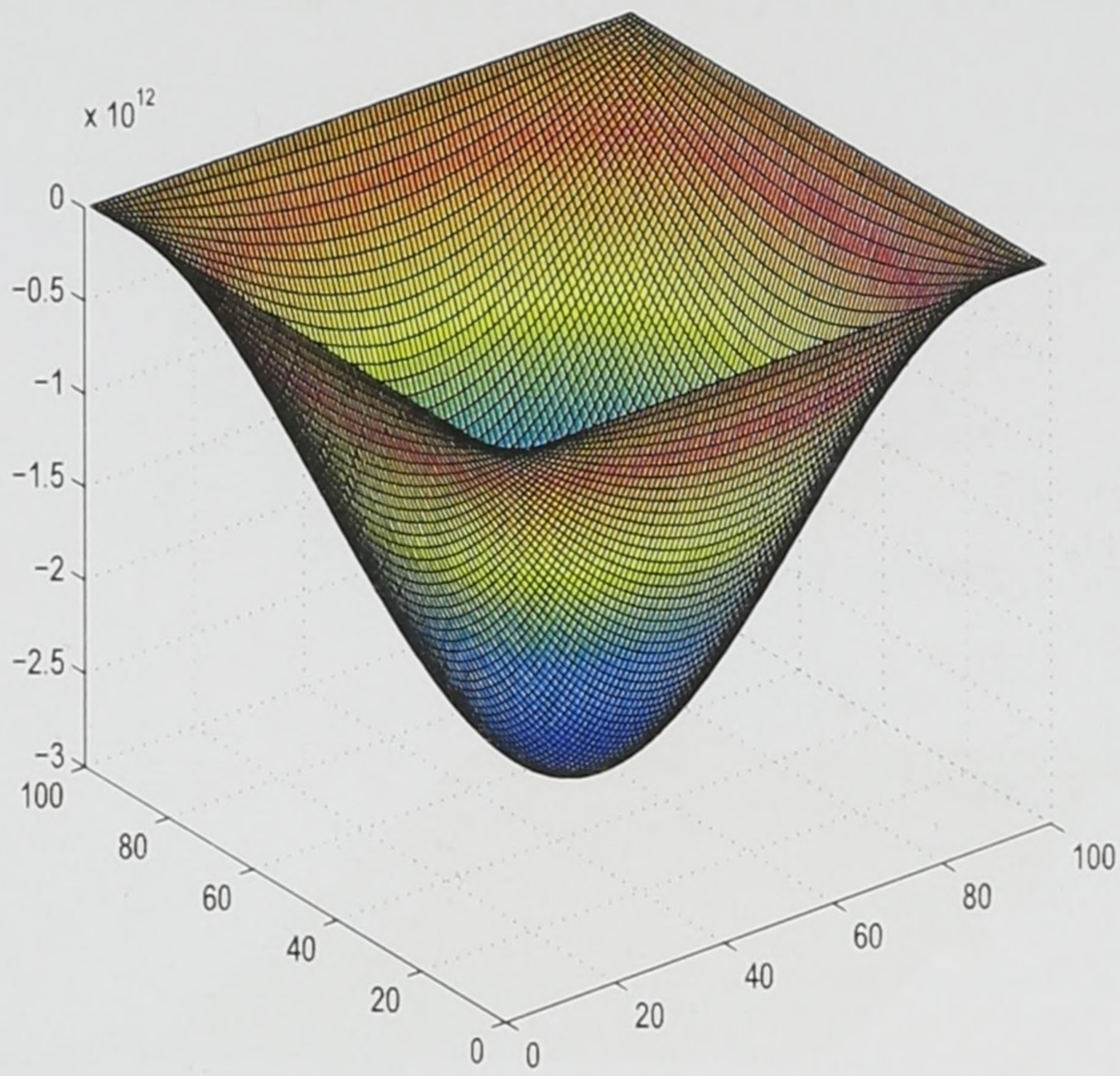

Figure 4.5: Slice, at $z = 50$ Å, of normalised inverted ground state wave function for a $100 \times 100 \times 100$ Å infinitely deep quantum box. Horizontal coordinates represent position on the $x - y$ plane. Energy= 173.07 meV.

4.3 Pyramidal quantum dot

Having demonstrated the validity of the method using an infinitely deep quantum box, the method will now be used to investigate the case of a pyramidal quantum dot of finite depth.

The system under investigation was chosen to closely resemble that found in the literature for ease of comparison [5], and is a self assembled InAs pyramidal quantum dot. A schematic of this system is displayed in figure 4.6. The values of the parameters used were: $m^* = 0.0665m_0$, $V = 276$ meV, $L_x = L_y = L_z = 520$ Å, $b = 120$ Å, $h = 60$ Å and $b_x = b_y = b_z = 200$ Å.

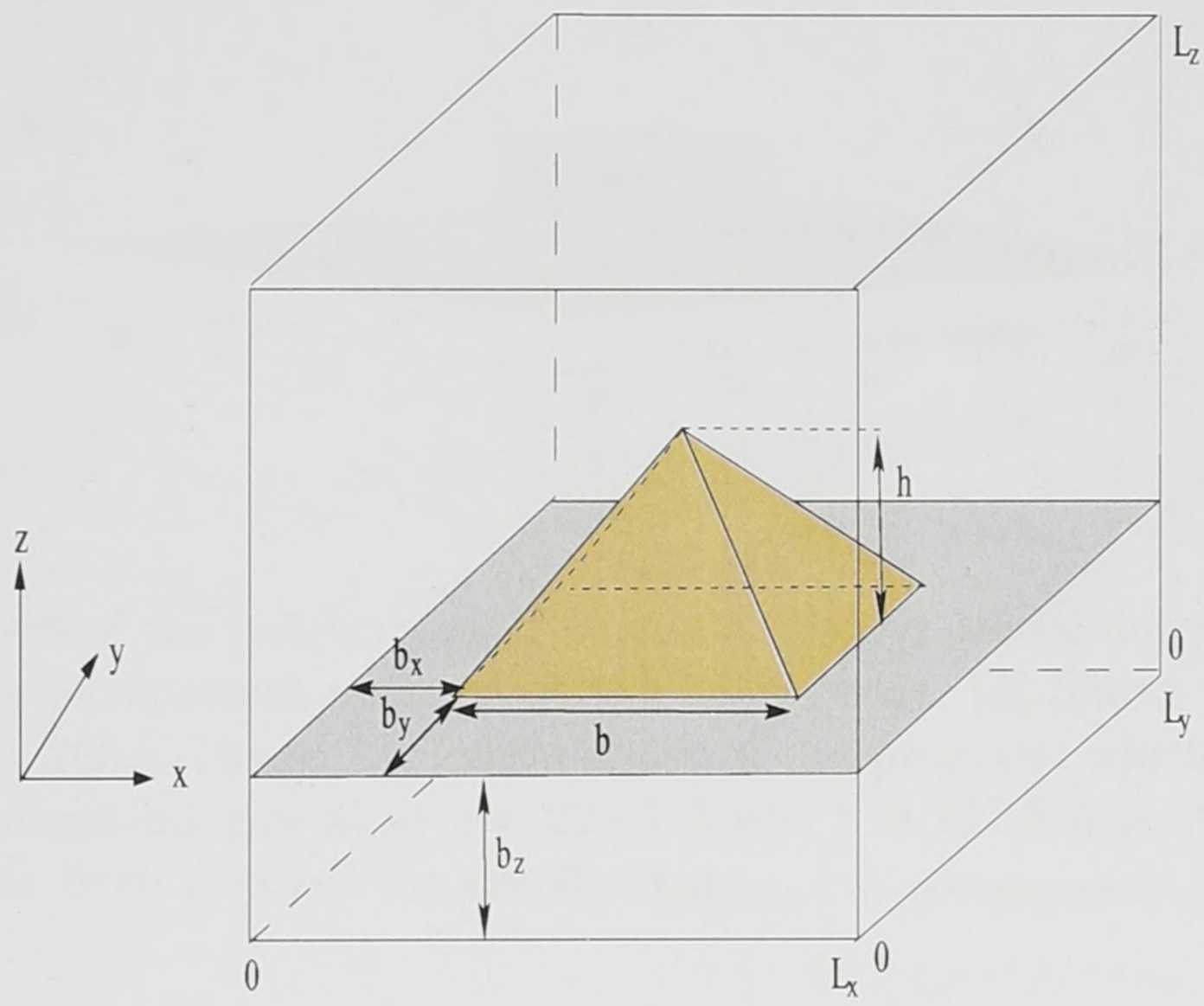

Figure 4.6: Schematic of pyramidal quantum dot.

As mentioned before all calculations assume a constant average value for the potential. In the present case the potential has the shape of a square based pyramid that is situated at the centre of the box. Figure 4.7 displays a plot of three slices representing the potential inside the box. The potential is in essence represented by squares of a constant potential of zero that are decreasing in size until they reach the apex of the pyramid, surrounded by the barrier potential with the value of 276 meV.

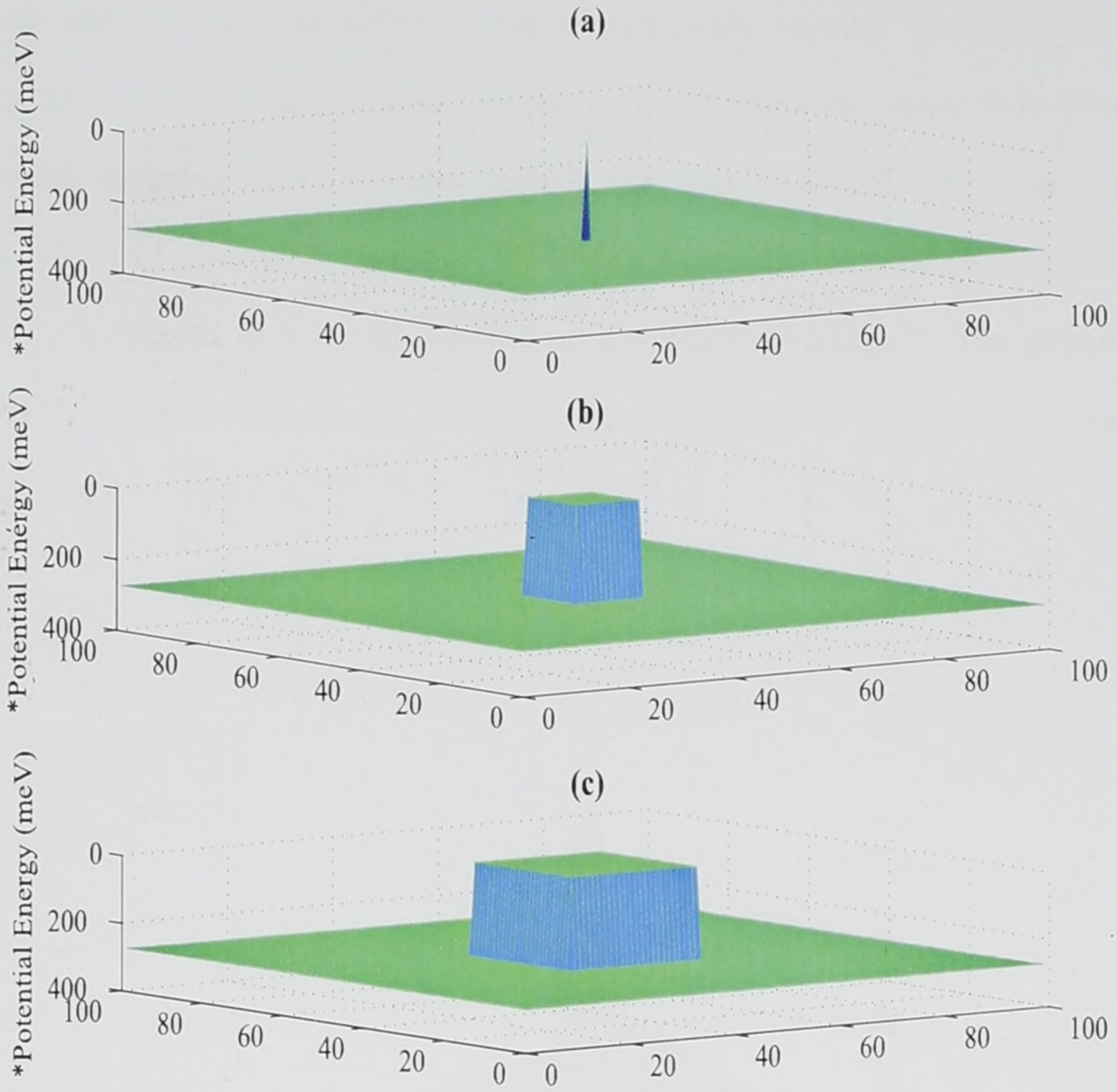

Figure 4.7: Slices of the potential used to model the pyramidal dot potential. Horizontal coordinates represent position on the $x - y$ plane. (a) Shows the apex of the pyramid at $z = 260$Å. (b) and (c) show slices of the potential which are squares of progressively increasing size at at $z = 228.8$ Å and $z = 197.6$ Å respectively. * The vertical axis has been inverted for visual clarity.

Figures 4.8, 4.9 and 4.10 show plots of the normalised ground state wave function for the pyramidal dot, where the mesh size used for the calculations was $100 \times 100 \times 100$ elements i.e. a mesh spacing of 5.2 Å. The figures correspond to slices through the middle of the dot, the uppermost edge of the dot and a slice near the top edge of the box containing the dot respectively. Figure 4.8 shows a clearly defined wave function, while figure 4.9 shows a slice of the wave function that has a sharper peak. This is due to the fact that this slice is passing through the uppermost point of the pyramidal dot, i.e. its narrowest point. Finally the wave function slice in figure 4.10 is both less localised, than the previous

two plots, as well as its peak value being considerably smaller in magnitude. This is a result of the slice being near the edge of the box and thus the wave function is decaying and is at some distance from the dot and hence less localised. It is also worth noting that all the slices of the wave function resulting from the case of the pyramidal dot are more spatially localised in a small central region corresponding to the pyramidal region, as compared to the more gradually decaying wave function of the infinitely deep quantum box, see figure 4.4.

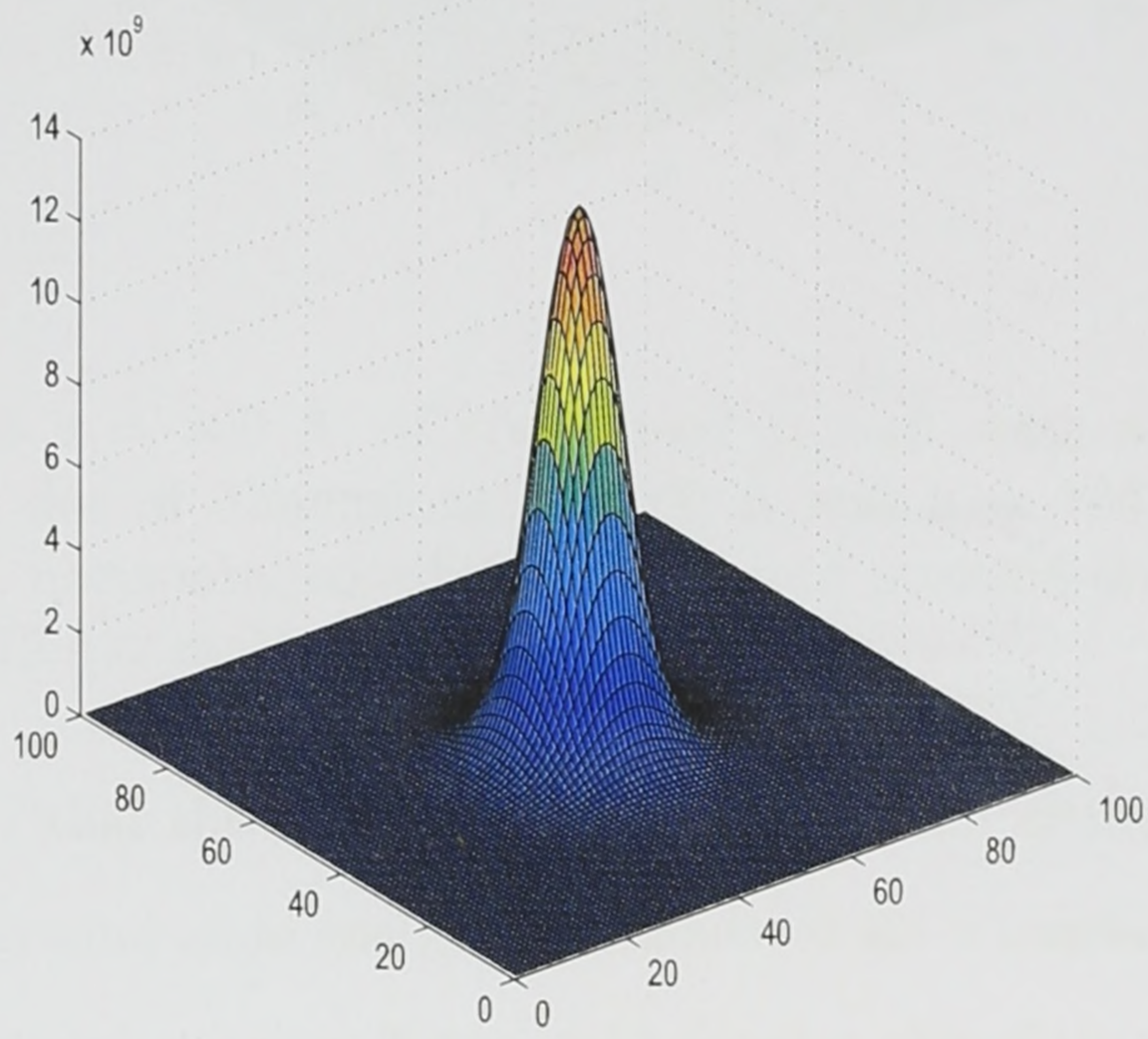

Figure 4.8: Slice, at $z = 228.8$ Å, of normalised ground state wave function for a pyramidal quantum dot of dimensions $h = 60$ Å and $h = 120$ Å, with potential barriers of 276 meV, horizontal coordinates represent position on the $x - y$ plane of the QD. Energy= 172.612 meV

4.3.1 Convergence and computation time

The eigenenergies were calculated using a number of different mesh sizes to ensure convergence. Figure 4.11 shows the ground state energy versus mesh size, along with the numerical value found in the literature [5]. It can clearly be seen that the energy converges as the mesh size is increased.

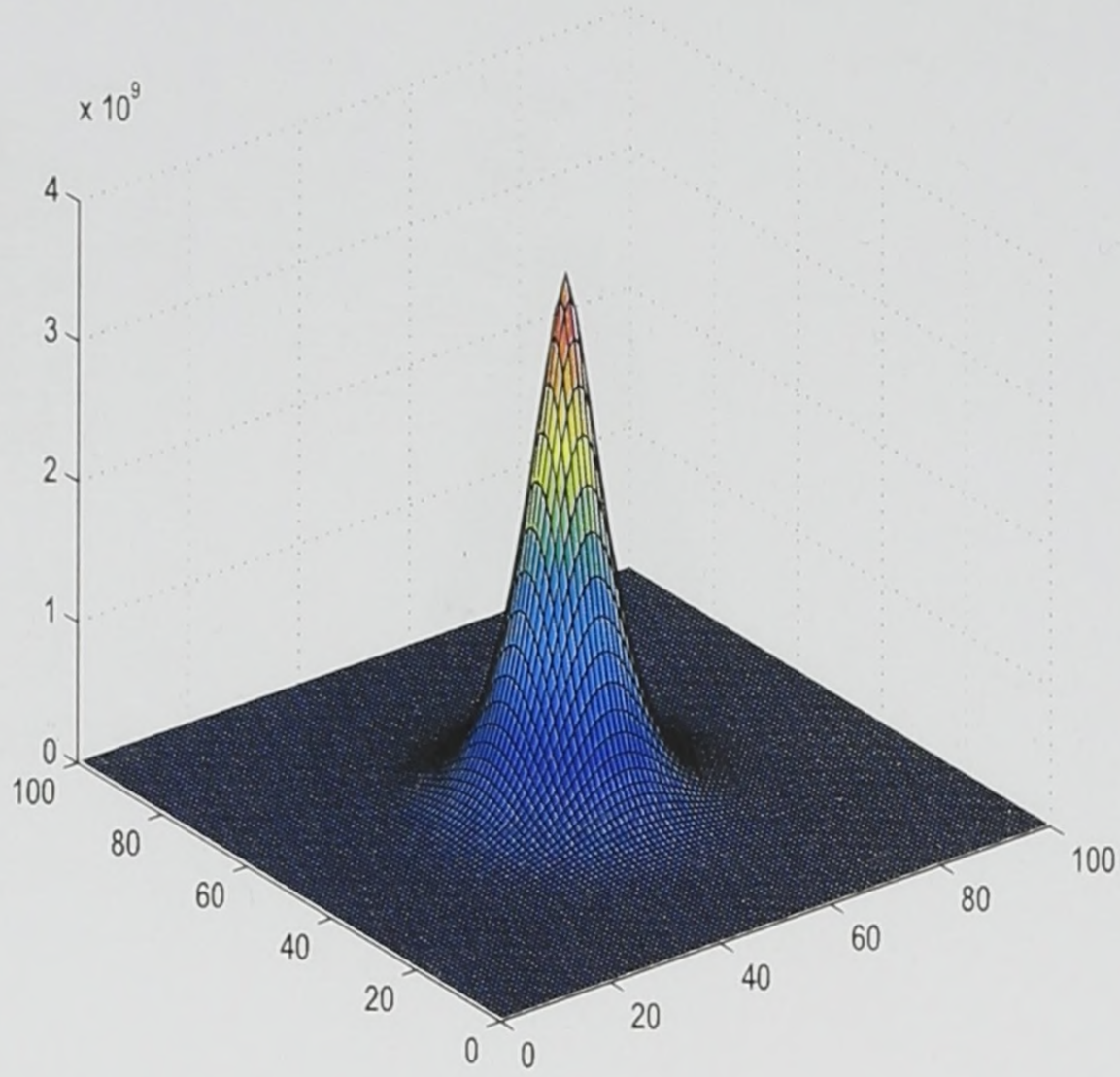

Figure 4.9: Slice, at $z = 260$ Å, of normalised ground state wave function for a pyramidal quantum dot of dimensions $h = 60$ Å and $h = 120$ Å, with potential barriers of 276 meV, horizontal coordinates represent position on the $x - y$ plane of the QD. Energy= 172.612 meV

In order to ensure that the eigenenergies are independent of the computational domain, the electronic ground state energy was calculated for a number of box sizes while maintaining the same mesh spacing. Figure 4.12 shows a plot of the ground state energy versus box size for the pyramidal quantum dot and a mesh spacing of 5.2 Å. As can be seen from the plot that for box sizes greater than 300 Å the eigenenergies are independent of the size of the computational domain.

The eigenvalue method to which a comparison was made, requires 1 Gigabyte of memory just to store the matrix [5]. The finite difference method requires only 78 Megabytes to store the matrix for a mesh size of $100 \times 100 \times 100$ elements, due to the fact that the matrix is a sparse one and about 7 Megabytes to store the final wave function. In terms of computation time, the eigenvalue method required, at best, just under 7 hours to reach a solution [5]. The finite difference method requires a significantly smaller amount of computational time, since a single iteration (over energy) requires about 10 minutes

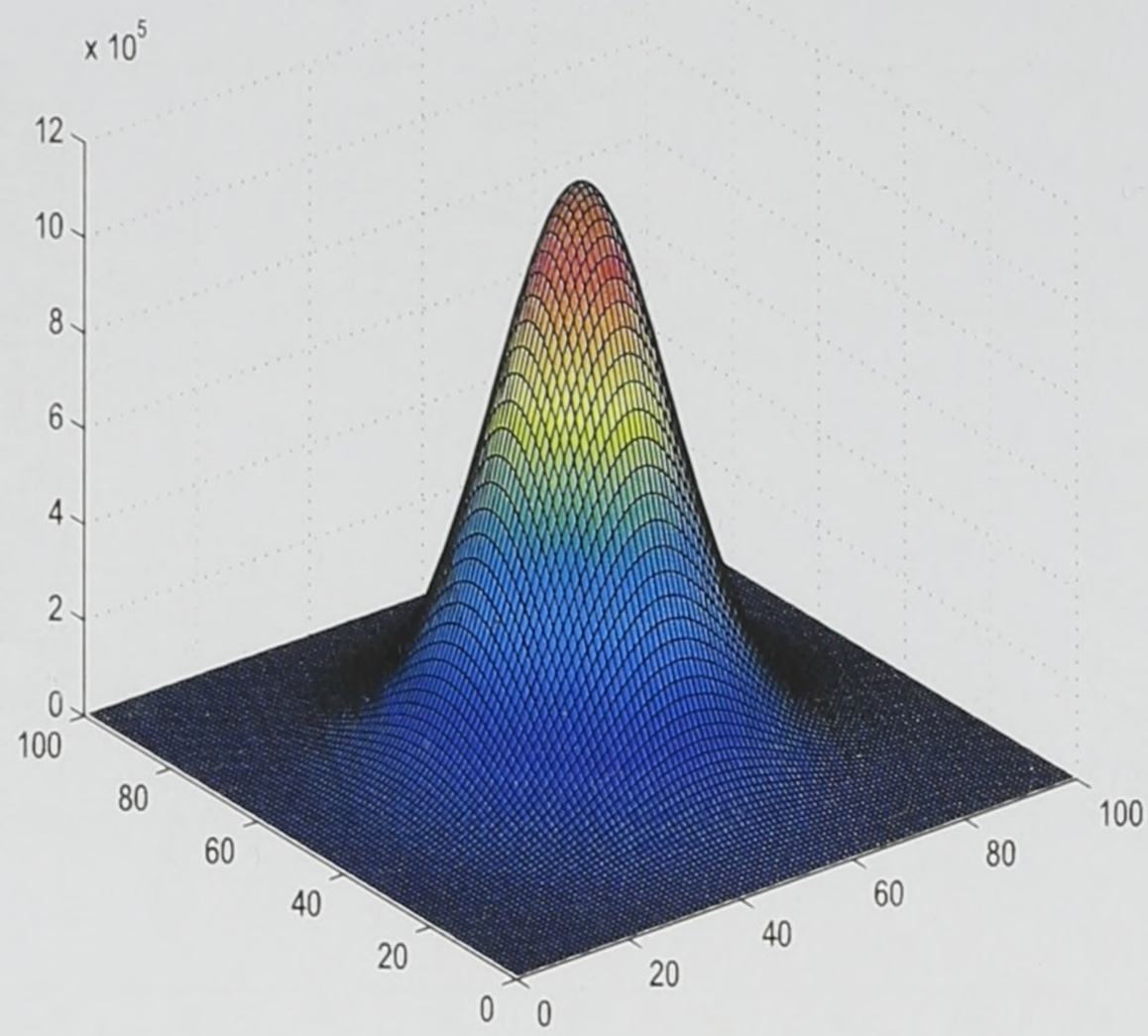

Figure 4.10: Slice, at $z = 416$ Å, of normalised ground state wave function for a pyramidal quantum dot of dimensions $h = 60$ Å and $h = 120$ Å, with potential barriers of 276 meV, horizontal coordinates represent position on the $x - y$ plane of the QD. Energy= 172.612 meV

and a solution can be found within a few iterations, depending on the initial guess. Figure 4.13 shows a plot of computation time per iteration in seconds versus the number of mesh points in each direction. The computation time was found to be related to $(\delta y)^4$, thus halving δy will increase the iteration time by approximately 16 times.

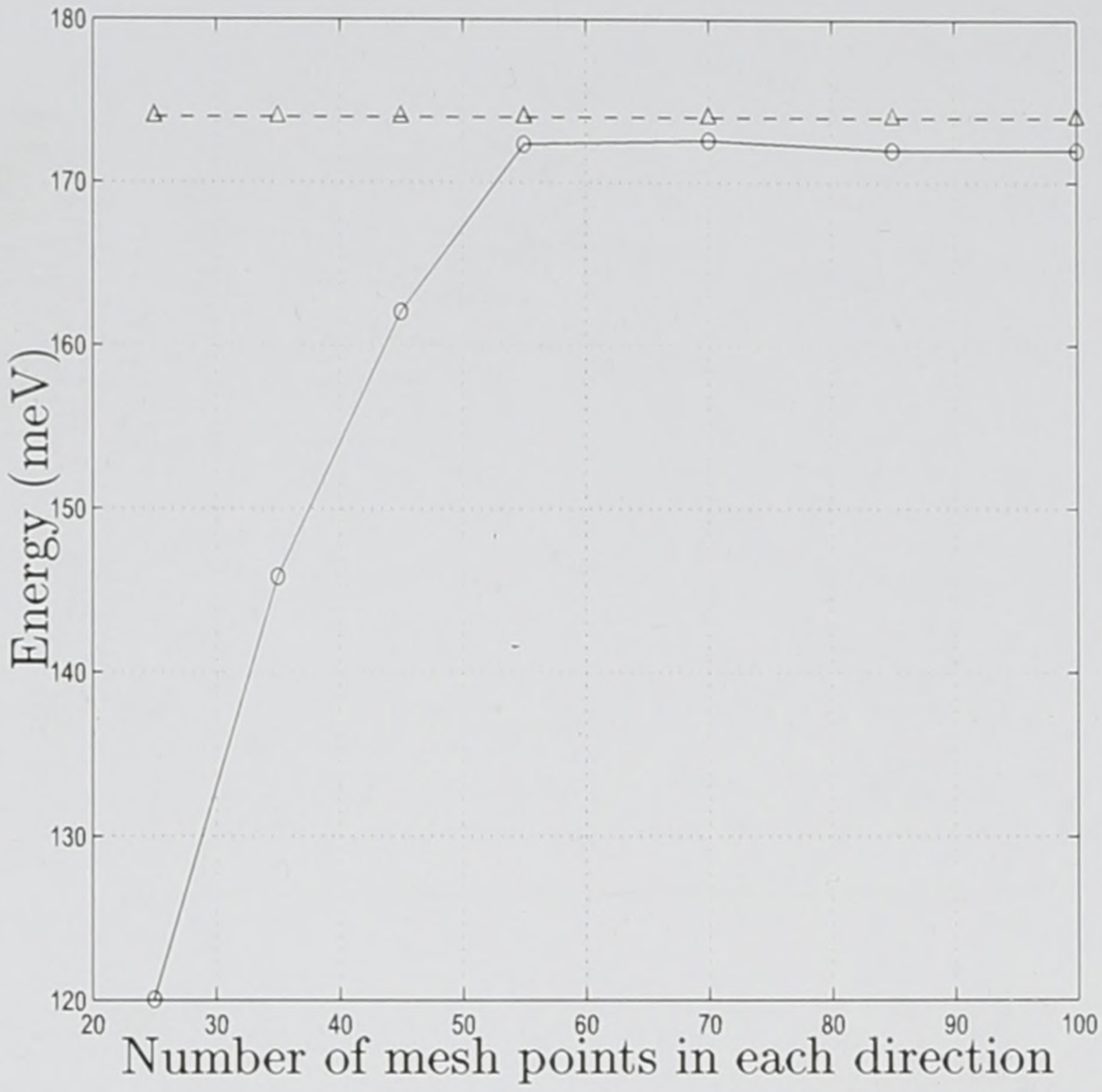

Figure 4.11: Energy vs. Mesh size for pyramidal QD. Line with triangles shows data from literature [5], line with circles data obtained using finite difference method.

Figure 4.12: Ground state energy vs. box size for pyramidal QD.

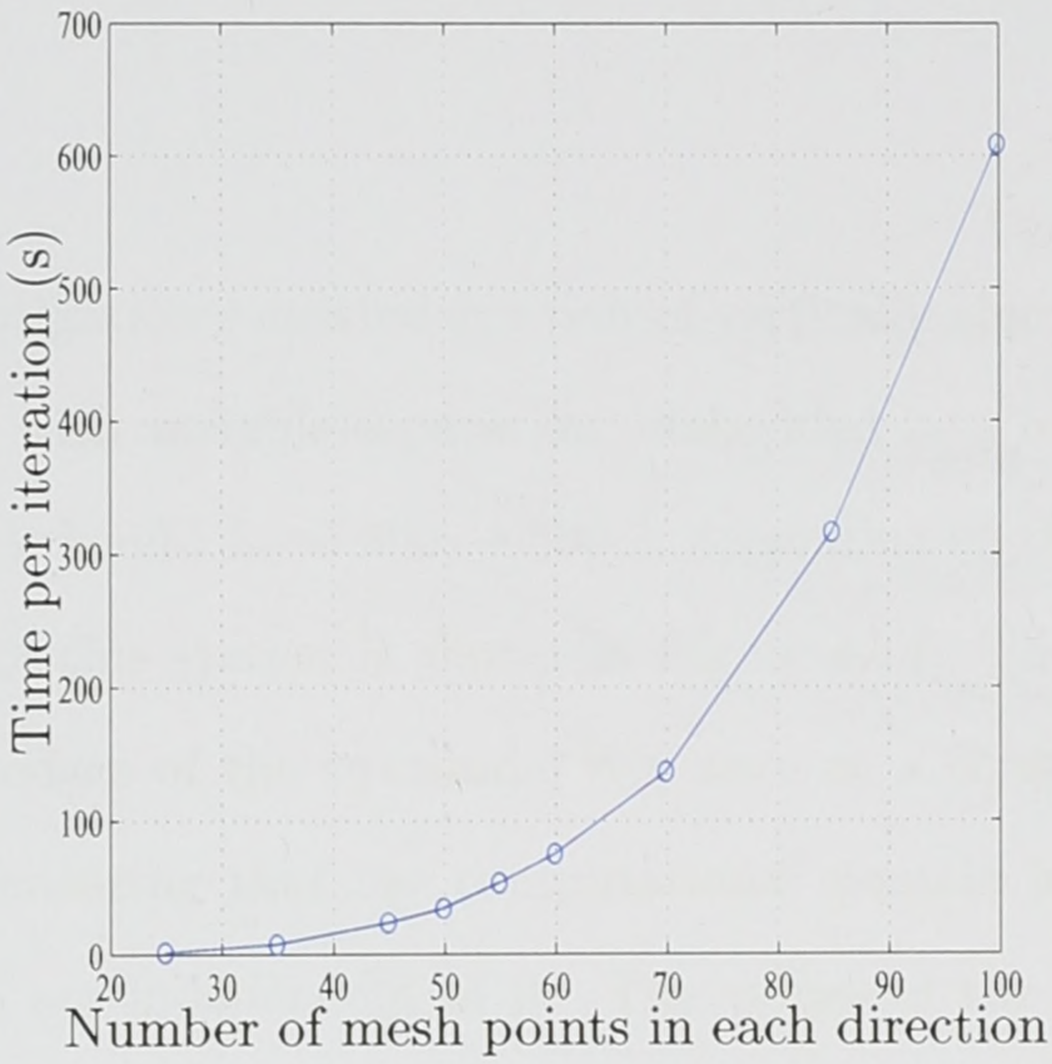

Figure 4.13: Time per iteration vs. mesh size for a pyramidal quantum dot.

4.4 Coupled quantum dots

4.4.1 Introduction

There has also been a growing interest in quantum computation, in which atomic levels and electron spins play the role of quantum bits (qubits) [68]. Each of these qubits usually consists of a pair of coupled QDs [13, 69]. A number of specific cases of laterally and vertically coupled QDs have been extensively investigated in the literature [7,8,14,68–73].

In this section the effect of the inter-dot separation on the energy levels of two vertically aligned QDs is investigated using the finite difference technique [74].

4.4.2 Results

The system under investigation consisted of a pair of vertically aligned pyramidal quantum dots of zero potential, with variable separation, embedded in a box of dimensions $L_x = L_y = 520$ Å and variable height $L_z = 600 \rightarrow 690$ Å depending on the inter-dot separation. A schematic diagram of this system is shown in Figure 4.14. The height was chosen so as to ensure that the edges of the pyramidal dot were at a constant distance from the edge of the box thus ensuring that the computational domain is large enough so that the energy eigenvalues are independent of it. The values of the parameters used were: $m^* = 0.0665m_0$, and $V = 276$ meV and the scale used was $\delta y = 9.45$ Å which was chosen for convergence purposes, see figure 4.11. In the previous section it was shown that as δy is decreased the energy goes to a fixed value. This choice of $\delta y = 9.45$ Å was shown to give the energy of the quantum dot to within 0.2 meV of the converged value. While decreasing δy improves the numerical accuracy of the solution, it of course leads to the use of more sampling points and hence larger memory requirements and increased computation times. The choice of δy used here corresponds to a mesh of $55 \times 55 \times 55$ elements for a typical quantum dot.

The quantum dots used were of slightly different dimensions, to avoid degeneracy, where the top dot had a height of $h = 60$ Å and a base length of $b = 120$ Å and the lower

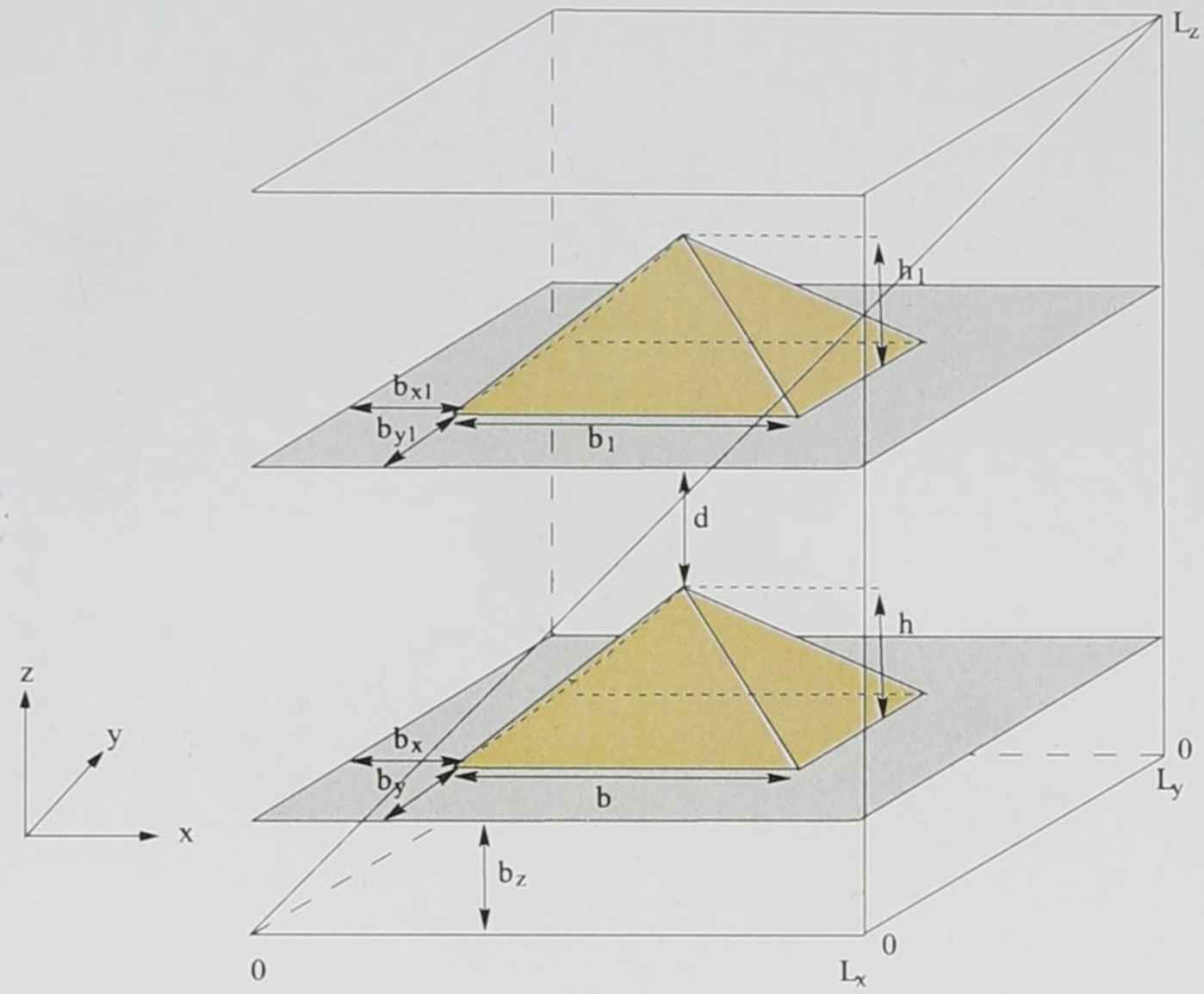

Figure 4.14: Schematic showing box with two embedded pyramidal dots with zero potential.

dot had the dimensions $h = 70$ Å and $b = 140$ Å. The dimensions of the smaller dot were chosen to correspond to those previously investigated [74], while the larger dot was chosen so that there was a slight difference in dimensions while maintaining an aspect ratio of 2 so as to be comparable to the values found in the literature [5]. The potential is modelled as two stacked square based pyramids of a potential of zero surrounded by the barrier potential of value 276 meV. Figure 4.15 shows a cross section of the potential, the $x - z$ plane at a constant y, for the case of 40 Å separation.

To investigate the effect of the proximity of second dot on the ground state of a given dot, the difference in the ground state energy between the single dot case (E^{1dot}) and the two dot case (E^{2dots}) was plotted versus the dot separation and is displayed in figure 4.16.

As can be seen from figure 4.16, when the dots are in close proximity the ground state, or bonding state, energy is lower than that of the single dot case. This is due to the interaction between the dots and the fact that the total potential is lower due to the presence of the second dot. The wave function clearly reflects this interaction.

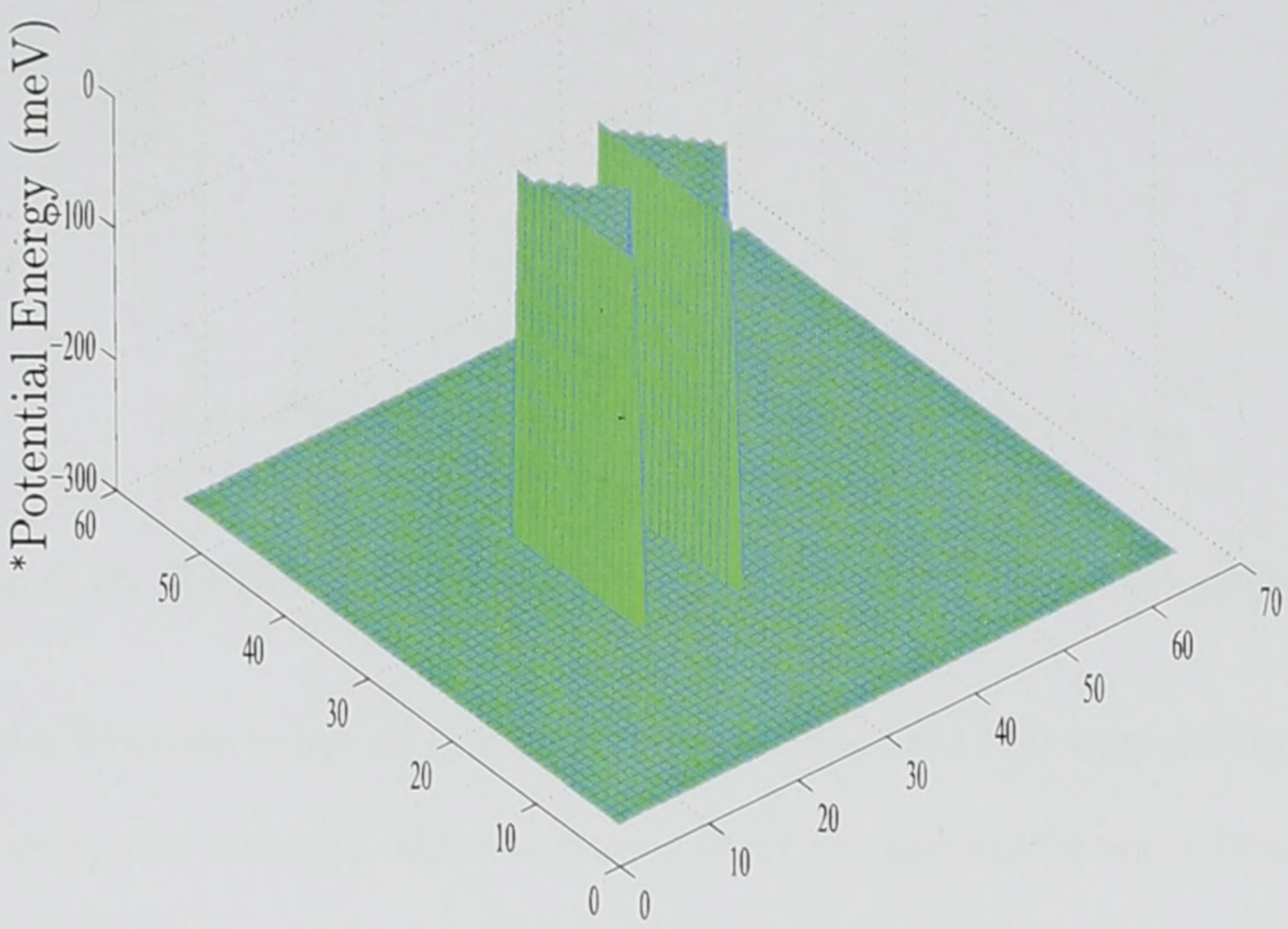

Figure 4.15: Slice of the potential used to model the quantum dot potentials for the example case of 40 Å separation. Horizontal coordinates represent position on the $x - z$ plane, and $y = 255.15$ Å. *The vertical potential axis has been inverted for visual clarity.

Again, since the wave functions obtained from these calculations are three dimensional it was necessary to plot slices of the wave function. Figure 4.17 shows vertical slices, the $x - z$ plane for a constant value of y, of the wave function for a number of different dot separations. At large separations, the wave function displays a maximum over the larger quantum dot, due to its lower energy, indicating that the lowest energy electron is localised in this larger dot and in effect isolated from the smaller dot. As the dots get closer a "shoulder" appears on the side of the wave function, spatially located over the smaller dot. This shoulder, which becomes evident at distances of less than 40 Å, indicates that there is a finite probability of the lowest energy electron existing in either of the two dots.

Figure 4.18 is a plot of stacked horizontal slices, the $x - y$ plane for a constant value of z, of the ground state for a dot separation of 100 Å and energy 147.59 meV. The slices

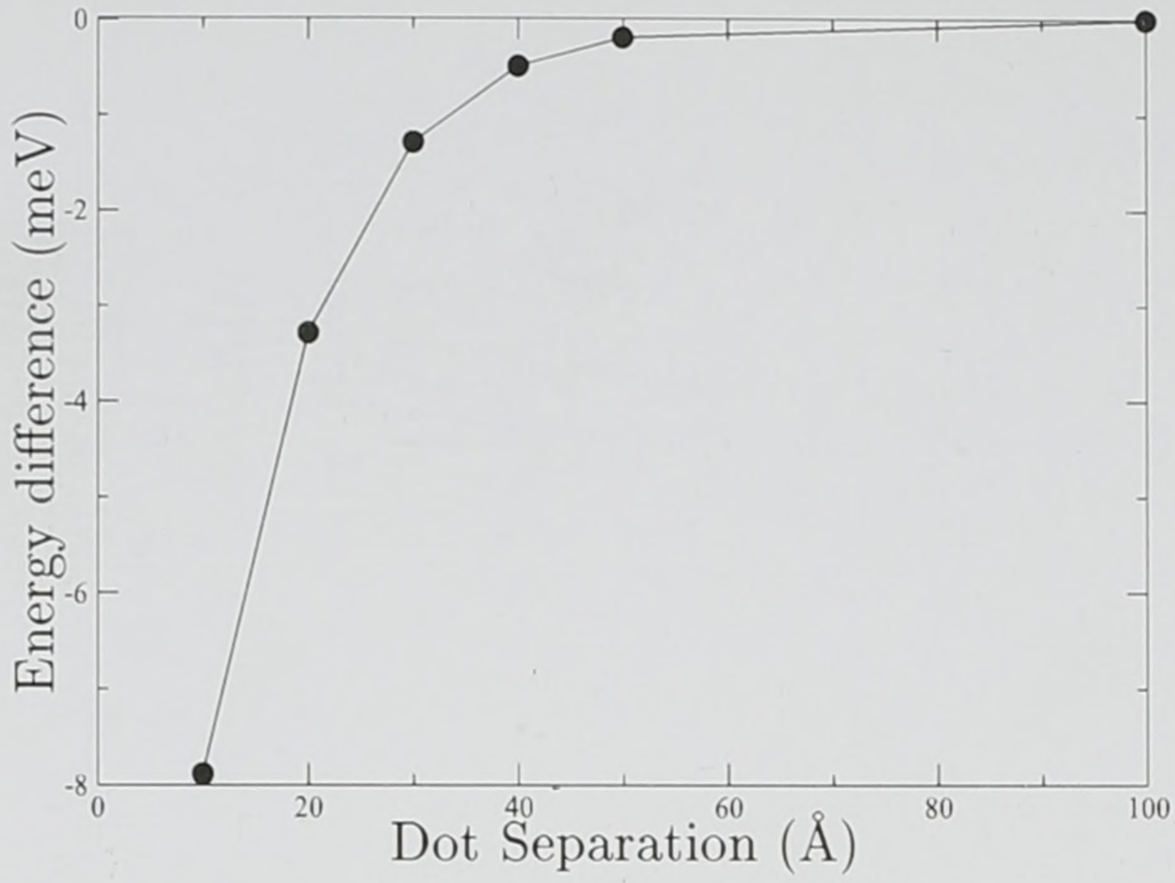

Figure 4.16: Difference in energy $E^{2dots} - E^{1dot}$ vs. dot separation

correspond to the bottom edge of the box, the middle and the upper edge of the box. As can be clearly seen, the bottom slice is dominated by the initial condition at the corner, while the middle slice shows a clearly defined wave function, since this slice is passing directly through the lower pyramidal dot. The top slice exhibits a maximum at the centre of the plane which is considerably smaller in magnitude and spatially wider than that of the middle slice. This is due to the fact that the top slice is at the edge of the box and hence the wave function is decaying and the it is at some distance from the quantum dots and hence less localised.

Figure 4.19 shows the wave function of the first excited state, or anti bonding state, for two values of inter-dot separation. As can be clearly seen the wave function consists of a positive peak over the smaller dot and a negative trough over the larger dot.

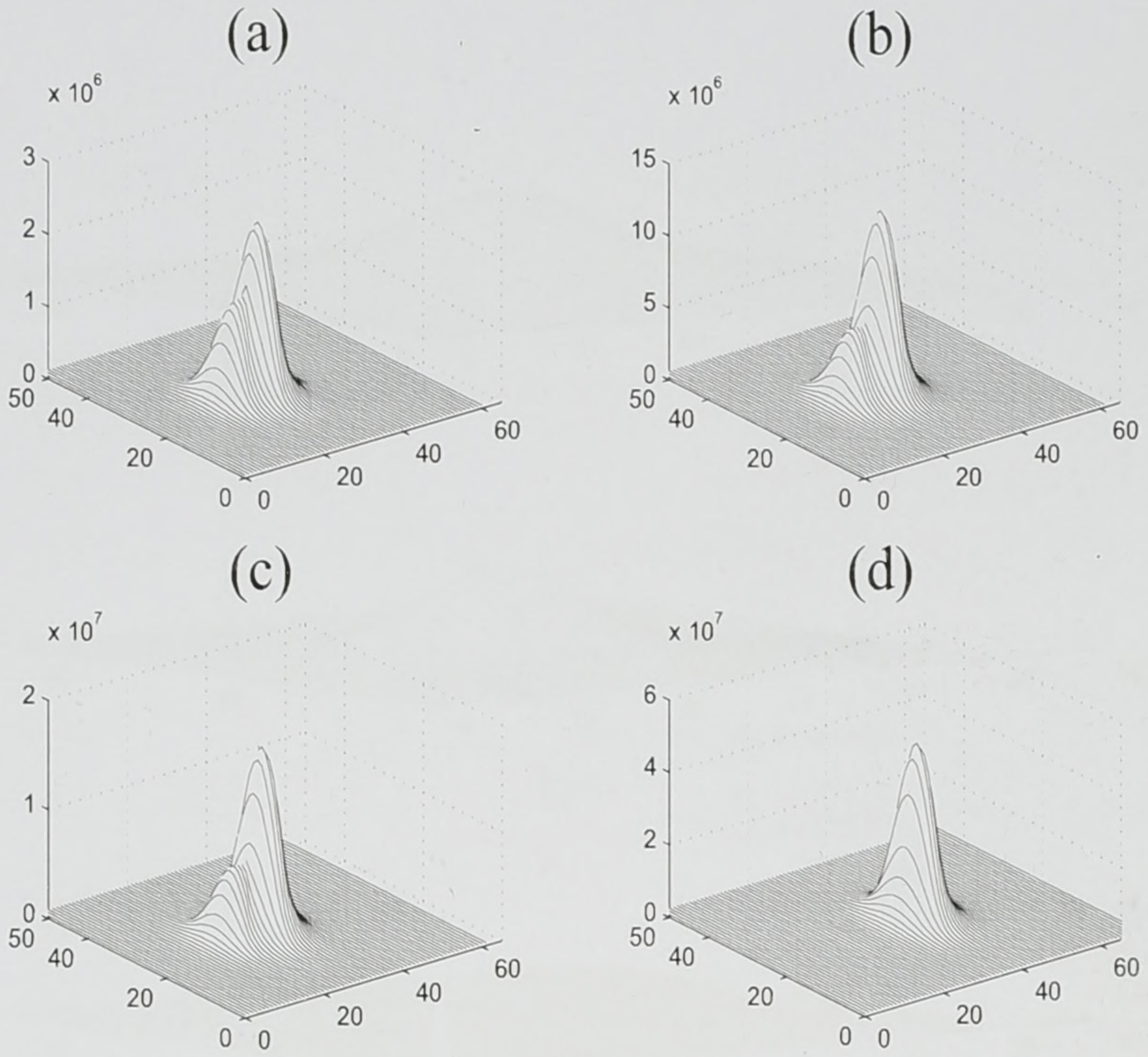

Figure 4.17: Normalised ground state, or bonding state, vertical slices of the wave function for box with two pyramidal dots with zero potential, horizontal coordinates represent position on the $x-z$ plane and at $y = 255.15$ Å. (a) Box size $520\times520\times600$ Å, separation of 10 Å and Energy = 139.70 meV. (b)Box size $520 \times 520 \times 610$ Å, separation 20 Å and Energy = 144.30 meV. (c) Box size $520\times520\times630$ Å, separation 40 Å and Energy = 147.10 meV. (d) Box size $520 \times 520 \times 690$ Å, separation 100 Å and Energy = 147.59 meV.

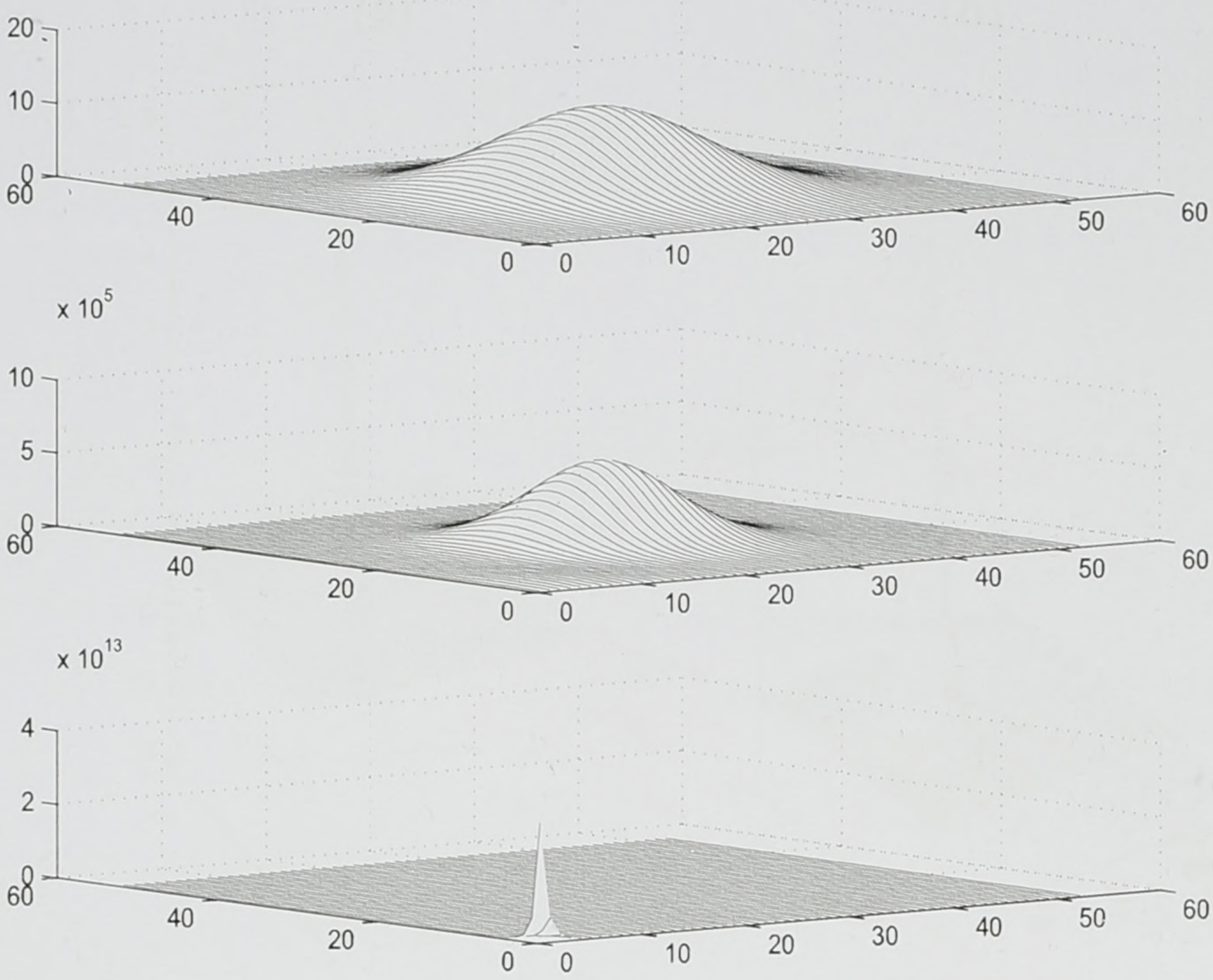

Figure 4.18: Normalised ground state horizontal slices of the wave function for a 520×690 Å box with two pyramidal dots at a separation of 100 Å with zero potential, horizontal coordinates represent position on the $x-y$ plane. Bottom slice is at $z = 9.45$ Å. Middle plot at $z = 292.95$ Å. Top plot at $z = 680.4$ Å. Energy = 147.59 meV

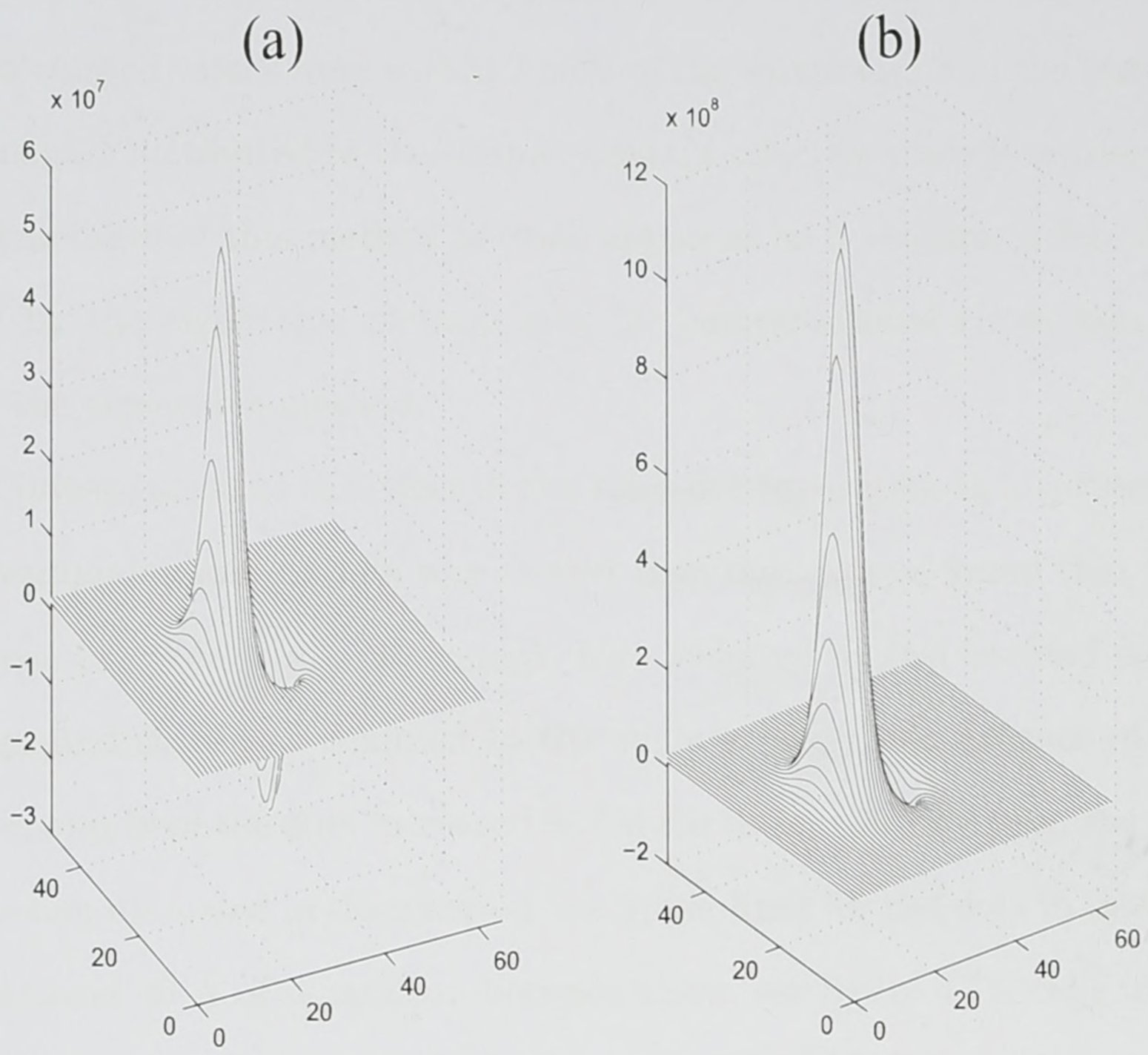

Figure 4.19: Normalised first excited state, or anti bonding state, vertical slices of the wave function for box with two pyramidal dots with zero potential, horizontal coordinates represent position on the $x - z$ plane and at $y = 255.15$ Å. (a) Box size $520 \times 520 \times 610$ Å, separation of 20 Å and Energy = 176.20 meV. (b)Box size $520 \times 520 \times 640$ Å, separation 50 Å and Energy = 172.61 meV.

4.5 Conclusion

In this chapter the finite difference method was extended to three dimensions and was employed to calculate the eigenenergies of an infinitely deep quantum box to demonstrate its validity. It was found that the calculated value was within 3 meV of the analytical value [27].

The more complex case of a pyramidal quantum dot was then investigated. It was found that the calculated values were within 2 meV of the values found in the literature [5]. The difference is again attributed to the simple constant effective mass Hamiltonian used. However, the advantages of this method become apparent as it requires a fraction of the memory needed by the eigenvalue method and the computational times also compare favourably with the eigenvalue method.

A numerical investigation of the effect of the inter-dot separation in a system of vertically aligned pyramidal quantum dots was carried then out. It was found that when the separation between the dots was large enough, they behaved as two isolated dots in the sense that the ground state was confined to the slightly larger dot because of its lower energy. As the proximity of the dots increased so did the interaction between the dots. For the particular system discussed in this chapter the upper limit for the dots to interact with each other was around 40 Å of separation between them, see figure 4.16. The interaction manifests itself as an increase in the peak value of the wave function of the higher energy dot and a reduction in the overall eigenenergies.

Chapter 5

Self-consistent Poisson-Schrödinger Solution

5.1 Poisson's equation

As mentioned before, there has been a growing interest in quantum computation where atomic levels and electron spins play the role of qubits [68]. These qubits usually consist of a pair of coupled quantum dots [13,69]. Thus, from a theoretical point of view it is highly desirable to have a method not only for predicting the eigenenergies of the individual QDs, but also the eigenenergy of the system as a whole. It follows that calculating the eigenstates of a QD is not enough, but it is necessary to investigate the behaviour of QDs when a number of electrons are added to the system so as to simulate their behaviour when the eigenstates are occupied by charge carriers.

The Poisson equation, which can be used to relate the potential to the charge distribution, can be used to calculate the potential generated by these electrons. This potential can then be included into the Schrödinger equation, with the aim of obtaining a self-consistent solution.

5.1.1 Poisson's equation: Derivation

The Poisson equation can be derived from Maxwell's equations [75, 76],

$$\nabla \times \vec{E} = -\frac{\partial \vec{B}}{\partial t} \tag{5.1}$$

$$\nabla \times \vec{H} = \vec{J} + \frac{\partial \vec{D}}{\partial t} \tag{5.2}$$

$$\nabla \cdot \vec{D} = \rho \tag{5.3}$$

$$\nabla \cdot \vec{B} = 0 \tag{5.4}$$

where $\vec{E}$ is the electric field, $\vec{B}$ is the magnetic flux density, $\vec{H}$ is the magnetic intensity, $\vec{D}$ is the electric displacement, $\vec{J}$ is the total conduction current density and ρ is the electric charge density.

Now to derive the equation consider the case of static conditions, i.e. no time variation, equation (5.1) reduces to $\nabla \times \vec{E} = 0$. This is equivalent to the statement that the electric field $\vec{E}$ is the gradient of a scalar function V_ρ, which is the electrostatic potential resulting from the charge distribution ρ. Hence E may be expressed as

$$\vec{E} = -\nabla V_\rho \tag{5.5}$$

Also, the electric displacement $\vec{D}$ is proportional to $\vec{E}$ and can be expressed as

$$\vec{D} = \epsilon \vec{E} \tag{5.6}$$

where ϵ is the permittivity of the material. Substituting into equation (5.3) yields the Poisson equation

$$\nabla^2 V_\rho = -\frac{\rho}{\epsilon} \tag{5.7}$$

A solution is usually arrived at through the use of the electric field, since

$$V_\rho(\mathbf{r}) = -\int_{-\infty}^{\mathbf{r}} \vec{E} \cdot d\mathbf{r} \tag{5.8}$$

In the one dimensional case, i.e. quantum well, the charge density may be thought of as an infinite sheet of charge thickness δz [27]. In the two dimensional case, i.e. quantum wire, the charge distribution may be thought of as an infinitely long strip of thickness δz and height δy. Finally, in the three dimensional case of a quantum dot, the charge distribution may be thought of as a finite volume which is dependent on the geometry of the dot. However, in the present case the Possion equation will be solved using a finite difference method so that it may be easily linked to the Schrödinger equation which is solved using the same method.

5.1.2 Finite difference expansion

The way to include the Poisson equation into the finite difference method, is to discretise the equation. This can be done by expanding equation (5.7) in terms of finite differences. This expansion is accomplished in a similar manner to that of the Schrödinger equation. Considering the three dimensional case, the second order partial derivative of the potential, V_ρ, is given by

$$\frac{\partial^2 V_\rho(x,y,z)}{\partial x^2} \approx \frac{V_\rho(x+\delta x,y,z) - 2V_\rho(x,y,z) + V_\rho(x-\delta x,y,z)}{(\delta x)^2} \tag{5.9}$$

$$\frac{\partial^2 V_\rho(x,y,z)}{\partial y^2} \approx \frac{V_\rho(x,y+\delta y,z) - 2V_\rho(x,y,z) + V_\rho(x,y-\delta y,z)}{(\delta y)^2} \tag{5.10}$$

$$\frac{\partial^2 V_\rho(x,y,z)}{\partial z^2} \approx \frac{V_\rho(x,y,z+\delta z) - 2V_\rho(x,y,z) + V_\rho(x,y,z-\delta z)}{(\delta z)^2} \tag{5.11}$$

Substituting into the Poisson equation, while ensuring the the step values $\delta x, \delta y$ and δz are small enough so that the approximation is valid, yields

$$\frac{V_\rho(x+\delta x,y,z)-2V_\rho(x,y,z)+V_\rho(x-\delta x,y,z)}{(\delta x)^2}$$
$$+\frac{V_\rho(x,y+\delta y,z)-2V_\rho(x,y,z)+V_\rho(x,y-\delta y,z)}{(\delta y)^2}$$
$$+\frac{V_\rho(x,y,z+\delta z)-2V_\rho(x,y,z)+V_\rho(x,y,z-\delta z)}{(\delta z)^2}$$
$$\approx -\frac{\rho(x,y,z)}{\epsilon} \quad (5.12)$$

Setting $\delta x = \delta z = \delta y$ it can be shown that equation (5.12) reduces to

$$V_\rho(x+\delta x,y,z)+V_\rho(x-\delta x,y,z)+V_\rho(x,y+\delta y,z)+V_\rho(x,y-\delta y,z)$$
$$+V_\rho(x,y,z+\delta z)+V_\rho(x,y,z-\delta z)-6V_\rho(x,y,z)=-(\delta y)^2\frac{\rho(x,y,z)}{\epsilon} \quad (5.13)$$

It is important to note that the charge distribution, ρ, is in fact a function of position. The charge distribution which is essentially the charge per unit volume, can be expressed in terms of the eigenstate wave function. This is possible since the Poisson and Schrödinger equations are to be solved self-consistently, and it is known from basic quantum mechanics that the square of a normalised eigenstate wave function is in actuality the probability of a charge carrier existing at a specific point in space. This means that if a solution to the Schrödinger equation is calculated, the resultant normalised eigenstate wave function can be squared and then multiplied by the total charge present to give the charge distribution at all points of the grid. Mathematically this can be expressed as

$$\rho(x,y,z) = n_e e^- \left|\psi_{norm}(x,y,z)\right|^2 \quad (5.14)$$

where ψ_{norm} is the normalised wave function, n_e is the total number of electrons in the system and e^- is the charge of a single electron.

5.1.3 Matrix equation

As with the Schrödinger equation, the solution depends on the ability to formulate the set of equations generated by equation (5.13) as a single matrix equation. In order to arrive at the matrix equation consider the simple case of a quantum box of dimensions L_x, L_y and L_z. The box can discretized in such a way that, by choosing appropriate scales, the dimensions of the box can be represented by a total of n_1+2 elements for the y dimension, n_2+2 for the z dimension and n_3+2 for the x dimension. Thus equation (5.13) can be further simplified to give

$$V_{\rho i,j,l+1} + V_{\rho i,j,l-1} + V_{\rho i,j-1,l} + V_{\rho i,j+1,l} + V_{\rho i+1,j,l} + V_{\rho i-1,j,l} - 6V_{\rho i,j,l} = -(\delta y)^2 \frac{\rho_{i,j,l}}{\epsilon} \quad (5.15)$$

where i, j, l are the array indices of the Poisson potential points. It can be shown that the set of simultaneous equations generated by equation (5.15) can be expressed as a single matrix equation of the form

$$\mathbf{P} \cdot \mathbf{V} = \mathbf{T} \quad (5.16)$$

where $\mathbf{P}$ is a two dimensional array of Poisson potential coefficients, $\mathbf{V}$ is a column vector of Poisson potential points and $\mathbf{T}$ is a column vector of source terms generated by the charge distribution.

Dirichlet boundary conditions are applied to all solutions of the Poisson equation and have the form,

$$V_\rho(x, y, z) \to 0 \text{ as } x, y \text{ or } z \to 0 \quad (5.17)$$

$$V_\rho(x, y, z) \to 0 \text{ as } x, y \text{ or } z \to L_x, L_y \text{ or } L_z \quad (5.18)$$

The forms of the matrices can be derived in a similar manner to that of the case of the Schrödinger equation. It can be shown that the matrix $\mathbf{P}$ is an $n \times n$ sparse matrix, where $n = [n_1 \times n_2 \times n_3]$. The best way to represent this matrix is by using sub-matrices. In the present case the matrix contains n_1 sub-matrices such that the total matrix has the

form

$$\mathbf{P} = \overbrace{\begin{pmatrix} \mathbf{\Lambda} & \mathbf{D} & \mathbf{0} & \cdots & \cdots & \mathbf{0} \\ \mathbf{D} & \mathbf{\Lambda} & \mathbf{D} & \mathbf{0} & \cdots & \mathbf{0} \\ \mathbf{0} & \mathbf{D} & \mathbf{\Lambda} & \mathbf{D} & \ddots & \vdots \\ \vdots & \ddots & \ddots & \ddots & \ddots & \mathbf{0} \\ \mathbf{0} & \cdots & \mathbf{0} & \mathbf{D} & \mathbf{\Lambda} & \mathbf{D} \\ \mathbf{0} & \cdots & \cdots & \mathbf{0} & \mathbf{D} & \mathbf{\Lambda} \end{pmatrix}}^{n_1 \text{ blocks}} \tag{5.19}$$

where, the sub-matrix $\mathbf{\Lambda}$ is a $([n_2 \times n_3] \times [n_2 \times n_3])$ tridiagonal matrix which is itself comprised of n_2 sub-matrices and has the form

$$\mathbf{\Lambda} = \overbrace{\begin{pmatrix} \gamma & \mathbf{I} & \mathbf{0} & \cdots & \cdots & \mathbf{0} \\ \mathbf{I} & \gamma & \mathbf{I} & \mathbf{0} & \cdots & \mathbf{0} \\ \mathbf{0} & \mathbf{I} & \gamma & \mathbf{I} & \ddots & \vdots \\ \vdots & \ddots & \ddots & \ddots & \ddots & \mathbf{0} \\ \mathbf{0} & \cdots & \mathbf{0} & \mathbf{I} & \gamma & \mathbf{I} \\ \mathbf{0} & \cdots & \cdots & \mathbf{0} & \mathbf{I} & \gamma \end{pmatrix}}^{n_2 \text{ blocks}} \tag{5.20}$$

The sub-matrix γ is a $(n_3 \times n_3)$ matrix and has the form

$$\gamma = \begin{pmatrix} -6 & 1 & 0 & \cdots & 0 \\ 1 & -6 & 1 & \ddots & \vdots \\ 0 & \ddots & \ddots & \ddots & 0 \\ \vdots & \ddots & 1 & -6 & 1 \\ 0 & \cdots & 0 & 1 & -6 \end{pmatrix} \tag{5.21}$$

The sub-matrix $\mathbf{D}$ is a $([n_2 \times n_3] \times [n_2 \times n_3])$ diagonal matrix which in itself is comprised of n_2 sub-matrices and has the form

$$\mathbf{D} = \overbrace{\begin{pmatrix} \mathbf{I} & \mathbf{0} & \cdots & \cdots & \mathbf{0} \\ \mathbf{0} & \mathbf{I} & \mathbf{0} & \cdots & \mathbf{0} \\ \mathbf{0} & \ddots & \ddots & \ddots & \vdots \\ \vdots & \ddots & \mathbf{0} & \mathbf{I} & \mathbf{0} \\ \mathbf{0} & \cdots & \cdots & \mathbf{0} & \mathbf{I} \end{pmatrix}}^{n_2 \text{ blocks}} \tag{5.22}$$

The sub-matrices $\mathbf{I}$ are just $(n_3 \times n_3)$ standard identity matrices.

The column vector $\mathbf{V}$ consists of $n = [n_1 \times n_2 \times n_3]$ elements and is given by equation (5.23). It consists of a total of n_1 blocks each of length $n_2 \times n_3$ elements.

$$\mathbf{V} = \begin{pmatrix} V_{\rho 1,1,1} \\ V_{\rho 1,1,2} \\ V_{\rho 1,1,3} \\ \vdots \\ V_{\rho 1,1,n_3} \\ V_{\rho 1,2,1} \\ \vdots \\ V_{\rho 1,n_2,n_3} \\ V_{\rho 2,1,1} \\ \vdots \\ V_{\rho n_1,n_2,n_3} \end{pmatrix} \tag{5.23}$$

Finally, the column vector $\mathbf{T}$ is of length n and is of the form

$$\mathbf{T} = \begin{pmatrix} \alpha_{1,1,1} \\ \alpha_{1,1,2} \\ \vdots \\ \alpha_{1,n_2,n_3} \\ \alpha_{2,1,1} \\ \vdots \\ \alpha_{i,j,l} \\ \vdots \\ \alpha_{n_1,n_2,n_3} \end{pmatrix} \tag{5.24}$$

where $\alpha_{i,j,l}$ is given by

$$\alpha_{i,j,l} = -(\delta y)^2 n_e e^{-\frac{|\psi_{norm}(i,j,l)|^2}{\epsilon}} \tag{5.25}$$

As an initial test to ensure that this approach is valid, the Poisson potential was calculated for a point charge. This was accomplished by setting up a normalised pseudo wave function, which consisted of a single value at the centre of the mesh. In this way a point charge was approximated, since the probability represented by this pseudo wave function had a value of unity at a single point at the centre of the mesh, and was zero elsewhere. This pseudo wave function was then plugged into the Poisson solver and the value of the electrostatic potential calculated for a mesh spacing of 9.45 Å and a mesh size of $55 \times 55 \times 55$ elements. It was found that the resulting electrostatic potential conformed to the expected behaviour dictated by Coulomb's Law, where the potential was inversely proportional to r^2, i.e. $V_\rho \propto \frac{1}{r^2}$, where r is the distance from the point charge. A slice through the middle of the surface describing this Poisson electrostatic potential is displayed in figure 5.1 and exhibits this predicted behaviour.

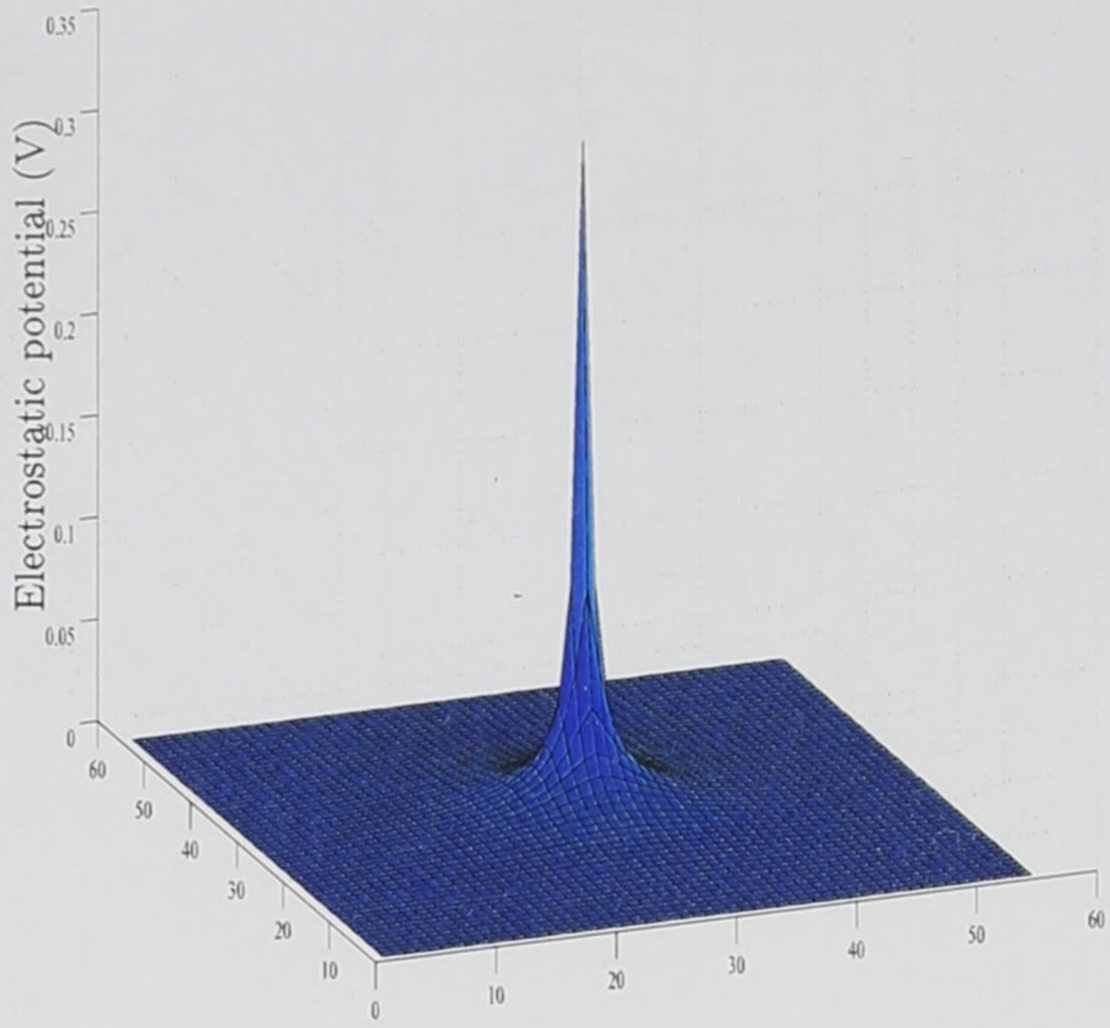

Figure 5.1: Slice, at $z = 255.15$ Å, of the calculated Poisson electrostatic potential for a point charge. Horizontal coordinates represent position on the $x - y$ plane.

5.2 Self-consistent Poisson-Schrödinger

This section presents an overview of the steps employed for solving the Poisson and Schrödinger equations self-consistently.

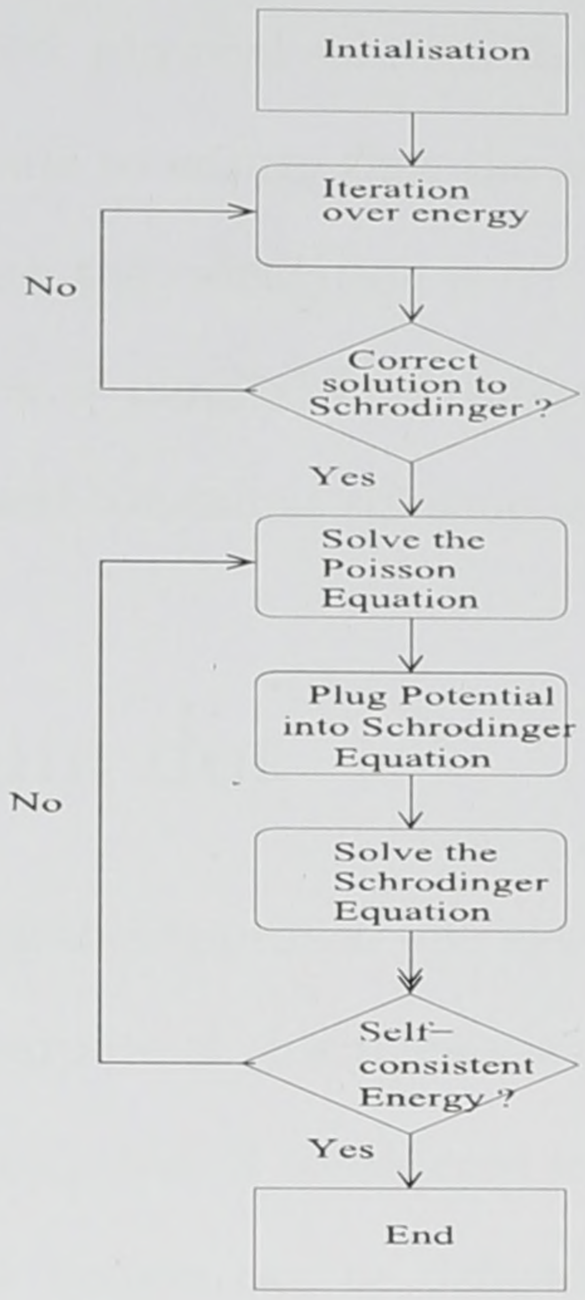

Figure 5.2: Algorithm for the implementation of the self consistent solution to the Poisson and Schrödinger equations

Having deduced the form of the matrices generated by the finite difference expansion of the Poisson equation, it can be solved using the same algorithm used for the Schrödinger equation. The next step is to successfully incorporate solution to the Possion equation into the Schrödinger solver, with the aim of obtaining self-consistent solutions. The steps employed in obtaining a self-consistent solution are outlined in the form of a flow chart displayed in figure 5.2. First of all the initialisation process is comprised of defining the different parameters and constants ($\hbar$, m^*, V etc.) and the initial setting up of the matrices (**A** and **S**). The second step is the main iteration over energy, where the energy is incremented, and the main diagonal of **A** is updated with the value of the energy. The Schrödinger equation is then solved and the correct physical solution identified. The next step is using the resultant wave function to calculate the charge distribution and the relevant matrices are set up and the Poisson equation is solved. The resulting Poisson potential is then plugged back into the Schrödinger solver, i.e. the main diagonal of **A**

is updated once again. The correct physical solution to the Schrödinger equation is then identified and a check is then made to ensure that the energy is self-consistent, a change less than some tolerance, if so then the calculation is terminated. If the energy is not self-consistent then the wave function is plugged back into the Poisson solver and the same procedure is carried out until a self-consistent solution is found.

5.3 Single quantum dot

The first system investigated using this approach was identical to that of section 4.3, and is displayed in figure 4.6. For the purpose of this theoretical investigation a very low doping density is assumed and the entire system is considered to be neutral. In this manner, the exact number of electrons in the system can be defined. Thus the Poisson potential is calculated for a specified number of electrons.

5.3.1 Results

The self-consistent solution of the Poisson-Schrödinger equations was calculated for the system under investigation, for the case of $1 \rightarrow 4$ electrons. The mesh used for all the calculations in this investigation was $55 \times 55 \times 55$ elements, which corresponds to a mesh spacing of 9.45 Å and was chosen for convergence purposes, see figure 4.11. The resultant energies are interpreted as follows; the ground state energy calculated in the absence of electrons, see figure 5.3, is the energy required to add an electron to the system, in other words the energy required to introduce an electron into an "empty" quantum dot. The energy obtained for the case of a single electron is the energy required to add a second electron to a quantum dot which already contains an electron and so on.

Figure 5.3 shows a slice of the ground state wave function for the system in the absence of electrons. This is the wave function used to calculate the initial charge distribution for the case of a single electron.

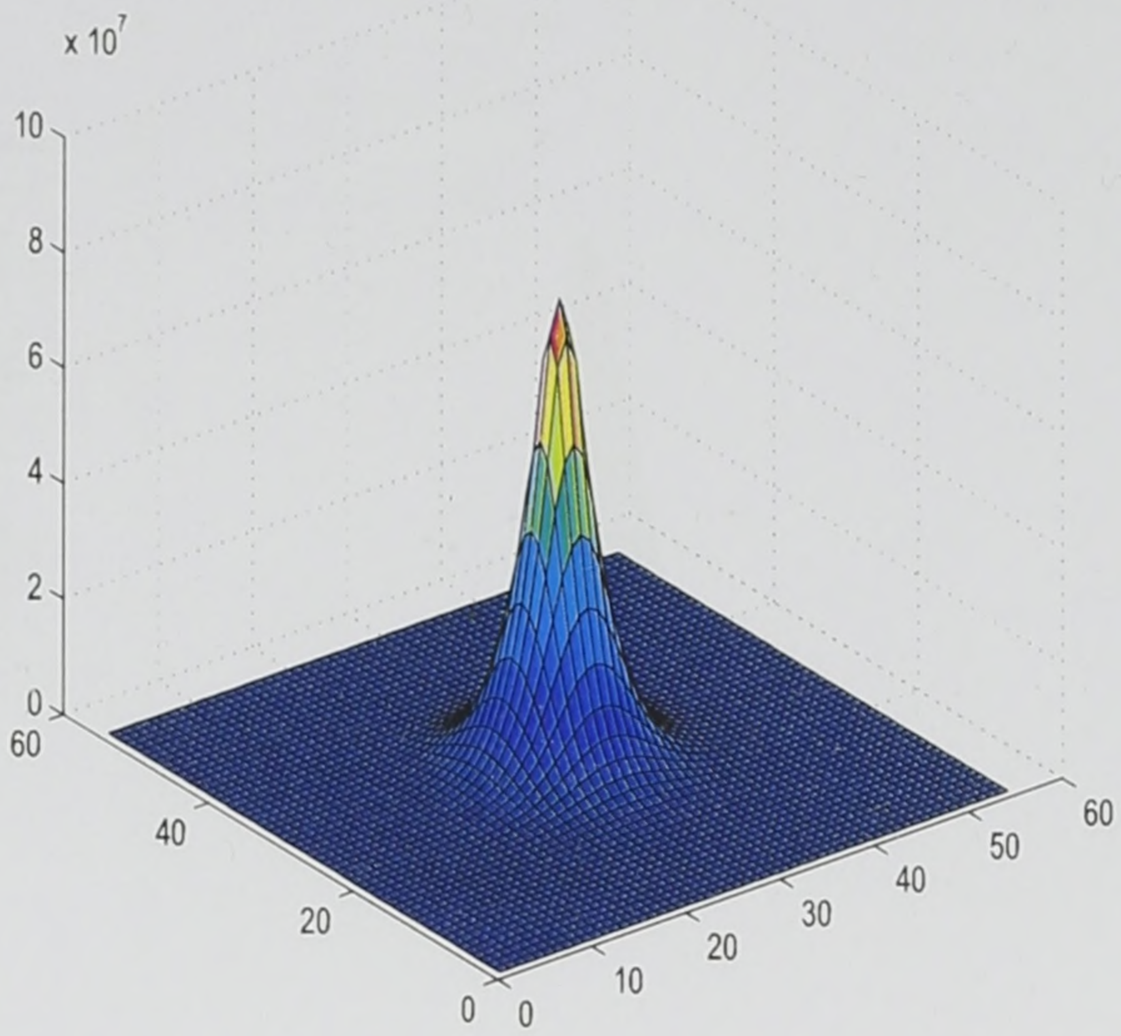

Figure 5.3: Slice, at $z = 255.15$ Å, of the normalised ground state wave function in the absence of electrons, i.e. empty, of a pyramidal dot of height= 60 Å and base width = 120 Å. Horizontal coordinates represent position on the $x - y$ plane of the QD. Energy= 172.35 meV.

Figure 5.4 shows a slice of the Poisson potential resulting from the charge distribution calculated using the wave function of figure 5.3 and in the presence of a single electron. As would be expected the Poisson potential has the general shape of the wave function, indicating that the largest value for this potential occurs at the centre of the QD corresponding to the region where the probability of finding the electron is at a maximum.

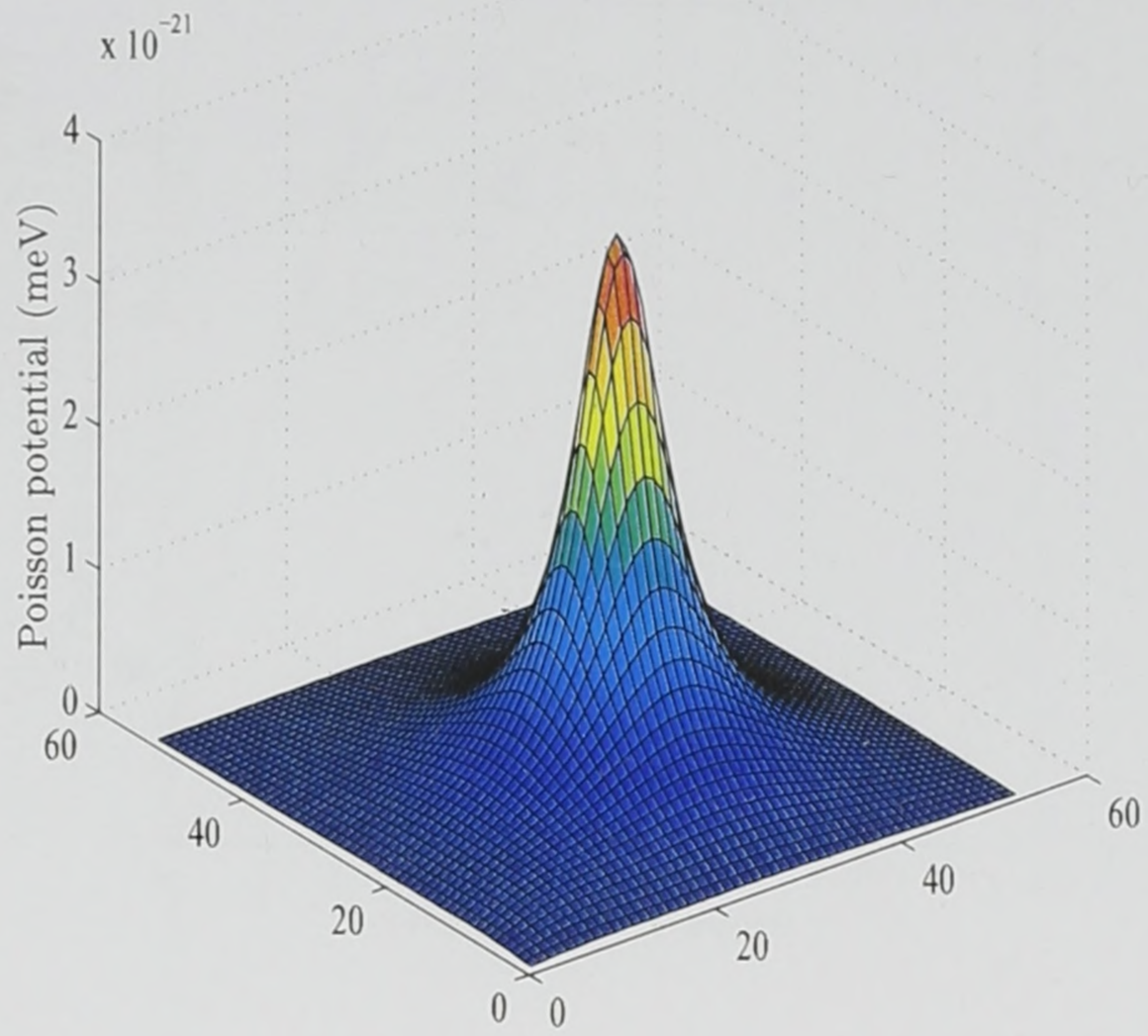

Figure 5.4: Slice, at $z = 255.15$ Å, of the Poisson electrostatic potential resulting from one electron. Horizontal coordinates represent position on the $x - y$ plane of the QD.

Figure 5.5 is a plot of the eigenenergy versus the number of iterations for the case of a single electron. As can clearly be seen the eigenenergy converges to the self-consistent value almost immediately. This fact is also evident when the initial wave function of figure 5.3 is compared with the final self-consistent wave function displayed in figure 5.6, since they are practically identical.

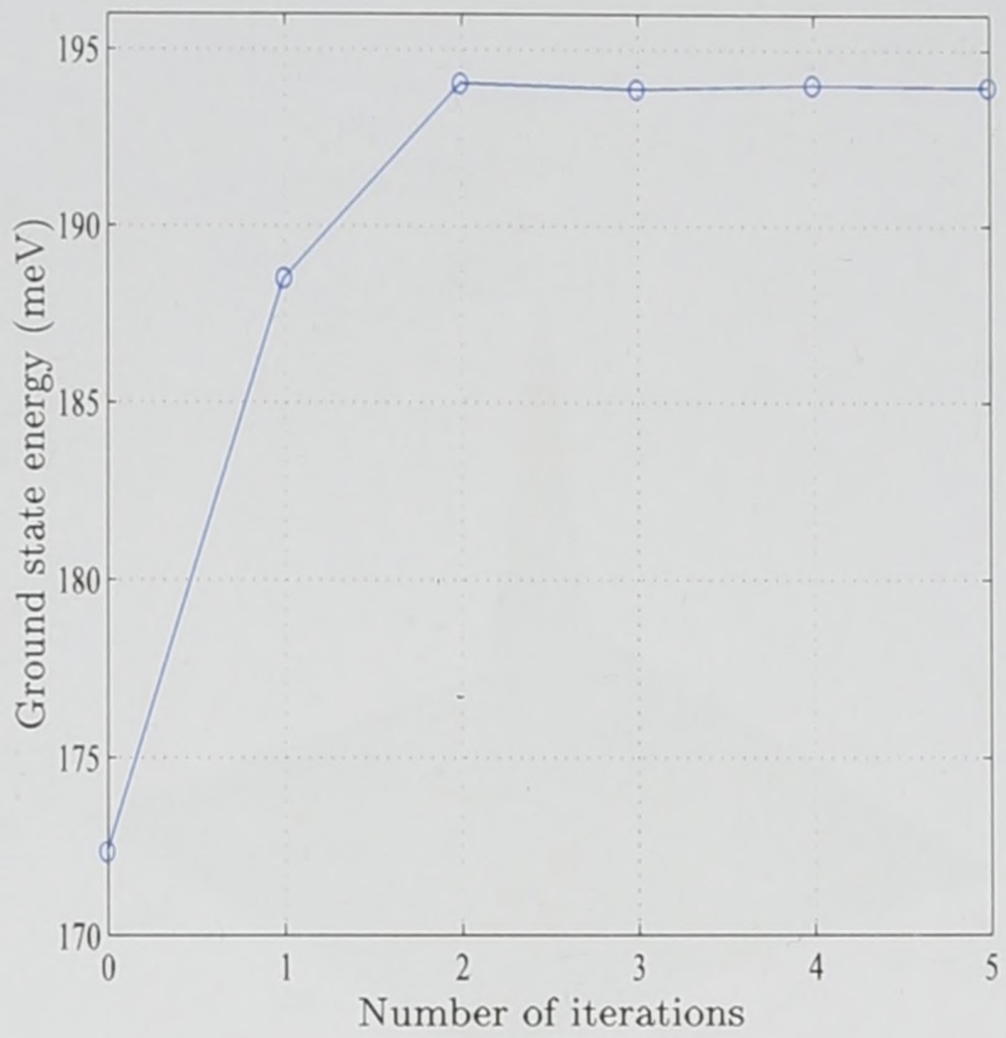

Figure 5.5: Ground state energy versus number of iterations for single quantum dot in the case of one electron (corresponding to the potential in figure 5.4)

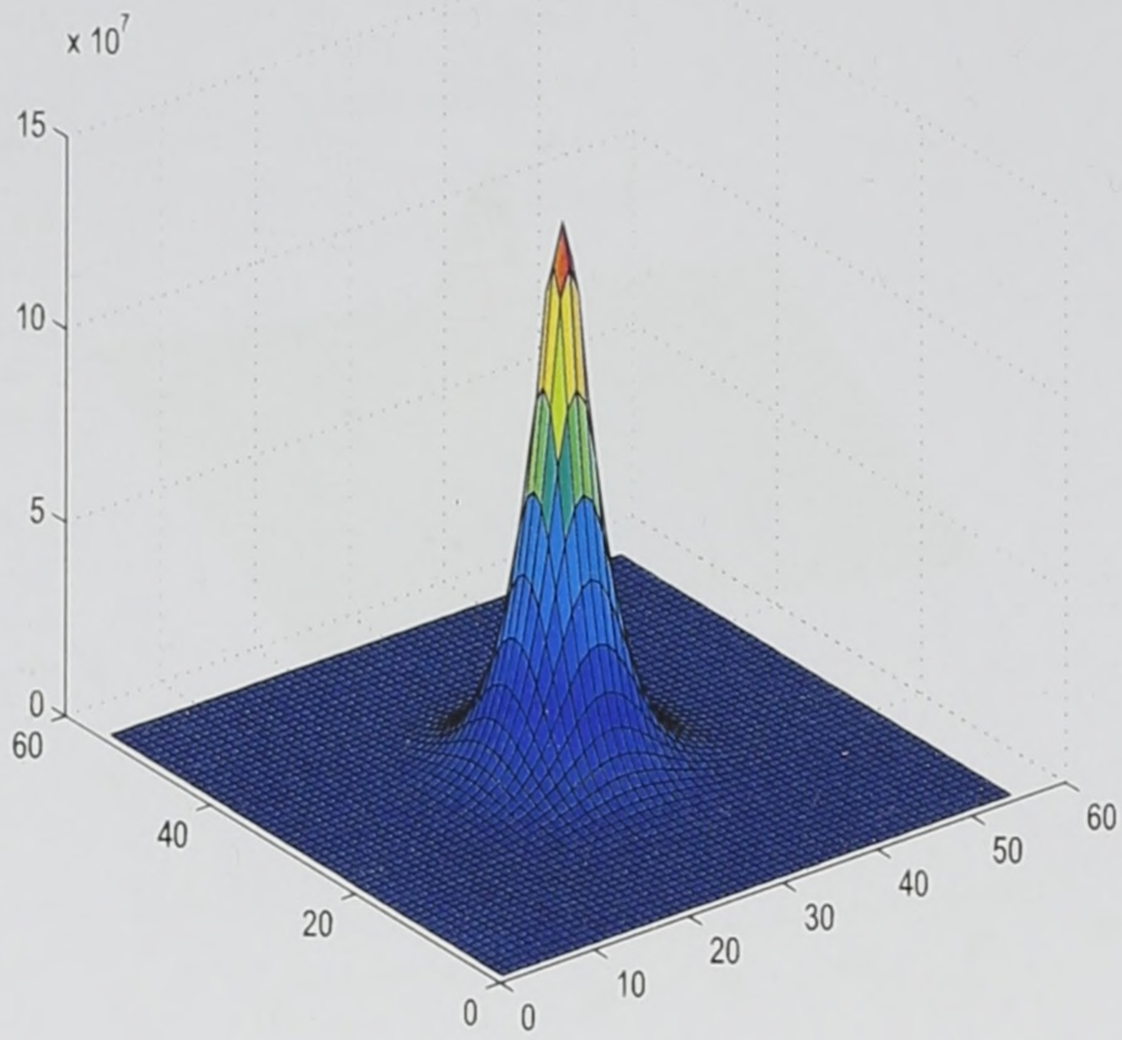

Figure 5.6: Slice, at $z = 255.15$ Å, of the normalised ground state self-consistent wave for the case of a single electron for a pyramidal dot of height= 60 Å and base width = 120 Å. Horizontal coordinates represent position on the $x - y$ plane of the QD. Energy= 193.96 meV.

As mentioned before, the eigenenergy calculated for the case of a single electron is in fact the energy required to add an electron to a quantum dot which already contains an electron. And since the Pauli exclusion principle [27] dictates that only two electrons may occupy the ground state it is necessary to move to the first excited state in order to the calculate the eigenenergies for the case of multiple electrons. Figure 5.7 shows a slice of the empty first excited state wave function, i.e no electrons, which is used to calculate the initial charge distribution in the case of multiple electrons.

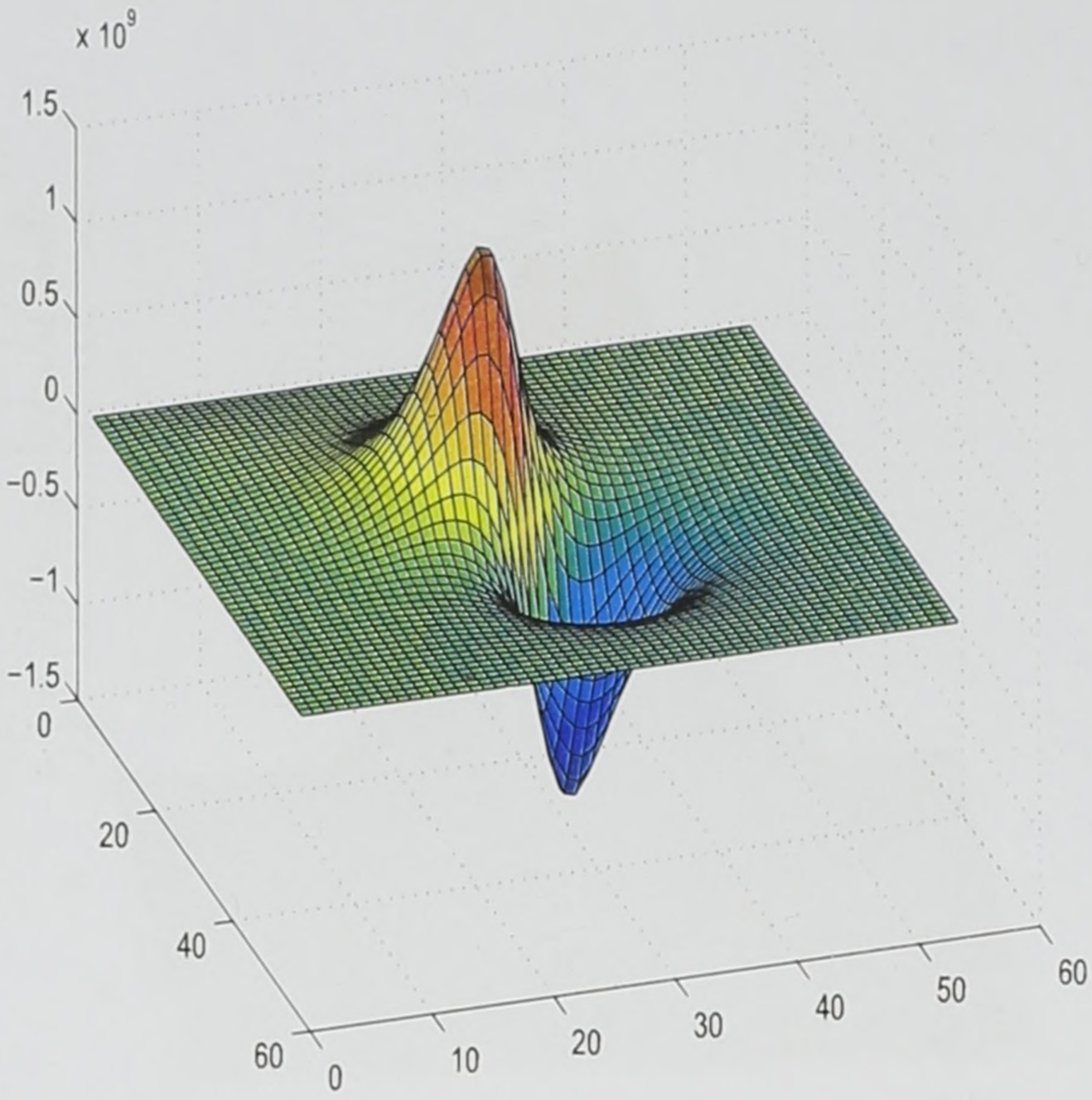

Figure 5.7: Slice, at $z = 255.15$ Å, of the normalised first excited state wave function for the case of an empty pyramidal dot of height= 60 Å and base width = 120 Å. Horizontal coordinates represent position on the $x - y$ plane of the QD. Energy= 261.3 meV.

Now consider the example case of 3 electrons. A slice of the initial Poisson potential resulting from using the empty wave function of figure 5.7 to calculate the charge distribution is displayed in figure 5.8.

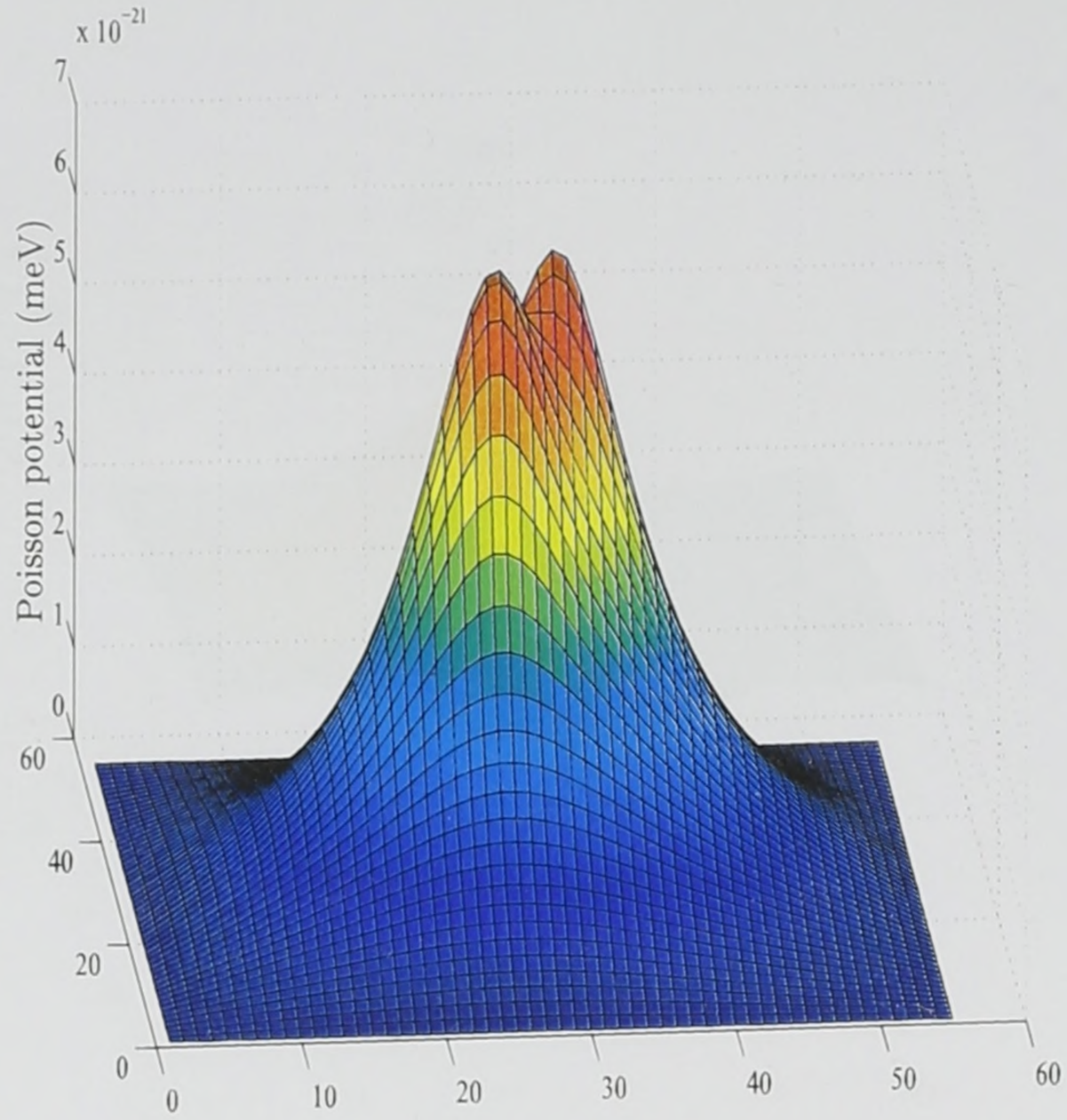

Figure 5.8: Slice, at $z = 255.15$ Å, of the Poisson potential resulting from 3 electrons and used for the first iteration. Horizontal coordinates represent position on the $x-y$ plane of the QD.

The inclusion of this potential into the Poisson-Schrödinger solver, i.e. the first iteration, resulted in the eigenstate described by the wave function of which a slice is shown in figure 5.9. This wave function, unlike those shown previously, does not exhibit strong localisation over the pyramidal region. This wave function describes a "quasi-bound" state. This is due to the fact that the energy of this state, 293.948 meV, is larger than the barrier potential which has a value of 276 meV. In essence, this wave function describes a state where the highest probability of locating the electrons is inside the pyramidal region, but there is also a significant probability of the electrons being located outside the pyramidal region.

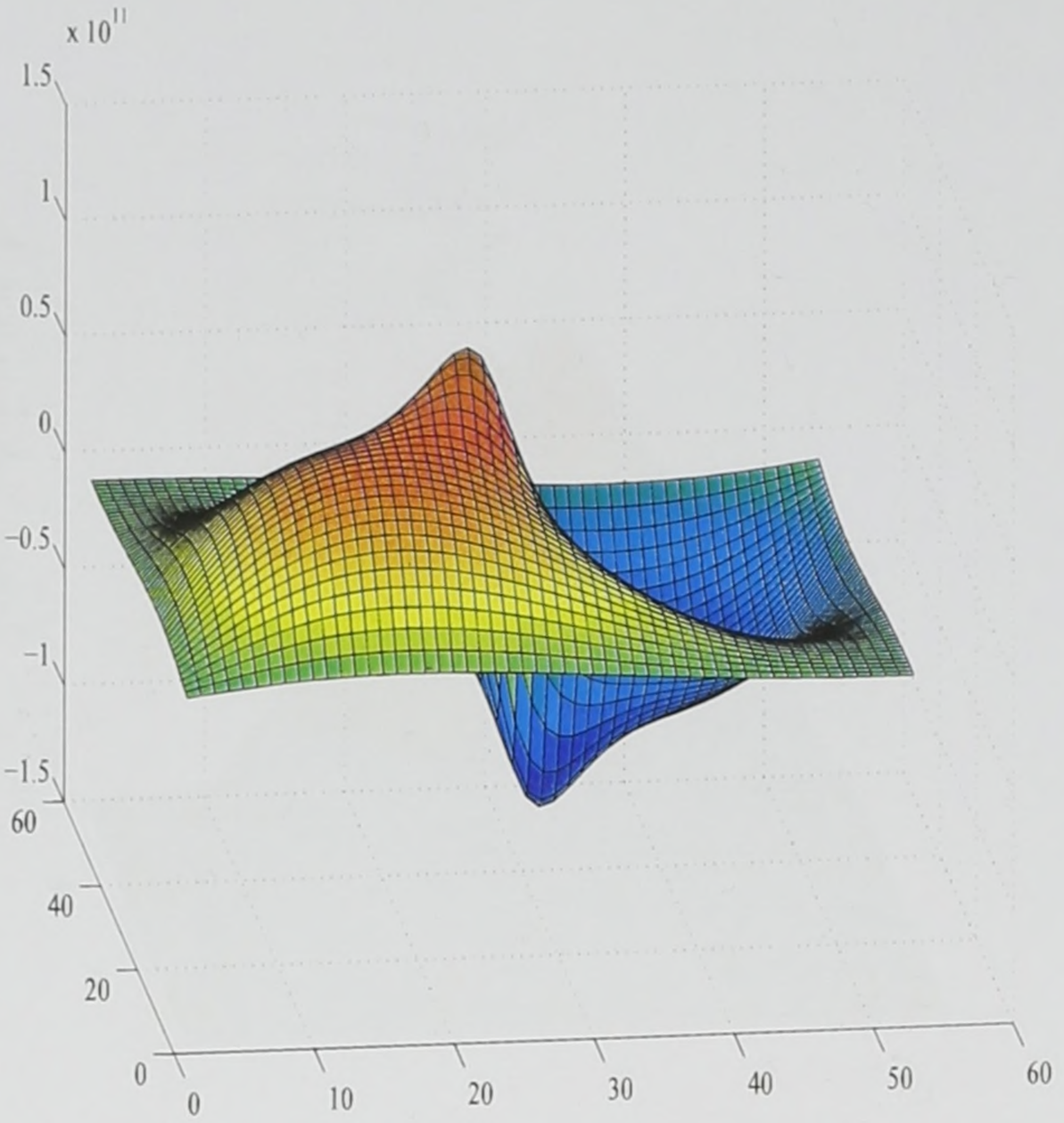

Figure 5.9: Slice, at $z = 255.15$ Å, of the normalised first excited state wave function for the case of 3 electrons for a pyramidal dot of height= 60 Å and base width = 120 Å, calculated by the first iteration of the Poisson-Schrödinger solver. Horizontal coordinates represent position on the $x-y$ plane of the QD. Energy= 293.948 meV.

Using the wave function of figure 5.9 to calculate the updated charge distribution, i.e. the second iteration, results in the Poisson potential displayed in figure 5.10. As can be seen, this updated potential is different in character from the previous potential of figure 5.8, reflecting the differences in the wave functions used to calculate the corresponding charge distributions. The inclusion of this updated potential into the Poisson-Schrödinger solver results in an eigenenergy of 272.828 meV, and a slice of the wave function describing this state is shown in figure 5.11. In contrast, this wave function shows strong localisation over the pyramidal region. This is due to the fact that the eigenenergy is below that of the barrier potential.

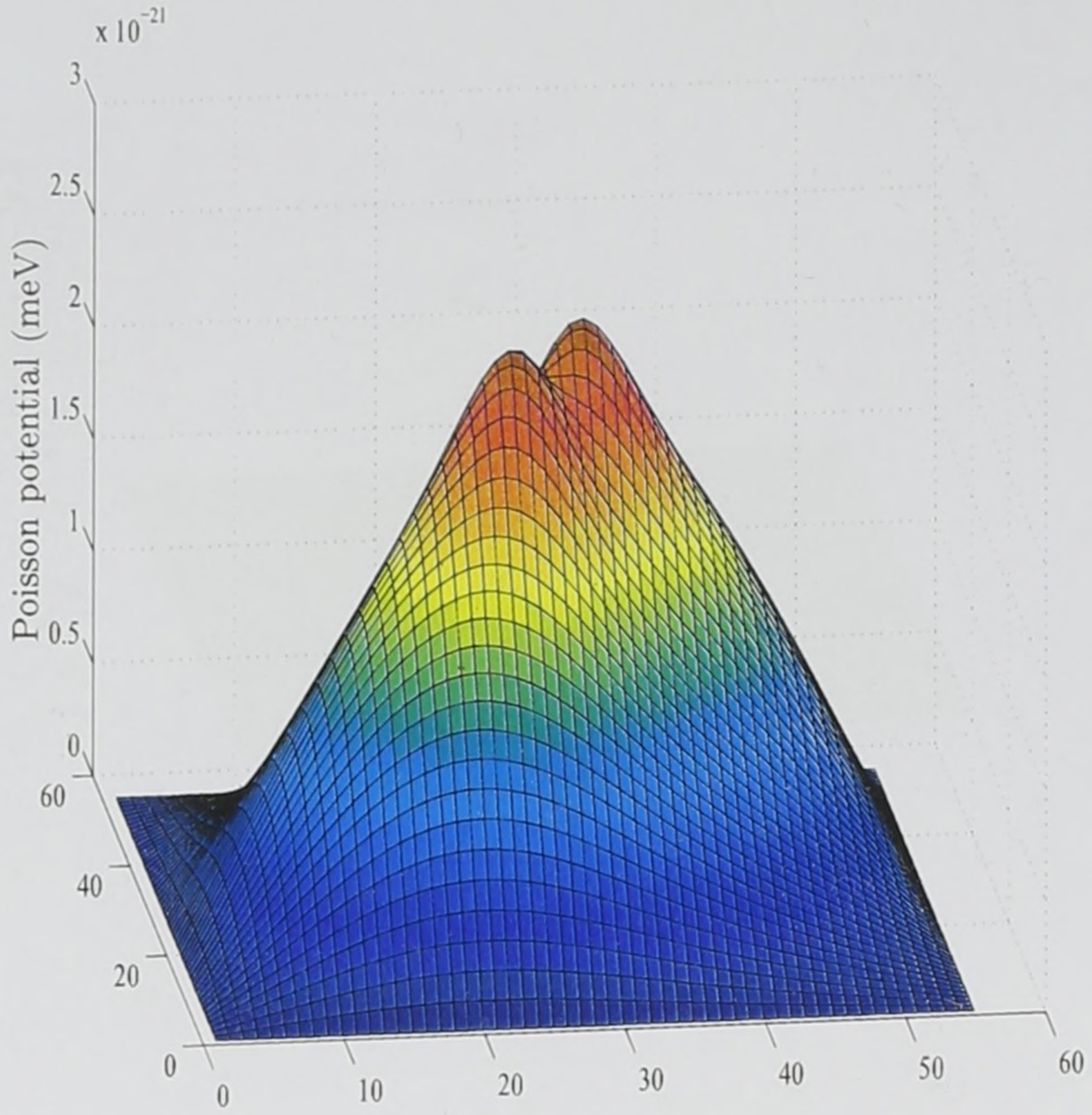

Figure 5.10: Slice, at $z = 255.15$ Å, of the Poisson potential resulting from 3 electrons and used for the second iteration. Horizontal coordinates represent position on the $x - y$ plane of the QD.

Note that the wave function resulting from the second iteration, see figure 5.11, is almost identical in shape to the wave function describing the empty QD, see figure 5.7. It was found that the Poisson potential calculated by using the wave function of figure 5.11 is of the same character as that of the first iteration, see figure 5.8, which in turn yielded a wave function identical in structure to that of figure 5.9. Thus, following the procedure outlined by the flow chart in figure 5.2, it was found that the difference between the eigenenergies of any two consecutive iterations was always around 20 meV. In other words no self-consistent solution was found, but rather the eigenenergy oscillated between two fixed values. Figure 5.12 is a plot of the eigenenergies versus the number if iterations for the case of 3 electrons, and clearly shows this behaviour.

In fact, the potential was alternating between two set values, while the correct value of the potential was actually located between these two fixed points. As a consequence, it was

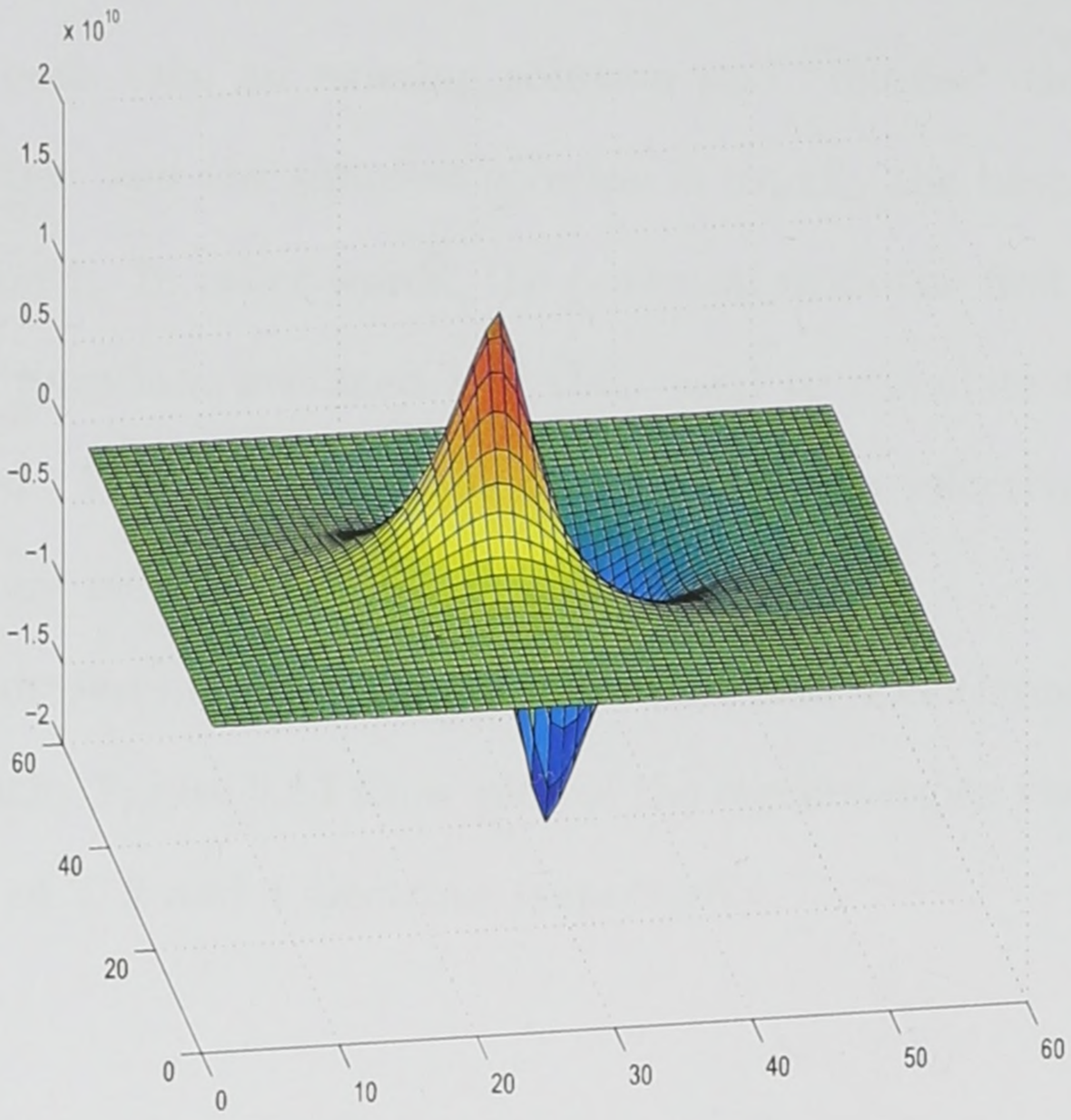

Figure 5.11: Slice, at $z = 255.15$ Å, of the normalised first excited state wave function for the case of 3 electrons for a pyramidal dot of height= 60 Å and base width = 120 Å, calculated by the second iteration of the Poisson-Schrödinger solver. Horizontal coordinates represent position on the $x - y$ plane of the QD. Energy= 272.828 meV.

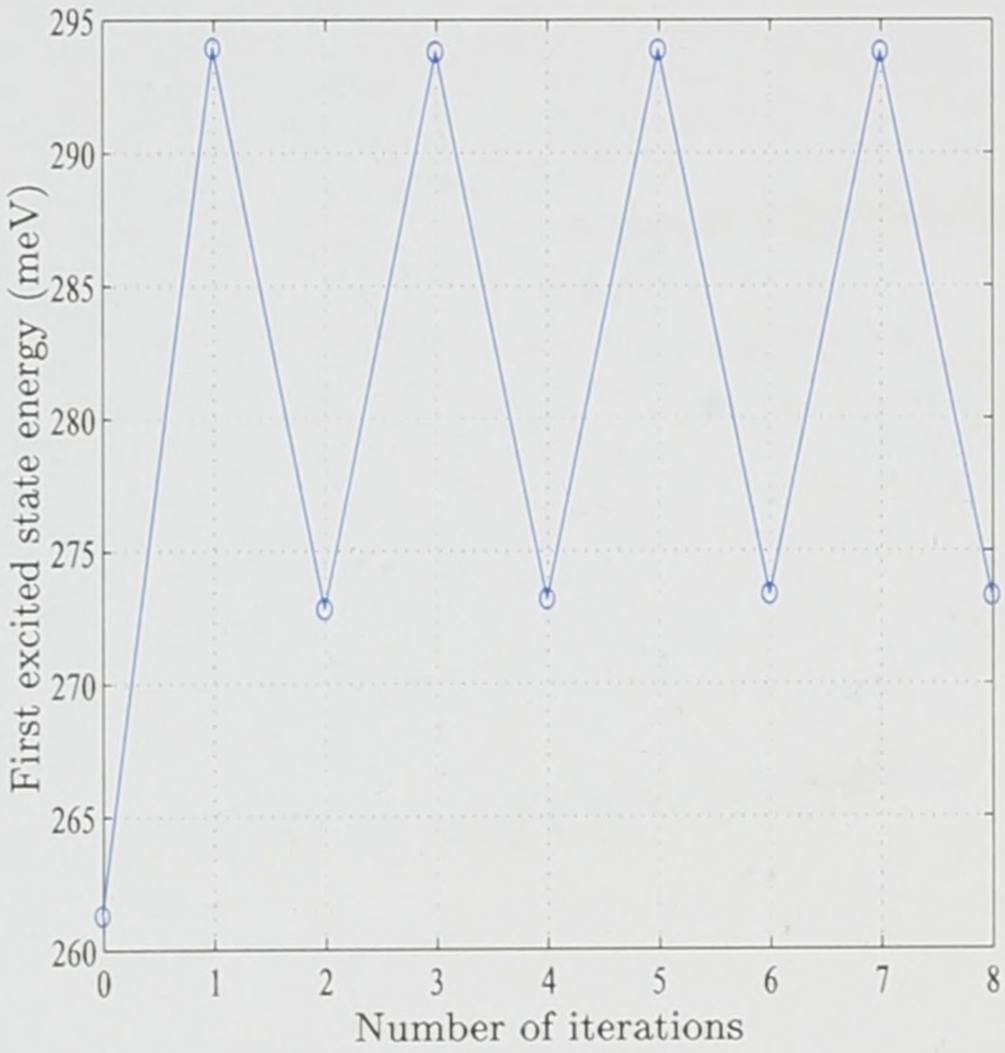

Figure 5.12: First excited state energy versus number of iterations for single quantum dot in the case of 3 electrons.

decided that it was necessary to use a standard relaxation method to achieve a solution. In essence, these methods take an existing solution and "relaxes" them to the correct solution. Taking the view that the simplest solution is usually the best, it was decided to use an averaging approach. In other words, the potential from the first iteration is added to that of the second iteration, averaged and then used to calculate the correct second iteration wave function. This procedure was found to be very effective, and was carried out until a self-consistent solution had been reached.

The same behaviour was observed for the cases of 2 and 4 electrons, and were solved using the same approach. Figure 5.13 show plot of the eigenenergies versus the number of iterations for the case of 2, 3 and 4 electrons respectively.

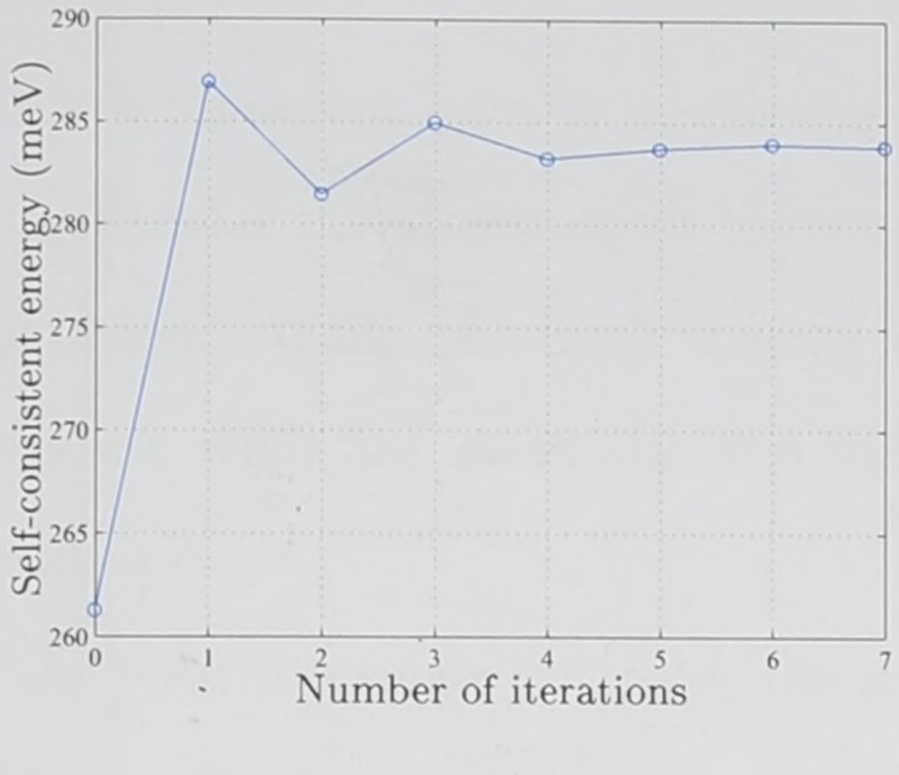

(a) Two electrons

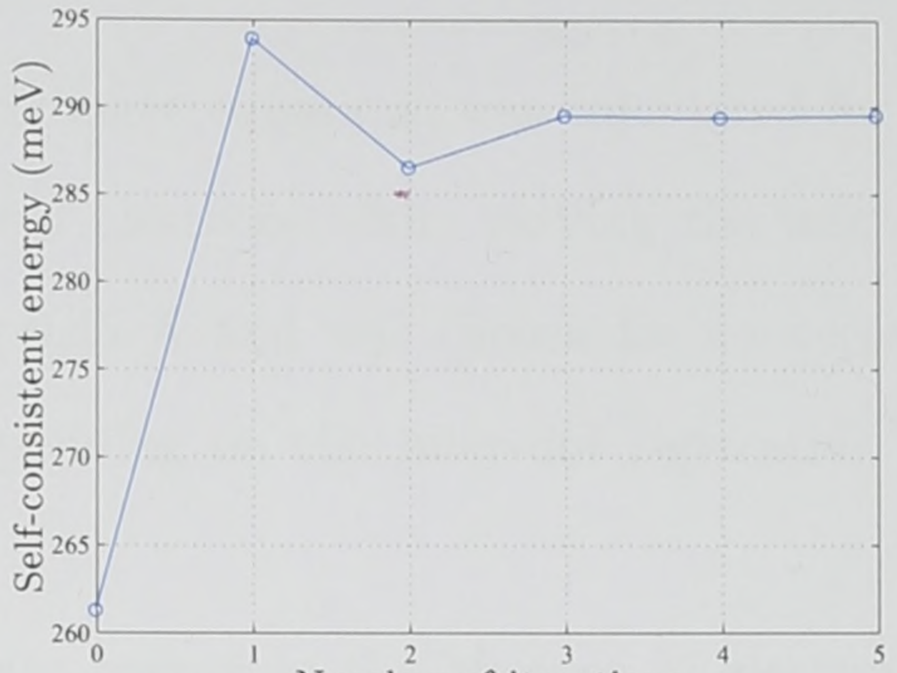

(b) Three electrons

(c) Four electrons

Figure 5.13: Self-consistent energy versus number of iterations for single quantum dot of $h = 60$ Å and $b = 120$ Å in the case of 2, 3 and 4 electrons.

5.4 Coupled quantum dots

Having obtained the self-consistent solution for the case of a single pyramidal quantum dot, the next step was to solve for the case of coupled quantum dots. The system under investigation consisted of a pair of vertically aligned quantum dots and was identical to the system discussed in section 4.4 and displayed in figure 4.14.

5.4.1 Results

The self-consistent solution to the Poisson-Schrödinger equations was calculated for the system under investigation, in the case of $1 \rightarrow 4$ electrons while varying the inter-dot separation. Again, the mesh spacing used was 9.45 Å and was chosen for convergence purposes, while the mesh size was variable depending on the inter-dot separation, see section 4.4.

As with the single dot case, the ground state energy in the absence of electrons is interpreted as energy an electron must possess in order to occupy an empty state in the quantum dot. The eigenenergy calculated in the case of of a single electron is the energy that an electron must possess in order to occupy the other allowed quantum state in the ground state of a system that already contains an electron, and so on. The self-consistent solution for the case of a single electron was calculated while varying the inter-dot separation, by using the ground state wave functions displayed in figure 4.17 to calculate the initial charge distributions. Figure 5.14 shows a plot of the self consistent energy versus dot separation for the case of a single electron.

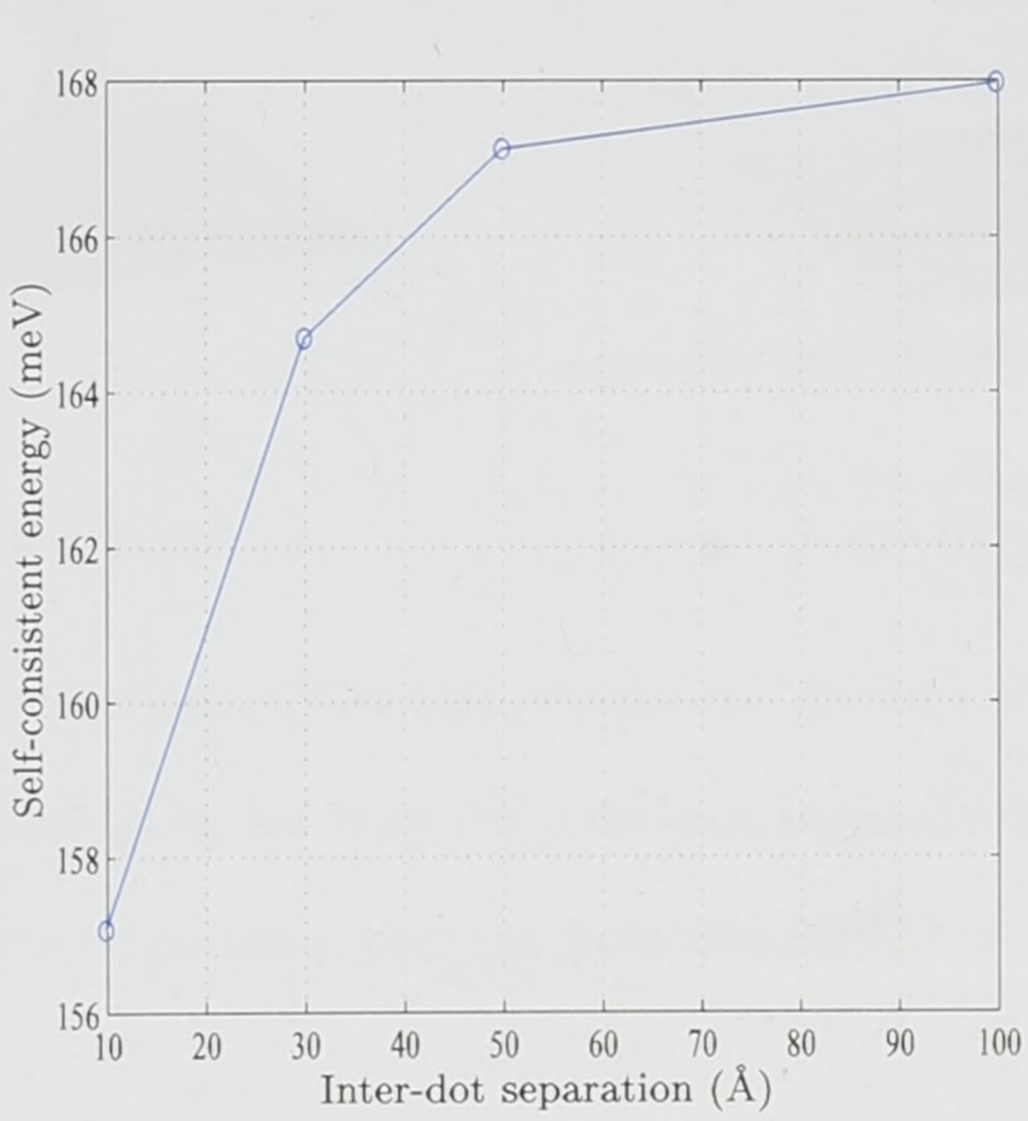

Figure 5.14: Self-consistent energy versus inter-dot separation for a pair of vertically aligned quantum dots for the case of one electron.

Figure 5.14 shows clearly that the self-consistent energy increases as the inter-dot separation is increased. This can be explained by inspecting the wave functions for the different separations. Figure 5.15 shows slices of the wave function for varying inter-dot separations in the case of a single electron.

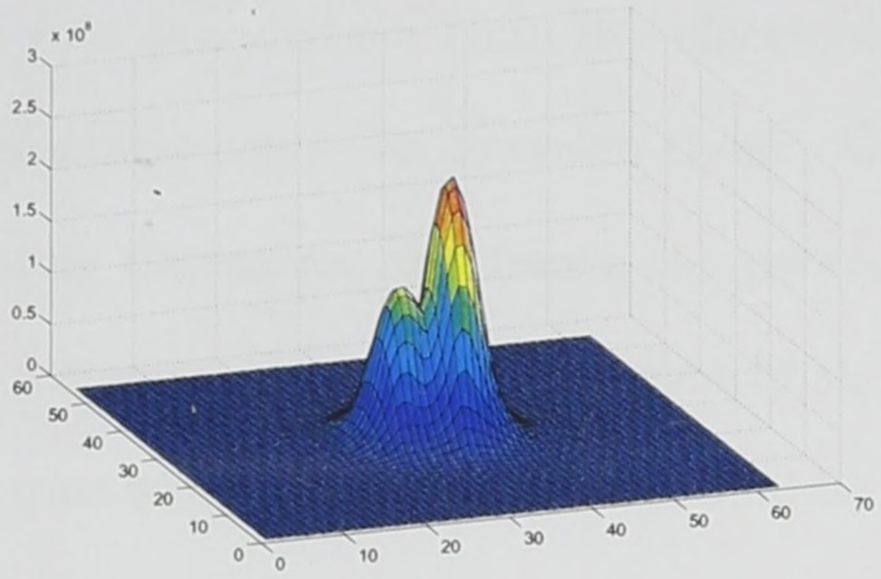

(a) 10 Å separation

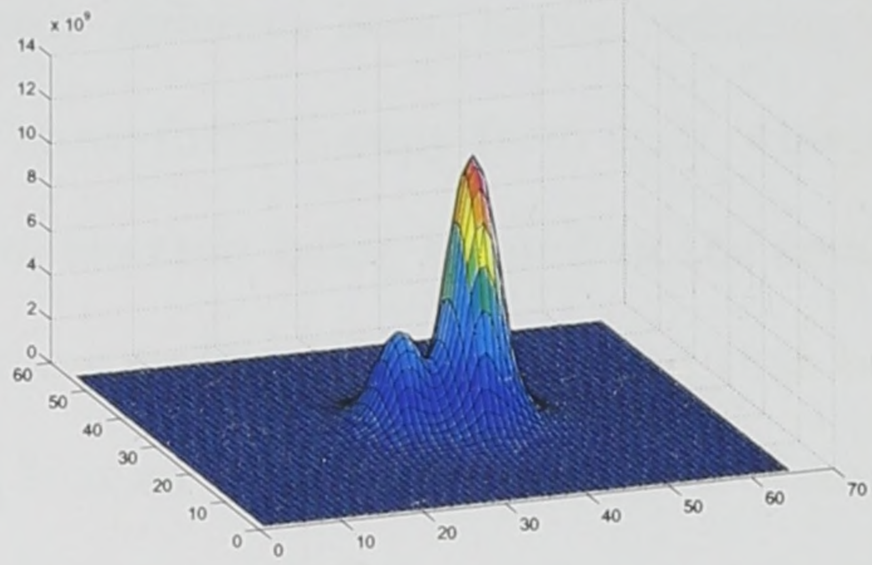

(b) 30 Å separation

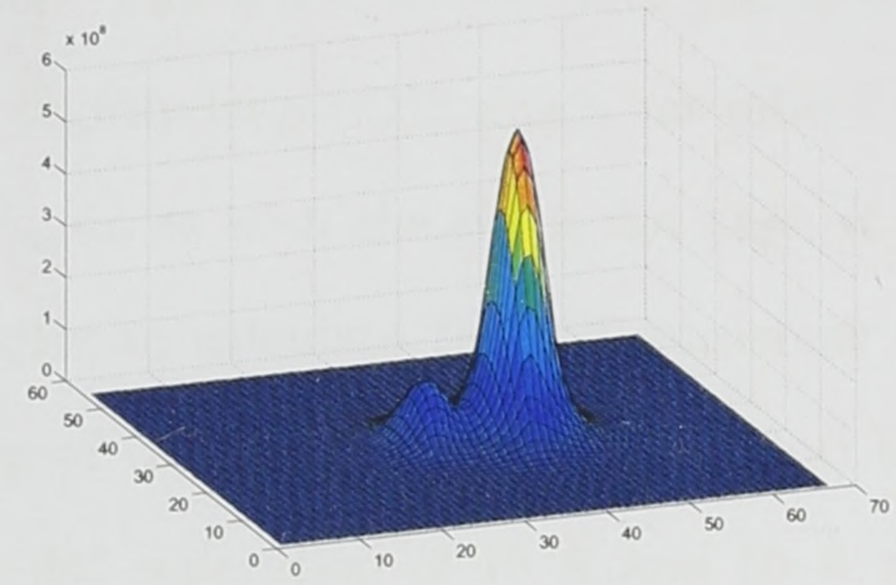

(c) 50 Å separation

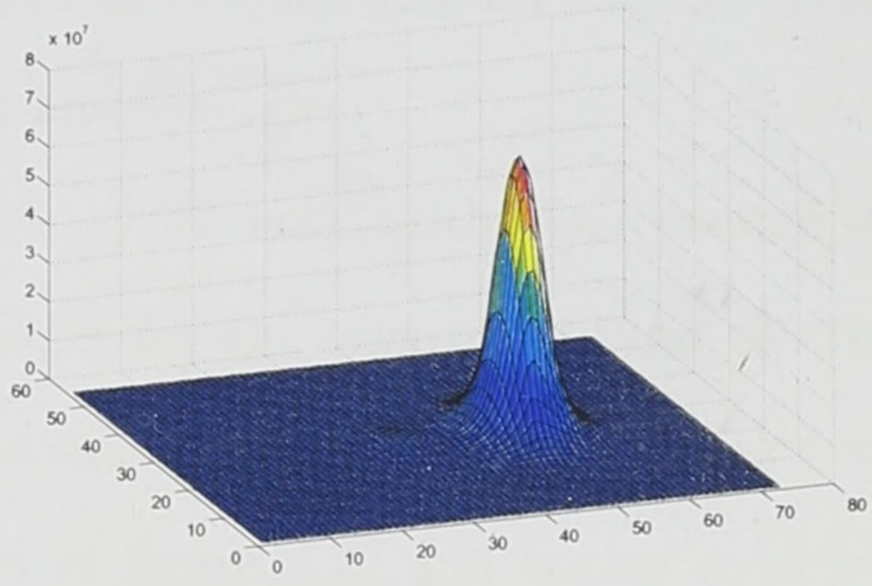

(d) 100 Å separation

Figure 5.15: Normalised slices of the self-consistent ground state wave function for a pair of vertically aligned QDs, for varying inter-dot separations in the case of a single electron. Horizontal coordinates represent position on the $x-z$ plane at $y = 255.15$ Å.

When the dots are in close proximity, as in the case of a separation of 10 Å, there is very strong interaction between the dots. It is worth noting that the interaction between

the dots extends to larger dot separations than that of the empty system, where the upper limit for the coupling was about 40 Å separation, see figure 4.17. The wave function in figure 5.15(a) shows that there is a significant probability that one or both electrons, i.e. the one already in the system and the one being added, may exist in the spatially smaller dot. Since, any system will adjust itself so as to have the lowest possible energy, then one can deduce that the electrons will occupy different dots, hence reducing the electrostatic repulsion between them. As the dots move further away from each other the coupling decreases, and hence the probability of an electron being located in the smaller dot decreases. Figure 5.15(d) clearly shows that the coupling is negligible and that both electrons will have a maximum probability of being located in the larger dot. This of course means that the electrostatic repulsion between the electrons will cause the eigenenergies of the system to increase. It is also worth noting that the eigenenergies of this coupled system are considerably lower than that of the single dot case discussed in the previous section. This is due to the lower overall potential of this coupled system, and the presence of a slightly larger QD which has inherently lower eigenenergies.

Again as with the single dot case, it was necessary to move to the first excited state in order to calculate the self-consistent eigenenergies for the case of multiple electrons. Slices of the first excited state, or anti bonding state, wave function for the cases of an inter-dot separation of 10 Å and 50 Å are shown in figure 4.19 and are an example of the wave functions used to calculate the initial charge distributions. The self-consistent eigenenergies for the cases of 2, 3 and 4 electrons versus the inter-dot separation are shown in figure 5.16.

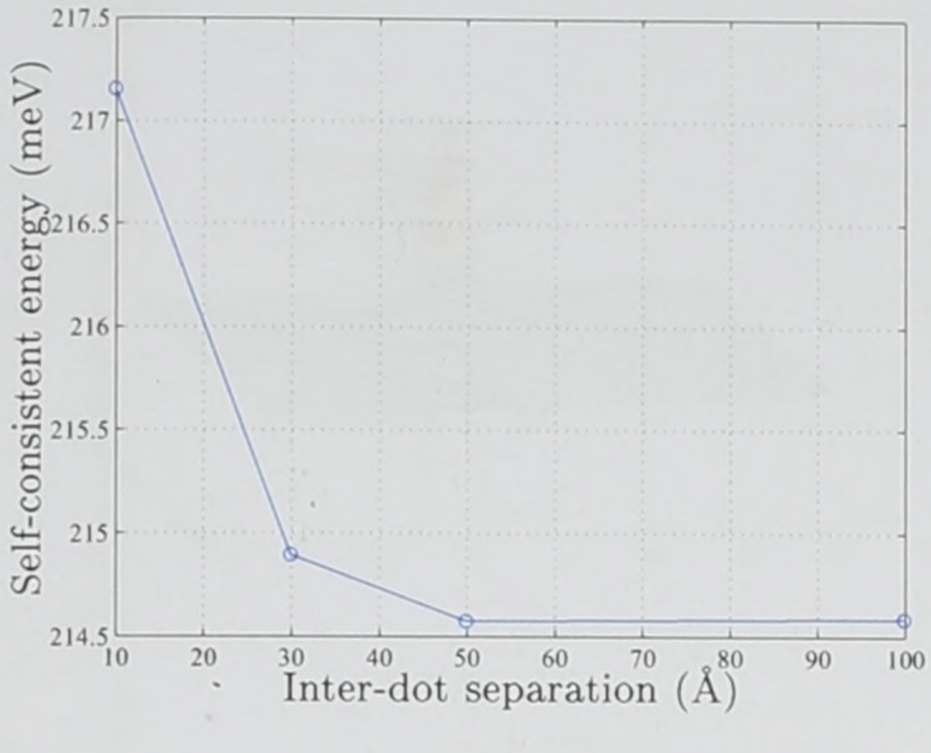

(a) Two electrons

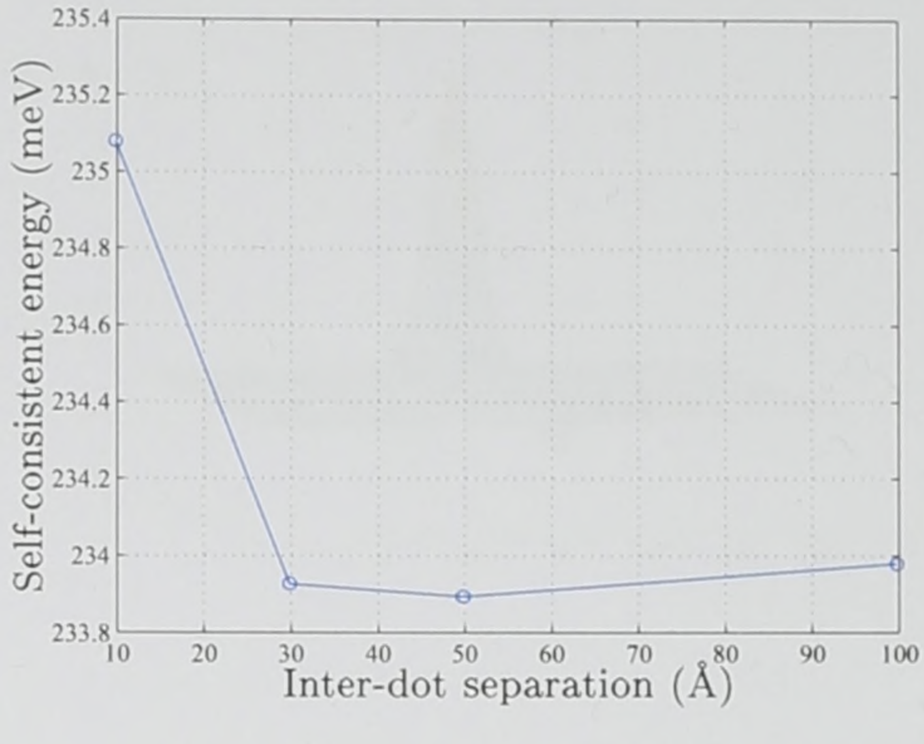

(b) Three electrons

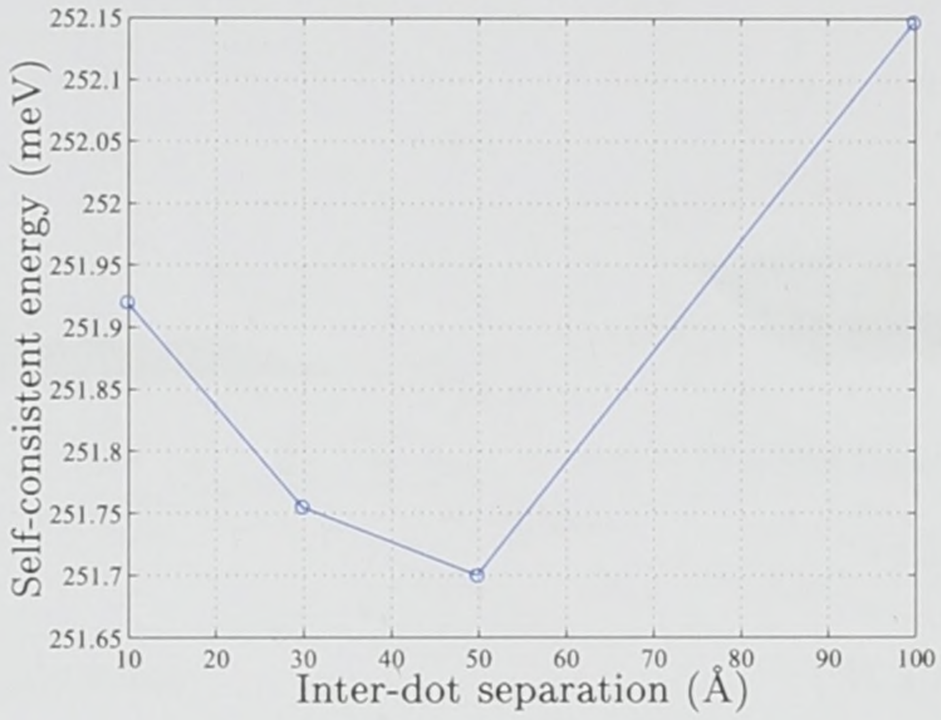

(c) Four electrons

Figure 5.16: Self-consistent energy versus inter-dot separation for a pair of vertically aligned quantum dots for the case of multiple electrons.

In contrast to the single electron case, it was found that for multiple electrons the eigenenergies of the system initially decreased and then increased as the inter-dot separation was increased. This behaviour was most pronounced for the case of 4 electrons, see figure 5.16(c), and as such will be considered as an example case for further discussion.

As before, this behaviour can be explained with the aid of the eigenenergy wave functions. Figure 5.17 shows slices of the wave function, in the case of 4 electrons for a number of inter-dot separations.

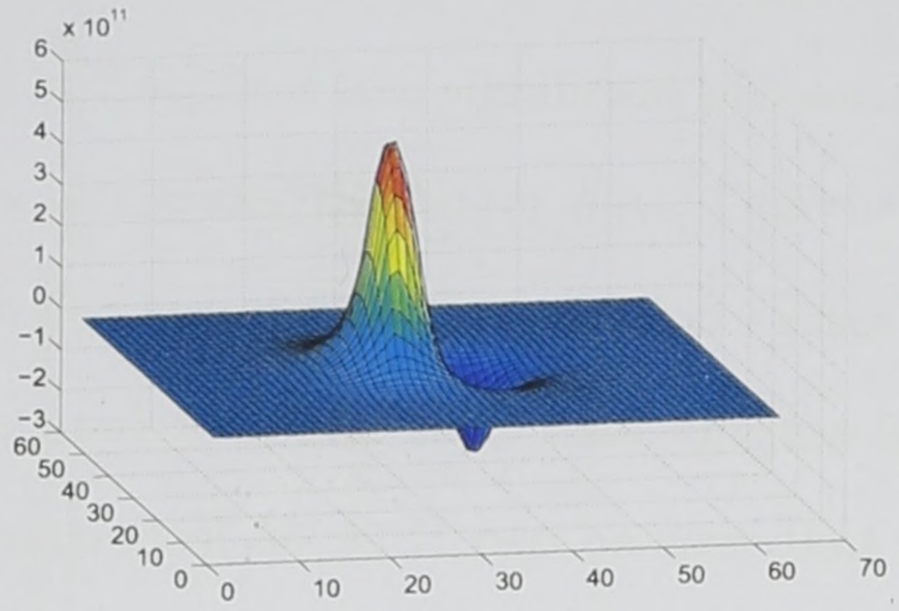

(a) 10 Å separation

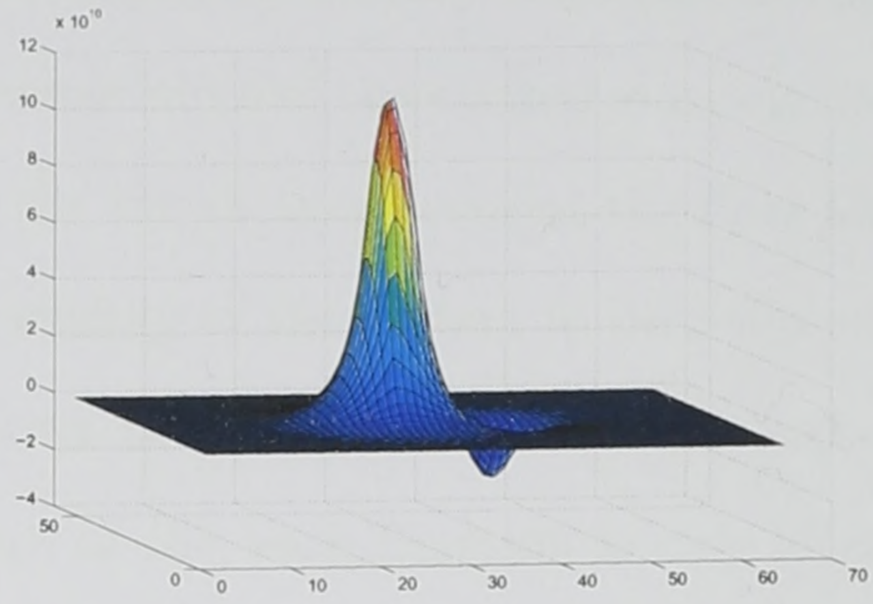

(b) 30 Å separation

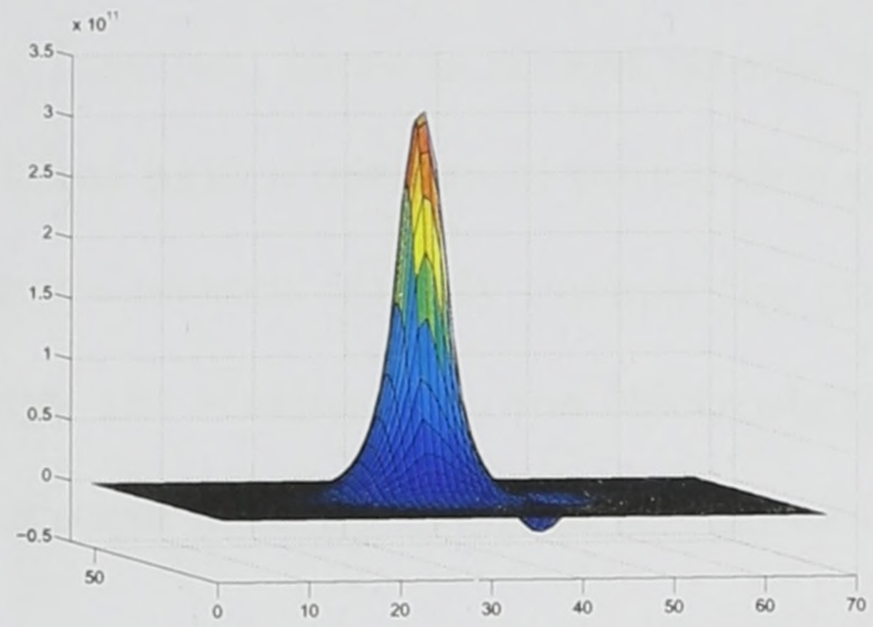

(c) 50 Å separation

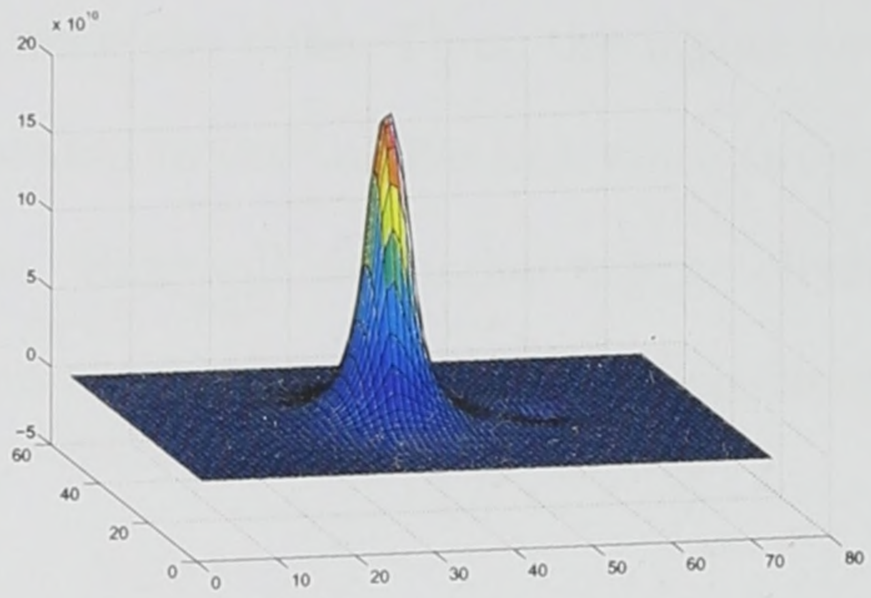

(d) 100 Å separation

Figure 5.17: Normalised slices of the self-consistent ground state wave function for a pair of vertically aligned QDs, for varying inter-dot separations in the case of 4 electrons. Horizontal coordinates represent position on the $x-z$ plane at $y = 255.15$ Å.

In figure 5.17(a) the QDs were 10 Å apart and the wave function shows that there was strong interaction between the dots, which manifests itself as a trough in the wave function that is spatially located over the larger of the two dots while the large positive peak is localised over the smaller dot. This wave function indicates that while the electrons had a maximum probability of being located in the smaller dot, there was still a significant probability that one or more electrons in the first excited state were located in the larger dot. When the electrons were 30 Å apart, the wave function of figure 5.17(b) shows that

while the trough of the wave function is an order of magnitude smaller than that of the 10 Å it still equates to a significant probability that one or more of the excited state electrons were occupying the larger dot. This decrease in the interaction between the dots along with the larger spatial separation causes the eigenenergy of the system to decrease when compared with the 10 Å case. Figure 5.17(c) shows the wave function for an inter-dot separation of 50 Å. It can be seen that the trough of the wave function is only slightly smaller than the case of the 30 Å case, and the dots were further apart thus leading to a further reduction in the eigenenergy of the system. Finally, figure 5.17(d) shows the wave function for an inter-dot separation of 100 Å. As can clearly be seen from the wave function, there is almost no interaction between the dots. Thus, the higher energy electrons have a maximum probability of being located in the smaller dot, since two lower energy electrons already occupy the ground state. Since all the higher energy electrons occupy the smaller dot, the electrostatic repulsion between them causes the eigenenergy to increase in comparison to the previous cases.

5.5 Conclusion

In this chapter the finite difference method developed previously, was extended to incorporate the Poisson equation. The Poisson equation was discretised, formulated into a matrix equation, and solved using the same algorithm as that used for the Schrödinger equation. The procedure for solving the coupled Poisson-Schrödinger equations self-consistently was then outlined.

The method was used to calculate the eigenenergies of a single QD, identical to that discussed in section 4.3, for a varying number of electrons. The convergence to the self-consistent solutions was then discussed, since it was necessary to use a relaxation technique in order to obtain a self-consistent solution for the case of multiple electrons. As would be expected the eigenenergies of the system rise as more electrons are added to the system.

The method was then used to investigate the effect of introducing a varying number of electrons into a system which consisted of a pair of vertically aligned QDs, for a number of different of inter-dot separations. It is worth mentioning that the system investigated was identical to that of section 4.4. It was found that the eigenenergies calculated for a single electron, i.e. the addition energy of a second electron into a system that already contains one, increased as the inter-dot separation was increased. This was due to the fact that as the inter-dot separation was increased, the interaction between the dots decreased. This in turn leads to the electrons being localised in the larger of the two dots, thus increasing the electrostatic repulsion between the electrons.

For the case of multiple electrons it was found that the eigenenergies initially drop and then increase as the inter-dot separation was increased. This behaviour was explained with the aid of the wave functions for the different eigenstates. The wave functions showed that when the dots were in close proximity there was a large interaction between the dots and as a direct result, the probability of one or more electrons occupying the spatially smaller dot was high, while that for the larger dot was smaller but still quite significant. As the dots were moved apart, the interaction between them persisted, but as a result of the larger separation distance the electrostatic repulsion decreased and hence so did the eigenenergy of the system. When the dots got even further apart, the interaction became negligible and as a result the probability of the electrons occupying the larger dot almost vanished. Thus, the electrons occupied the smaller dot and the eigenenergy of the system increased as a consequence of the electrostatic repulsion. Finally it was found that the eigenenergies of the coupled system were considerably lower than their single dot counterparts. This was due to the lower overall potential resulting from the presence of a second dot, which also has inherently lower energies because of its larger size.

Chapter 6

Conclusions

6.1 Concluding remarks

This thesis started out with introducing the need for quantum dots as a viable approach for achieving further miniaturisation when the physical limits of present devices are reached. A number of techniques for the fabrication of QDs were then discussed at length in order to build a picture of their practical realisation. Particular attention was paid to the self-assembly of QDs, since at present this seems to be the most promising route to achieving the fabrication of large, highly dense and uniform arrays of QDs.

The optical properties of QDs were then discussed, with regards to their scattering processes and applications. The literature shows that while the use of QDs has yielded favourable results in a number of fields, most prominently in lasers and laser diodes, they have not always generated results that conform to their predicted dramatic advantages over higher dimensional systems. This emphasises the crucial need to completely understand the physical properties of QDs.

The size and shape of self-assembled quantum dots (SAQD) reported in the literature were then discussed, thus building a picture of the general state of the field and presenting some of the issues that are still open.

Next, a brief introduction to the most successful theoretical approaches in the study of semiconductor systems was presented. These included the $\mathbf{k} \cdot \mathbf{p}$ theory, which was originally a device for exploring the properties of energy bands and wave functions at some important point in $\mathbf{k}$ space [52]. Next was the psuedopotential method, which at heart is a mathematical transformation by which only a few plane waves are required to approximate the psuedowave functions, which is of particular importance in the neighbourhood of the core region. The effective mass approximation (EMA) was then discussed, and is a standard procedure used to approximate the band structure of crystalline semiconductors by only retaining the effective masses and the energy at the extremity of each band. Particular attention was paid to the EMA in heterostructures. A mathematical overview of the two more commonly used numerical methods for the solution of the Schrödinger for QD systems was then presented. Namely, these were the expansion of the wave function in terms of orthogonal period functions [5], and the expansion of the wave function in terms of plane wave Fourier series [65, 66].

Having covered the background material, the contributions of this thesis will now be presented in the remainder of this chapter along with some suggestions for future work.

1. Finite difference method: Quantum wires

A new implementation of the finite difference method was developed, and discussed, for solving the two dimensional time-independent, constant effective mass Schrödinger equation. The motivation behind this approach was to develop a computational technique which is fast to execute and requires a small memory footprint.

To demonstrate its validity, this numerical finite difference method was then utilised to calculate the electronic eigenenergies of an infinitely deep quantum wire, by solving the Schrödinger equation. A new aspect introduced in this work, was basing the identification of the correct physical solutions on the behaviour of the wave functions. It was found that only when a solution was in the near vicinity of the correct physical value did a maximum in the wave function occur away from the corner of the wave function, where an initial

value was defined. In the case of the infinitely deep quantum wire the numerical results calculated agree with the analytical values to within 0.25 meV.

A brief description of how finite confining potentials were included into the method was then given. The method was then used to calculate the electronic eigenenergies of a finitely deep triangular quantum wire that was found in the literature [62]. The calculated energies show very good agreement with that of Gangopahdhyay [62], with the difference in eigenenergies ranging between 2 and 10 meV. This difference is likely to arise from the simplified constant effective mass Hamiltonian. However, even using this simplified Hamiltonian proved to be effective, since the method has the advantages of being relatively fast, where a typical iteration for a 100×100 mesh takes approximately 7 seconds, the main matrix $\mathbf{A}$ required 0.5 Megabyte of storage and the the final wave function was approximately 0.07 Megabyte in size.

A mathematical overview of how the more realistic variable effective mass Hamiltonian can be incorporated into the method was then given. However, a suitable algorithm for solving the system of equations generated was not found. This problem is by no means insurmountable, but it was deemed that the returns from such an increase in complexity would not justify the effort, as present results show that there is good agreement with experimental results.

This technique has the advantages of being easy to implement, scales as N^3 when extended to three dimensions as opposed to N^6 for orthogonal periodic functions (N in the case of this method being the number of mesh points in each direction), all the matrices generated are sparse so the computation time compares favourably with other methods. Also this method is readily expandable to larger spatial areas and completely general three-dimensional potentials.

2. Quantum dots

Having shown that for the two dimensional case, or QWW, that the finite difference method is an efficient and accurate method, the technique was then extended to three

dimensions. The forms of the matrices were deduced and a discussion of how to more efficiently identify the correct physical solutions was presented, along with the justification for using a simple form for the potentials.

The method was employed to calculate the eigenenergies of an infinitely deep quantum box to demonstrate its validity. It was found that the calculated result was within 3 meV of the analytical value [27]. The more complex case of a pyramidal quantum dot was then investigated. It was found that the calculated results were within 2 meV of the values found in the literature [5]. The difference is again attributed to the simple constant effective mass Hamiltonian used. However, the advantages of this method become apparent as it requires a fraction of the memory needed by the eigenvalue method and the computational times also compare favourably with the eigenvalue method. In this case the finite difference requires only 78 Megabyte to store the matrix **A** and 7 Megabyte to store the final wave function. In comparison, the eigenvalue method requires 1 Gigabyte just to store the matrix, and required at best just under 7 hours to obtain a solution [5]. The method presented here required approximately 10 minutes per iteration and a solution can be reached within a few iterations depending on the initial guess.

A numerical investigation of the effect of the inter-dot separation in a system of vertically aligned pyramidal quantum dots was then carried out. It was found that when the separation between the dots was large enough, they behaved as two isolated dots in the sense that the ground state was confined to the slightly larger dot because of its lower energy. As the proximity of the dots increased, so did the interaction between the dots. For the particular system discussed in this thesis the upper limit for the dots to interact with each other was around 40 Å of separation between them, see figure 4.16. The interaction manifests itself as an increase in the peak value of the wave function of the higher energy dot and a reduction in the overall eigenenergies.

2. Self-consistent Poisson-Schrödinger solutions

Recently there has been a growing interest in quantum computation where atomic levels and electron spins play the role of qubits [68]. These qubits usually consist of a pair of coupled quantum dots [13,69]. Thus from a theoretical point of view it is highly desirable to have a method not only for predicting the eigenenergies of the individual QDs, but also the eigenenergy of the system as a whole. It follows that calculating the eigenstates of a QD is not enough, but it is necessary to investigate the behaviour of QDs when a number of electrons are added to the system so as to simulate their behaviour when the eigenstates are occupied by charge carriers.

The Poisson equation, which can be used to relate the potential to the charge distribution, was used to calculate the potential generated by these electrons. This potential was then included into the Schrödinger equation, with the aim of obtaining a self-consistent solution.

The finite difference method developed previously, was extended to incorporate the Poisson equation. The Poisson equation was discretised, formulated into a matrix equation, and solved using the same algorithm as that used for the Schrödinger equation. The Poisson solver was then used to solve for a simple test case of a point charge to demonstrate its validity, where it satisfied the expected behaviour such that $V_\rho \propto r^2$, where V_ρ is the Poisson potential and r is the distance from the point charge. The procedure for solving the coupled Poisson-Schrödinger equations self-consistently was then outlined.

The method was used to calculate the eigenenergies of a single QD, identical to that investigated previously, for a varying number of electrons. The convergence to the self-consistent solutions was then discussed, since it was necessary to use a relaxation technique in order to obtain a self-consistent solution for the case of multiple electrons. As would be expected the eigenenergies of the system rise as more electrons are added to the system.

The method was then used to investigate the effect of introducing a varying number of electrons into a system which consisted of a pair of vertically aligned QDs, for a number of different of inter-dot separations. It was found that the eigenenergies calculated for a

single electron, i.e. the addition energy of a second electron into a system that already contains one, increased as the inter-dot separation was increased. This was due to the fact that as the inter-dot separation was increased, the interaction between the dots decreased. This in turn leads to the electrons being localised in the larger of the two dots, thus increasing the electrostatic repulsion between the electrons.

For the case of multiple electrons it was found that the eigenenergies initially drop and then increase as the inter-dot separation was increased. This behaviour was explained with the aid of the wave functions for the different eigenstates. The wave functions showed that when the dots were in close proximity there was a large interaction between the dots and as a direct result, the probability of one or more electrons occupying the spatially smaller dot was high, while that for the larger dot was smaller but still quite significant. As the dots were moved apart, the interaction between them persisted, but as a result of the larger separation distance the electrostatic repulsion decreased and hence so did the eigenenergy of the system. When the dots got even further apart, the interaction became negligible and as a result the probability of the electrons occupying the larger dot almost vanished. Thus, the electrons occupied the smaller dot and the eigenenergy of the system increased as a consequence of the electrostatic repulsion. Finally it was found that the eigenenergies of the coupled system were considerably lower than their single dot counterparts. This was due to the lower overall potential resulting from the presence of a second dot, which also has inherently lower energies because of its larger size.

In conclusion, this thesis has developed a novel implementation of the finite difference method, which was found to effective, fast and requires little memory overhead when compared to the more commonly used methods. To the best of our knowledge, this is the first implementation of a finite difference method to be utilised in the investigation of pyramidal dots, for both the single dot and coupled dot cases. The inclusion of the Poisson equation into the method and its utilisation in the investigation of single and coupled dots is also a new aspect introduced in this work. Using this finite difference method in the investigation of a number of different systems yielded favourable results.

The next section will present a few suggestions for future work, which can implemented to improve the performance of this method and its application to new systems.

6.2 Future work

The numerical accuracy of the method can be improved by including the effect of variable effective masses and variable permittivities. The efficiency of the routine may also be improved through the use of a nonuniform mesh.

From a physical point of view, it would be of great interest to investigate the effects of magnetic and electric fields on the energy levels of coupled QDs, with the aim of simulating such systems as those developed by Sherwin et al. [13]. It would also be of great benefit to investigate arrays of embedded quantum dots in doped semiconductor wells.

References

[1] M. Ogawa, T. Kunimasa, T. Ito, and T. Miyoshi, "Finite-element analysis of quantum wires with arbitrary cross sections," *Journal of Applied Physics*, vol. 84, no. 6, pp. 3242–3249, 1998.

[2] M. Califano and P. Harrison, "Presentation and experimental validation of a single-band, constant-potential model for self-assembled In/GaAs quantum dots," *Physical Review B*, vol. 61, no. 16, pp. 10959–10965, 2000.

[3] C. Hu *Semicond. Int.*, p. 105, 1994.

[4] F. Lui and M. Lagally, "Self-organised nanoscale structures in Si/Ge films," *Surface Science*, vol. 386, 1997.

[5] M. Califano, *Development of Computational Models For the Electronic Structure of Self-Assembled Qunatum Dots.* PhD thesis, Institute of Microwaves and Photonics, School of Electronic and Electrical Engineering, University Of Leeds, 2001.

[6] S. M. Reimann and M. Manninen, "Electronic structure of quantum dots," *Reviews of Modern Physics*, vol. 74, no. 4, pp. 1283–1342, 2002.

[7] A. Wensauer, O. Steffens, M. Suhrke, and U. Rössler, "Laterally coupled few-electron quantum dots," *Physical Review B*, vol. 62, no. 4, 2000.

[8] F. Troiani, U. Hohenester, and E. Molinari, "Electron-hole localization in coupled quantum dots," *Physical Review B*, vol. 65, 2002.

[9] S. Fafard, M. Spanner, J. P. McCaffrey, and Z. Wasilewski, "Coupled InAs/GaAs quantum dots with well-defined electronic shells," *Applied Physics Letters*, vol. 76, no. 16, pp. 2268–2270, 2000.

[10] C. Kadow, A. Jackson, A. Gossard, S. Matsuura, and G. Blake, "Self-assembled ErAs islands in GaAs for optical-heterodyne THz generation," *Applied Physics Letters*, vol. 76, no. 24, 2000.

[11] J. Phillips, P. Bhattacharya, S. Kennerly, D. Beekman, and M. Dutta, "Self-assembled InAs-GaAs quantum-dot intersubband detectors," *IEEE Journal of Quantum Electronics*, vol. 35, no. 6, 1999.

[12] H. Cao, J. Xu, W. Xiang, Y. Ma, S.-H. Chang, S. Ho, and G. Solomon, "Optically pumped InAs quantum dot microdisk lasers," *Applied Physics Letters*, vol. 76, no. 24, 2000.

[13] M. S. Sherwin, A. Imamoglu, and T. Montroy, "Quantum computation with quantum dots and terahertz cavity quantum electrodynamics," *Physical Review A*, vol. 60, no. 5, 1999.

[14] S.-S. Li, J.-B. Xia, J.-L. Liu, F.-H. Yang, Z.-C. Niu, S.-L. Feng, , and H.-Z. Zheng, "InAs/GaAs single-electron quantum dot qubit," *Journal of Applied Physics*, vol. 90, no. 12, 2001.

[15] D. Bimberg, M. Grundmann, and N. N. Ledentsov, *Quantum Dot Heterostructures.* John Wiley and Sons, Ltd, 1999.

[16] M. Jaros, *Physics and Applications of Semiconductor Microstructures.* Oxford : Clarendon Press, 1989.

[17] K. Barnham and D. Vvedensky, eds., *Low-dimensional semiconductor structures.* Cambridge Univerity Press, 2001.

[18] I. N. Stranski and L. von Krastanow *Wiss. Lit. Mainz Abh. Math. Naturwiss. K1. IIb*, vol. 146, p. 797, 1939.

[19] H. Sunamura, N. Usami, and Y. Shiraki, "Island formation during growth of Ge on Si(100): A study using photoluminescence spectroscopy," *Applied Physics Letters*, vol. 66, no. 22, p. 3024, 1995.

[20] D. Eaglesham and M. Cerullo, "Dislocation-free Stranski-Karastanow Growth of Ge on Si(100)," *Physical Review Letters*, vol. 64, no. 16, 1990.

[21] A. Sasaki, "Initial growth layers and critical thickness of InAs heteroepitaxy on GaAs substrates," *Journal of Crystal Growth*, vol. 160, pp. 27–35, 1996.

[22] J. Tersoff and F. LeGoues, "Competeing relaxation mechanisims in strained layers," *Physical Review Letters*, vol. 72, no. 22, 1994.

[23] J. Tersoff and R. Tromp, "Shape transition in growth of strained islands: spontaneous formation of quantum wires," *Physical Review Letters*, vol. 70, no. 18, 1993.

[24] P. Harrison, R. W. Kelsall, P. Kinsler, and K. Donovan, "Quantum well intersubband transitions as a source of terahertz radiations," in *1998 IEEE sixth international conference on THz Electronics Proceedings*, pp. 74–78, 1998.

[25] B. Xu, Q. Hu, and M. R. Melloch, "Electrically pumped tunable terahertz emitter based on intersubband transition," *Applied Physics Letters*, vol. 71, p. 440, 1997.

[26] H. Benisty, C. Sotomayor-Torrés, and C. Weisbuch, "Intrinsic mechanism for the poor luminescence properties of quantum-box systems," *Physical Review B*, vol. 44, no. 19, p. 10945, 1991.

[27] P. Harrison, *Quantum Wells, wires and dots: theoretical and computational physics.* John Wiley & Sons, LTD., 2000.

[28] R. J. Warburton, "Self-assembled semiconductor quantum dots," *Contemporary Physics*, vol. 43, no. 5, pp. 351–364, 2002.

[29] D. Gammon, E. Snow, B. Shanabrook, D. Katzer, and D. Park, "Homogenous linewidths in the optical spectrum of a single Gallium Arsenide quantum dot," *Science*, vol. 273, p. 87, 1996.

[30] T. Sosnowski, T. Norris, H. Jiang, J. Singh, K. Kamath, and P. Bhattacharya, "Rapid carrier relaxation in $In_{0.4}Ga_{0.6}As/GaAs$ quantum dots characterized by differential transmission spectroscopy," *Physical Review B*, vol. 57, p. 9423, 1998.

[31] Y. Arakawa and H. Sakaki, "Multidimensional quantum well laser and temperature dependence of its threshold current," *Applied Physics Letters*, vol. 40, p. 939, 1982.

[32] M. V. Maximov, I. V. Kochnev, Y. M. Shernyakov, S. V. Zaitsev, N. Y. Gordeev, A. F. Tsatsul'nikov, A. V. Sakharov, I. L. Krestnikov, P. S. Kop'ev, Z. I. Alferov, N. N. Ledentsov, D. Bimberg, A. O. Kosogov, P. Werner, and U. Gösele, "InGaAs/GaAs quantum dot lasers with ultrahigh characteristic temperature $t_0 = 385$K grown by organic chemical vapour deposition," *Japanese Journal of Applied Physics*, vol. 36, p. 4221, 1997.

[33] D. Bouwmeester, A. Ekert, and A. Zeilinger, *The physics of quantum information.* Springer:Berlin, 2000.

[34] J.-M. Gèrard and B. Gayral, "Strong purcell effect for InAs quantum boxes in three-dimensional solid-state microcavities," *Journal of Lightwave Technology*, vol. 17, no. 11, p. 2089, 1999.

[35] C. Santori, M. Pelton, G. Solomon, Y. Dale, and Y. Yamamoto, "Triggered single photons from a quantum dot," *Physical Review Letters*, vol. 86, no. 8, 2001.

[36] P. Michler, A. Kiraz, C. Becher, W. Schoenfeld, P. Petroff, L. Zhang, E. Hu, and A. Imamoglu, "A quantum dot single-photon turnstile device," *Science*, vol. 290, p. 2282, 2000.

[37] C. Santori, D. Fattal, J. Vucković, G. S. Solomon, and Y. Yamamoto, "Indistinguishable photons from a single-photon device," *Nature*, vol. 419, p. 594, 2002.

[38] T. Lundstrom, W. Schoenfeld, and P. Petroff, "Exciton storage in semiconductor self-assembled quantum dots," *Science*, vol. 286, p. 2312, 1999.

[39] D. Haft, R. J. Warburton, K. Karrai, S. Huant, G. Medeiros-Ribeiro, J. M. Garcia, W. Schoenfeld, and P. M. Petroff, "Luminescence quenching in InAs quantum dots," *Applied Physics Letters*, vol. 78, no. 19, p. 2946, 2001.

[40] M. Grundmann, J. Christen, N. N. Ledentsov, J. Böhrer, D. Bimberg, S. S. Ruvimov, P. Werner, U. Gösele, J. Heydenreich, V. M. Ustinov, A. Y. Egorov, A. E. Zhukov, P. S. Kop'ev, and Z. I. Alferov, "Ultranarrow luminescence lines from single quantum dots," *Physical Review Letters*, vol. 74, no. 20, p. 4043, 1995.

[41] J. M. Moison, F. Houzay, F. Barthe, L. Leprince, E. André, and O. Vatel, "Self-organized growth of regular nanometer-scale InAs dots on GaAs," *Applied Physics Letters*, vol. 64, no. 2, 1994.

[42] D. Leonard, K. Pond, and P. M. Petroff, "Critical layer thickness for self-assembled InAs islands on GaAs," *Physical Review B*, vol. 50, no. 16, 1994.

[43] M. Fricke, A. Lorke, J. P. Kotthaus, G. Medeiros-Ribeiro, and P. M. Petroff, "Shell structure and electron-electron interaction in self-assembled InAs quanum dots," *Europhysics Letters*, vol. 36, no. 3, pp. 197–202, 1996.

[44] S. Sauvage, P. Boucaud, F. H. Julien, J. M. Gèrard, and J. Y. Marzin, "Infrared spectroscopy of intraband transitions in self-organized InAs/GaAs quantum dots," *Journal of Applied Physics*, vol. 82, no. 7, 1997.

[45] N. Liu, J. Tershoff, O. Baklenov, J. A. L. Holmes, and C. K. Shih, "Nonuniform composition profile of $In_{0.5}Ga_{0.5}As$ alloy quantum dots," *Physical Review Letters*, vol. 84, no. 2, p. 334, 2000.

[46] I. Kegel, T. H. Metzger, A. Lorke, J. Peisl, J. Stangl, G. Bauer, J. M. Garcìa, and P. M. Petroff, "Nanometer-scale resolution of strain and interdiffusion in self-assembled InAs/GaAs quantum dots," *Physical Review Letters*, vol. 85, no. 8, p. 1694, 2000.

[47] Z. M. Wang, K. Holmes, Y. I. Mazur, and G. J. Salamo, "Fabrication of (In, Ga)As quantum-dot chains on GaAs(100)," *Applied Physics Letters*, vol. 84, no. 11, p. 1931, 2004.

[48] J. Y. Marzin, J. M. Gèrard, A. Izraël, D. Barrier, and G. Bastard, "Photoluminescence of single quantum dots obtained by self-organized growth on GaAs," *Physical Review Letters*, vol. 73, no. 5, p. 716, 1994.

[49] M. Grundmann, O. Stier, and D. Bimberg, "InAs/GaAs pyramidal quantum dots: Strain distribution, optical phonons, and electronic structure.," *Physical Review B*, vol. 52, no. 16, p. 11969, 1995.

[50] K. H. Schmidt, G. Medeiros-Ribeiro, M. Oestreich, P. M. Petroff, and G. H. Döhler, "Carrier relaxation and the electronic structure of InAs self-assembled quantum dots," *Physical Review B*, vol. 54, no. 16, p. 11346, 1996.

[51] F. Bloch *Z. Phys.*, vol. 52, p. 555, 1928.

[52] R. Willardson and A. C. Beer, eds., *Semiconductors and semimetals*, vol. 1. Boston London : Academic, 1966.

[53] S. L. Chuang, *Physics of Optoelectronic Devices.* New York Chichester : Wiley, 1995.

[54] T. Wenckebach, *Essentials of semiconductor physics.* Chichester, West Sussex: John Wiley and Sons, Ltd, 1999.

[55] G. Baraff and D. Gershoni, "Eigenfunction-expansion method for solving the quantum-wire problem: Formulation," *Physical Review B*, vol. 43, p. 4011, 1991.

[56] O. Stier and D. Bimberg, "Modeling of strained quantum wires using eight-band k.p theory," *Physical Review B*, vol. 55, no. 12, pp. 7726–7732, 1997.

[57] E. O. Kane, *Handbook on Semiconductors.* T.S. Moss, North Holland, Amsterdam, 1982.

[58] J. M. Luttinger and W. Kohn, "Motion of electrons and holes in perturbed periodic fields," *Physical Review*, vol. 97, p. 869, 1955.

[59] M.-F. Li, *Modern semiconductor quantum physics.* World Scientific Publishing Co. Pte. Ltd., 1994.

[60] J. H. Davies, *The Physics of low-dimensional semiconductors - An Introduction.* Cambridge Univerity Press, 1998.

[61] D. Gershoni, H. Temkin, G. Dolan, J. Dunsmuir, S. Chu, and M. Panish, "Effects of two-dimensional confinementon the optical properties of InGaAs/InP quantum wire structures," *Appl. Phys. Lett.*, vol. 53, no. 11, 1988.

[62] S. Gangopahdhyay and B. Nag, "Energy levels in finite barrier triangular and arrowhead-shaped quantum wires," *Journal of Applied Physics*, vol. 81, no. 12, pp. 7885–7889, 1997.

[63] S. Gangopahdhyay and B. Nag, "Energy levels in three-dimensional quantum-confinement structures," *Nanotechnology*, vol. 8, pp. 14–17, 1997.

[64] P. Harrison, "Matrix methods." Unpublished, 2001.

[65] M. Tadiċ and Z. Ikonič, "Self-consistent electronic-structure calculation of rectangular modulation-doped GaAs/$Ga_{1-x}Al_xAs$ quantum wires," *Physical Review B*, vol. 50, no. 11, 1994.

[66] M. Tadić, Z. Ikonič, and V. Milanović, "The self-consistent electronic structure of rectangular free-standing quantum wires:Fourier expansion approach," *Superlattices and Microstructures*, vol. 23, pp. 369–379, 1998.

[67] R. Johnson and R. Pollard, *Development of the Leeds Physical model, End of year report.* University of Leeds, 1999.

[68] X. Hu and S. D. Sarma, "Hilbert-space structure of a solid-state quantum computer:two-electron states of a double–quantum-dot molecule," *Physical Review A*, vol. 61, 2000.

[69] X.-Q. Li and Y. Yan, "Highly coherent solid-state quantum bit from a pair of quantum dots," *Applied Physics Letters*, vol. 81, no. 1, 2002.

[70] J. Kyriakidis, M. Pioro-Ladriere, M. Ciorga, A. Sachrajda, and P. Hawrylak, "Voltage-tunable singlet-triplet transition in lateral quantum dots," *Physical Review B*, vol. 66, 2002.

[71] D. Austing, S. Sasaki, K. Muraki, K. Ono, S. Tarucha, M. Barranco, A. Emperador, M. Pi, and F. Garcias, "Influence of mismatch on the addition energy spectra of vertical diatomic artificial molecules," *Physica E*, vol. 12, pp. 896–899, 2002.

[72] B. Szafran, S. Bednarek, and J. Adamowski, "Parity symmetry and energy spectrum of excitons in coupled self-assembled quantum dots," *Physical Review B*, vol. 64, 2001.

[73] B. Partoens and F. Peeters, "Two vertically coupled quantum dots in a magnetic field," *Physica B*, vol. 298, 2001.

[74] D. El-Moghraby, R. Johnson, and P. Harrison, "Calculating the modes of quantum wire and dot systems using a finite differencing technique," *Computer Physics Communications*, vol. 150, no. 3, pp. 235–246, 2003.

[75] C. Snowden, *Semiconductor Device Modelling.* London: Peregrinus, 1988.

[76] P. Machado, *Modelling of ultra-small scale microwave transistor structures.* PhD thesis, Dept. of Electronic and Electrical Engineering, University of Leeds, 2001.